Universitat de Barcelona

Mechano-chemical study of rotatory molecular Motors

Rubén Pérez Carrasco

Mechano–chemical study of rotatory molecular motors

Ph.D. thesis

Rubén Pérez Carrasco

Ph.D. advisor:
José María Sancho Herrero

Departament d'Estructura i Constituents de la Matèria
Facultat de Física. Universitat de Barcelona

A mis padres.

A Jose.

Agradecimientos

A pesar de que la autoría de esta tesis lleve mi nombre, todo lo escrito lo debo en gran parte a lo que he aprendido de muchas otras personas. Por eso quiero agradecerle mi formación a todos mis maestros. No sólo a aquellos que son profesores como oficio si no a aquellos que han moldeado una parte de mí,

A mi padre, si ha habido realmente un maestro en mi vida, es él.

A mi madre, por confiar en mí y dejarme siempre elegir.

A Pili, por cuidar siempre de mí, aunque sea con zumos de zanahoria.

A Vanessa, la persona junto a quien empecé a aprender, y sigo haciéndolo.

A Dámaris, ojalá todo el mundo escuchara y reflexionara como ella.

A Carlos, él entiende que nada es cierto ni falso y que nadie puede tener razón.

A Jose B., por mostrarme que de todo se puede aprender algo.

A Paz, por regalarme un cartabón cuando más lo necesitaba.

A David, no se puede aprender nada sin el abogado del diablo cerca.

A Noemí, por no rendirse nunca, por no faltar nunca, porque me inspiras.

A Ana, por enseñarme que no existen las fronteras.

A Agnés, per tots aquells pastissos de xocolata que ens feien passar el fred.

A Jose María, mi director, por enseñarme a hacer ciencia más allá de los libros.

A Marta, mi confesora científica y ejemplo a seguir.

A Jose, por acompañarme en esta aventura y enseñarme a querer cada día mejor.

A María K., porque no le hacen falta sardinas pa beber agua.

A Pau, demostrant cada dia que la raó i el cor no són incompatibles.

A Javi, por su ayuda constante en todos los ámbitos.

A María Q., gracias a ella no soy la persona más despistada del mundo.

A Katja, por invitarme a hacer ciencia en San Diego.

A Eze, Nekane, Silvia y Paco por conquistar Chichibabin cuando Kara Thrace duerme.

To Richard, for letting me play with real molecular motors.

To Ananthi, Sumi and Dharma, who took me in making me feel a part of their family.

A los compañeros de la facultad que hacen ciencia de calidad en tiempos precarios.

A Benasquepipol y a GEFENOL por juntar física, futuro y chuletón.

A Laura R., Lilly A., Donna N,... por hacerme olvidar la física si lo necesitaba.

A Ender, Hercules, Corso,... acompañándome en cada viaje.

The wonderful noonday silence of a tropical forest is, after all, due only to the dulness of our hearing; and could our ears catch the murmur of these tiny maelstroms, as they whirl in the innumerable myriads of living cells which constitute each tree, we should be stunned, as with the roar of a great city.

Thomas Huxley (1868)

Contents

1 Introduction

1.1. The physical cell

The definition of *Physics* given by the Oxford English Dictionary is *the branch of science concerned with the nature and properties of matter and energy.* Such a definition is quite extensive, everything is made of matter. Therefore, how is Physics distinguished from other branches of science? Similar questions arise when looking for the definition of other areas of scientific knowledge, being impossible to isolate them from the rest of branches of knowledge. Despite this evident connection between scientific branches, each one has taken a different path along history studying different problems, developing its own jargon and its own set of techniques that usually hide its connection with the rest.

For instance, a biologist would define the cell as the minimal unit of life that holds some characteristic functions, such as feeding itself, moving or reproducing. Whenever a deeper description is requested, a traditional biologist will recall the constituents of the cell describing its organelles and how they are related to the different functions of the cell. An even more detailed portrait will lead to descrip-

tions of the biochemical structures of the organelles or the biochemical reaction networks that drive all the chemical processes regulating the cell inner working. On the other hand, a classical physicist observing a cell will describe it as a complex system out of equilibrium where matter aggregated at different scales is continuously transducing between energy, matter and information. These two parallel descriptions, the one from the biologist and the one from the physicist, are in fact the same. A cell feeding itself is nothing else than the cell getting matter from the exterior and processing it to get useful energy.

As a matter of fact, biology and engineering are two sides of the same coin. Engineering is regarded as the human skill to build structures and machines able to have a certain function, whereas, biology studies the structures that nature, through natural selection, has developed. Those natural structures become the tools that allow living systems to perform their different functions. It is, thus, not casual that nature and engineering have converged many times to similar solutions to akin problems. Sometimes, the convergence has occurred independently. This situation, regarded in evolutionary biology as convergent evolution, is the case, for instance, of the use of Earth's magnetic field as an orientation mechanism. Even though human being uses compasses since Ancient China, many biological systems had already expertised the orientation through Earth's magnetic field. This is the case of *Magnetospirillum gryphiswaldense*, a bacterium that can contain magnetite (Fe_3O_4) crystals that orientate the bacterium with Earth's magnetic field [73] (Fig. 1.1). Other times, the convergence between engineering and nature results from the human observation of nature as it happens with the human devising of planes, inspired by birds.

Accordingly, the benefits of this coupling between engineering and life sciences is mutual. Not only the insight into biological systems requires the phys-

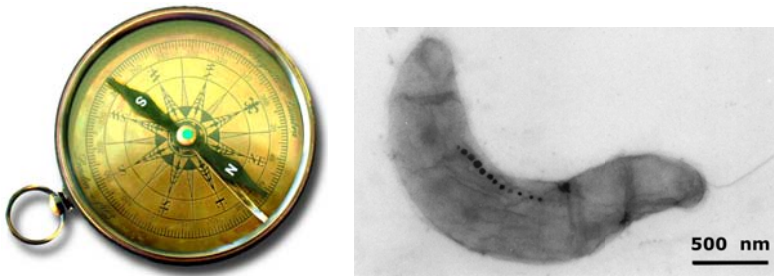

Figure 1.1: Example of convergent evolution in design between mankind and nature. Left: The compass' magnetic pointer orientates with Earth's magnetic field. Right: A *Magnetospirillum gryphiswaldense* containing a chain of magnetosomes enclosing magnetite particles. The magnetic chain helps the bacterium to get oriented. Image extracted from [73].

ical knowledge to understand the mechanisms by which living systems manage energy and matter, but also the study of biological systems reveals new optimisation ideas [18].

This discussion on the intersection between biological and physical sciences can also be applied to nanometric scales, describing the working of a cell as a set of enclosed natural machines and structures that constitute the minimal unit of life. This alternate definition of a cell is again compatible with the one given by biologists and physicists and reveals again how diffuse are the limits between different scientific areas and how gathering the available scientific knowledge is mandatory to get a full insight of nature.

The picture of a cell composed by machines has had a long trail along history [11, 17], little by little converging to the actual concept of molecular machines that began in the XXth century with their first experimental observations. Actually, the current picture of molecular machines was finally drawn with Alberts famous

paper [3] pointing out the physical relevance on the study of subcellular processes and the importance of interdisciplinarity in this quest.

1.2. Molecular Machines

The molecular machines referred in the previous section are not any abstract construction. Molecular machines are real macromolecules, mainly proteins, that continuously transduce between different kinds of energy. The output of the energetic transduction can be a mechanical work *i.e.* to attain a net displacement against a hindering force. In this case, molecular machines are also referred as molecular motors or motor proteins. However, both terms, machine and motor, are usually regarded as synonyms in the literature.

For molecular motors, the interrelation between structure and function is even closer than in other machines. Molecular proteins are nothing else than a polymeric chain built out of hundreds or even thousands of amino acids. Nonetheless, only 20 different natural amino acids are necessary for the construction of the machinery of life. The difference between amino acids in size, polarity, charge or hydrophobicity gives place to different interactions of the proteinic chain with itself and with the surrounding molecules of the environment, folding the protein (Fig. 1.2) [83]. Thus, the specific composition of the protein gives place to its actual biochemical tridimensional structure and, more than that, to its function. Furthermore, the structure of an individual molecular machine is not unique, but several marginally stable configurations are compatible with the primary structure of the protein. This pliancy gives the motor its mechanical abilities. It is the product of this complex coupling between chemical and spatial properties what gives molecular machines their ability to transduce between different kinds of energy [4, 83].

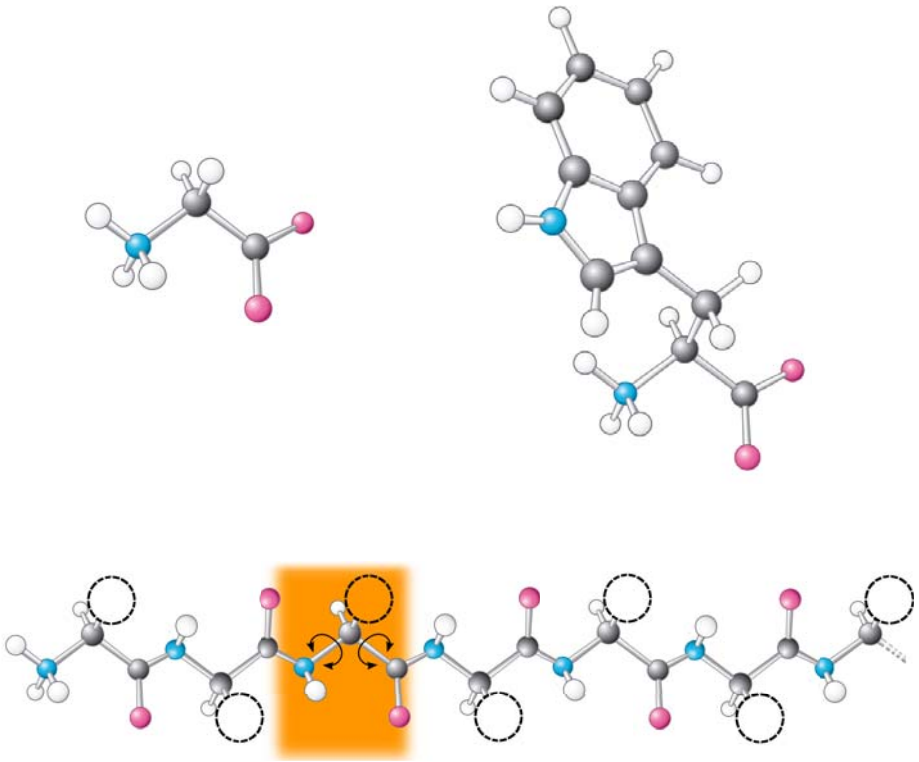

Figure 1.2: . Proteins are chains of amino acids. Top left: Glicine, The smallest amino acid. Top right: Triptophan, the largest amino acid. Bottom: Scheme of a protein backbone formed by only 7 amino acids. Only the functional groups amine ($-NH_2$) and carboxyl ($-COOH$) are shown. The position of the lateral chain that will identify each amino acid is marked with a black circle. Additionally, one amino acid is highlighted (*orange box*) where the rotational angles of the chain are specified. The rotation of the protein backbone allows its folding that will be set by the actual amino acids conforming the chain. Colour code: Hydrogen (*white*), Carbon (*grey*), Oxygen (*magenta*) and Nitrogen (*blue*). The schemes are based on those of [83].

The functions that molecular machines can accomplish are multiple. Here a brief tour among different motors and their function is provided. In this tour, molecular motors are separated in three groups regarding their function, namely, cytoskeletal machines, machines manipulating the structure of other molecules and transmembranal translocators. Such classification should only serve as a guide to review the high diversity of molecular motors in a more ordered way. However, some motors could lay in different of the categories introduced. Furthermore, only some of the existing motors and their function are presented in order to show the high variety of subcellular processes driven by molecular motors. A more thorough review on the topic can be found in [11, 72].

Probably the most famous molecular motors are those interacting with cell cytoskeleton. Such motors comprise kinesins, myosins and dyneins, and are able to attach and detach actively to actin and microtubule filaments. Those polymeric filaments act as tracks for the cytoskeletal molecular motors. The operation of cytoskeletal motors is devised to generate a force on the track that can attain many different purposes. Usually, the force entails an active transport. This directional transport along the cytoskeleton is useful to transport big cargoes such as vesicles [86] (Fig. 1.3). In other cases, cytoskeletal motors can act collectively such as in the formation of membrane nanotubes [9, 35], the dynein coordination in motile flagella able to propel a cell [66, 77] or the billion of myosins that working in coordination contract muscles [23].

Additionally, cytoskeletal tracks, namely, microtubules and actin can act as motor themselves by generating a force through its active polymerisation and depolimerisation. This force has also many functions as its the case of cell motility by lamellipodia [78].

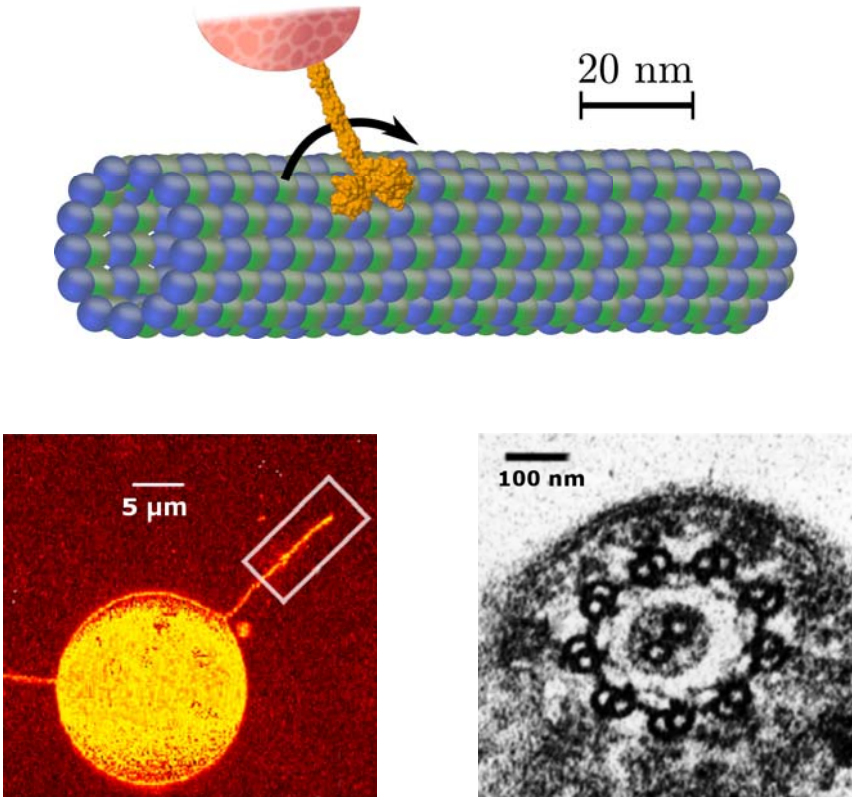

Figure 1.3: Examples of cytoskeletal motors. Top: Kinesin transporting a cargo along a microtubule. Kinesin surface reconstructed from 1N6M file from PDB. Bottom left: Confocal image of a membrane nanotubule extracted by cooperation of several kinesins from a vesicle located in a microtubule network. Image extracted from [9]. Bottom right: Transmission Electron Microscopy of the cross section of a flagellum from *Trimastix pyriformis*. The radial structure of the flagellum comprises a ring of 9 microtubule pairs and a two central microtubules. The different microtubules are actively linked by dyneins that produce a coordinated shear between microtubules generating the oscillations of the flagellum. Image extracted from [48].

A second large group of molecular motors contains those manipulating molecules. In general this manipulation consists in the catalysis of the synthesis or degradation of molecular complexes. In this case, the input and the output energy is, usually, chemical energy. However, in order to perform its function there is always an active mechanical deformation of the structure of the motor. This group contains all the machines in charge of the DNA translation process: the chromatin remodellers unwrap the DNA that is unzipped by the helicase. Following it, the single stranded DNA is transcribed into RNA by the DNA-dependent polymerase. Finally, the translation process is driven by the ribosome that synthesises the protein.

Other motors in the same group are in charge of manipulating smaller molecules. This is the case of the ATP-synthase that energises the cell by resynthetisising ATP molecules in the cell. This motor will be one of the main aims of study of the current work and its description is retaken in more detail in Sec. 1.3.1.

Finally, the last group of machines is located at biological membranes. Membranes are natural walls dividing the cell and can control the molecular transport across them. This last group contains the transmembranal machines that act as an active translocator for different molecules across the membrane. Each translocation machine is devoted to transport a specific molecule ranging from ions to DNA. The role of the translocators is not only to act as a passive channel but also to provide very large forces as it is the case of the DNA-packaging motor found in many viruses [39].

The motor classification chosen takes into account the final output of the motor disregarding the necessary energetic input. A classification according to the

input would reveal three different energetic natural inputs in the cell. The main energetic source is the hydrolysis of ATP or other nucleotide derivatives. Such molecules are found in an unstable energetic state that require a long time to be hydrolysed. This time is long enough to diffuse around the cell and arrive at a molecular machine. Molecular machines act as catalysers of its hydrolysis reaction taking the most of the released energy. A second source of energy is found in membranes. Membranes can maintain different ionic concentration at each side. Hence, keeping at both sides a difference in electrostatical and chemical energy. Thus, in the presence of an ionic channel across the membrane, a directional flux of ions can take place. Some transmembranal machines can use this flux of ions to extract energy from it. Finally, a third natural source of energy is presented directly in the form of mechanical work. Even though, the initial source of energy is usually chemical energy, intermediate processes, often between coupled motors, transmit their energy through mechanical work. The two main sources of chemical energy, ATP hydrolysis and ionic gradients are discussed in detail in Chapters 3 and 4, each section devoted to a certain energy input.

Despite the initial discussion about the relation of physics and biology, the high interest that physicists had in molecular motors arrived as a result of one important fact. Molecular motors are systems operating at a nanometric scale that could answer to old questions in physics. Specially those related with the energy management at the nanoscale, where the averages provided by thermodynamics or classical statistical mechanics must be revised. This, together with the advance in the last years on the manipulation of single molecules, has lead to several physical works on the topic [52, 64, 85]. Indeed, the physics leading subcellular processes is very different to the physics governing macroscopic machines, thus behaving counterintuitively. For instance, the importance of dissipative forces over inertial effects result in a low Reynolds number world completely

different to the one of macroscopic machines [61]. The lack of inertia in the subcellular world provides a scenario in which every movement of a body between two points requires to be assisted along the whole trajectory. At the very moment the driving input stops, the body will cease its directional advance. Additionally, the relevance of dissipative forces results in a high heat dissipation that must be managed wisely. It is also very significant the effect of thermal fluctuations in the motion of any body at the subcellular scale. The magnitude of thermal energy, of the order of pN nm, is comparable to other energetic scales of the system. The hydrolysis energy of ATP is 20 times the thermal energy and the usual energy of an ion crossing a membrane around 5 times [4]. Thus thermal fluctuations coming from the thermalisation of the particles conforming the surrounding media of any motor will always be relevant giving place to noisy trajectories where the instantaneous velocity of the motor will be larger than its average velocity. All this issues are thoroughly addressed and quantified in Chapter 2 where a theoretical framework for studying molecular motors is proposed making emphasis in the general aspects that differentiate the working machines at both scales.

Following nature, the human knowledge of nanoscience has allowed also the design of artificial molecular motors. So far, molecular motors created are much smaller than natural molecular machines but suggest an appealing future in the control of the nanoscopic world. Examples include nanocars driven by light or electrical impulses (Fig. 1.4), nanoswitches, or even nanomuscles [30, 33, 43]. Actually, experimental advances not only include the generation of artificial molecular motor from scratch but have also achieved the artificial modification of natural molecular motors. This is the case of the modified dynein created in Zev Bryant's group [10]. After the observation that the directionality of dyneins depended in the length of its neck, a dynein was devised with a contractile neck driven by external controllable inputs. Such inputs can be chemical such as the introduc-

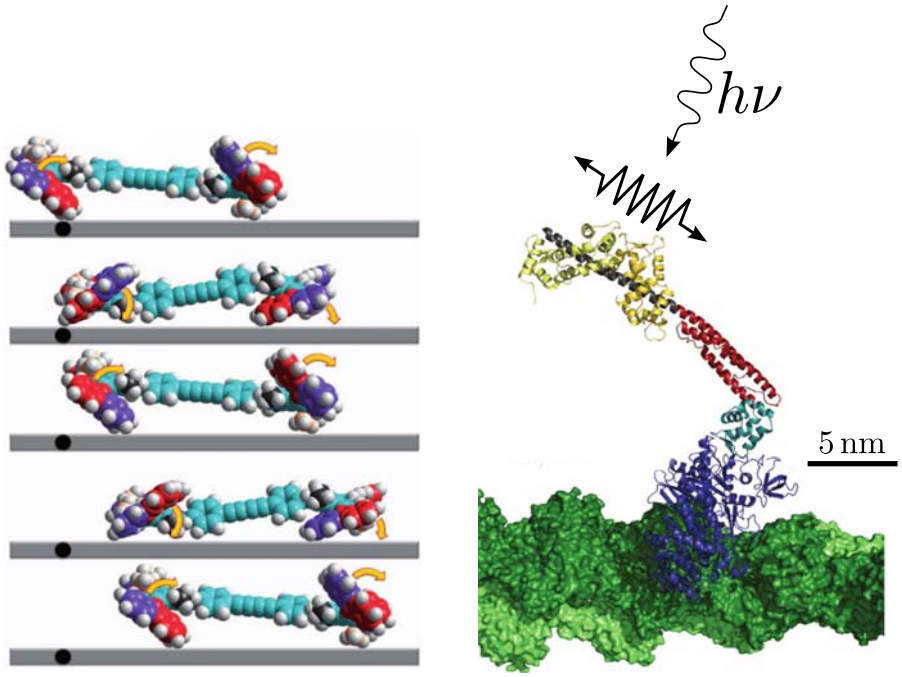

Figure 1.4: Examples of artificial molecular motors. Left: An organic nanocar developed experimentally by [33]. The nanocar consists on a rigid carbon chassis provided with two planar molecules at each side that can rotate. The directional rotation results from a chemical reaction driven by an electrical impulse supplied by an AFM microscope. Image extracted from [33]. Right: Modified dynein. The length of the neck can be provided with a light sensitive molecule, thus having a light controlled length of the neck. Since the length of the neck determines the directionality of the dynein along the actin filament, the motor results in a bidirectional controllable artificial molecular motor. Image extracted from [10].

tion of a certain substance in the sample, or physical, such as the control of the contraction of the neck with light. Thus, in this last case, the direction of advance of the dynein can be controlled simply by illuminating the sample (Fig. 1.4).

1.3. Rotatory Molecular Machines

This work is mainly devoted to the analysis of rotatory molecular motors *i.e.* molecular machines that involve a rotatory motion in its operation. Actually, the best known examples are ATP synthases and the Bacterial Flagellar Motors. Also motors working with double-stranded DNA such as helicases or DNA-translocators can be considered rotatory motors since they work on the twisted DNA helix. However, the current work will only focus in the two former cases, studying more exhaustively the ATP synthase.

1.3.1. F_0F_1–ATP synthase

ATP, often called the energy currency of the cell, arrives at the catalytic sites of different motors through diffusion along the cell. Altogether, so many subcellular processes extract energy from ATP hydrolysis that the ingest of each necessary ATP molecule is unfeasible for any living system. Actually, an human being uses each day an amount of ATP comparable to its own weight [8]. Nevertheless, cells have a solution for this problem: the recycling of the hydrolysis of ATP waste products. This process occurs in the F_0F_1–ATP synthase which is able to take the hydrolysis products of ATP, namely, ADP and phosphate (P_i), and join them back generating a new active ATP molecule. Clearly, the energy necessary for the ATP synthesis is not free. F_0F_1–ATPsynthase is located at a membrane obtaining its energy from the Proton Motive Force of ions crossing

this membrane. In eukaryotic cells, the F_0F_1–ATP synthase is found in the inner membrane of the mitochondria, it can also be found in cloroplasts of plants and algae, while in prokaryotic cells is found in the plasma membrane. Here a new question arises, where does this membrane proton potential comes from? In this case, the membrane potential is the outcome of a set of complex electron transport chains resulting from processes such as the oxidation of food or light absorption *i.e.* from the processing of cell's external energetic input [4]. Thus the role of F_0F_1–ATP synthase is not that of generating energy but transducing the local energy of a membrane potential into an energy carrier in the form of ATP able to travel along the cell.

Another particular characteristic of F_0F_1–ATP synthase is the way energy is transferred from the ionic potential to the ATP molecule. The energetic transduction takes place following two coupled mechanisms that take place at different parts of the motor. These parts are the transmembranal subunit F_0 and the globular hydrophilic subunit F_1 (Fig. 1.5). The hydrophobic part F_0 consists of a channel that spans all the membrane and a rotor (c-ring). Both parts, channel and rotor are coupled transforming the spontaneous flux of ions across the channel into a directional rotation of the rotor. Thus, the F_0 subunit works as a turbine transducing a flux into a rotatory motion. The F_0 subunit is attached to a central asymmetric shaft (γ shaft) that transmits the rotation along the motor to the F_1 subunit. The F_1 globular subunit, unable to rotate, surrounds the asymmetric shaft. This way, the rotation of the F_0 subunit is transmitted to the F_1 subunit as an internal mechanical deformation of the F_1 subunit through the shaft. This internal mechanical deformation is the input energy that the F_1 subunit, that is affine to ADP and P_i, uses to synthesise ATP.

Thus, F_0F_1 is a molecular machine composed itself by two well differentiated

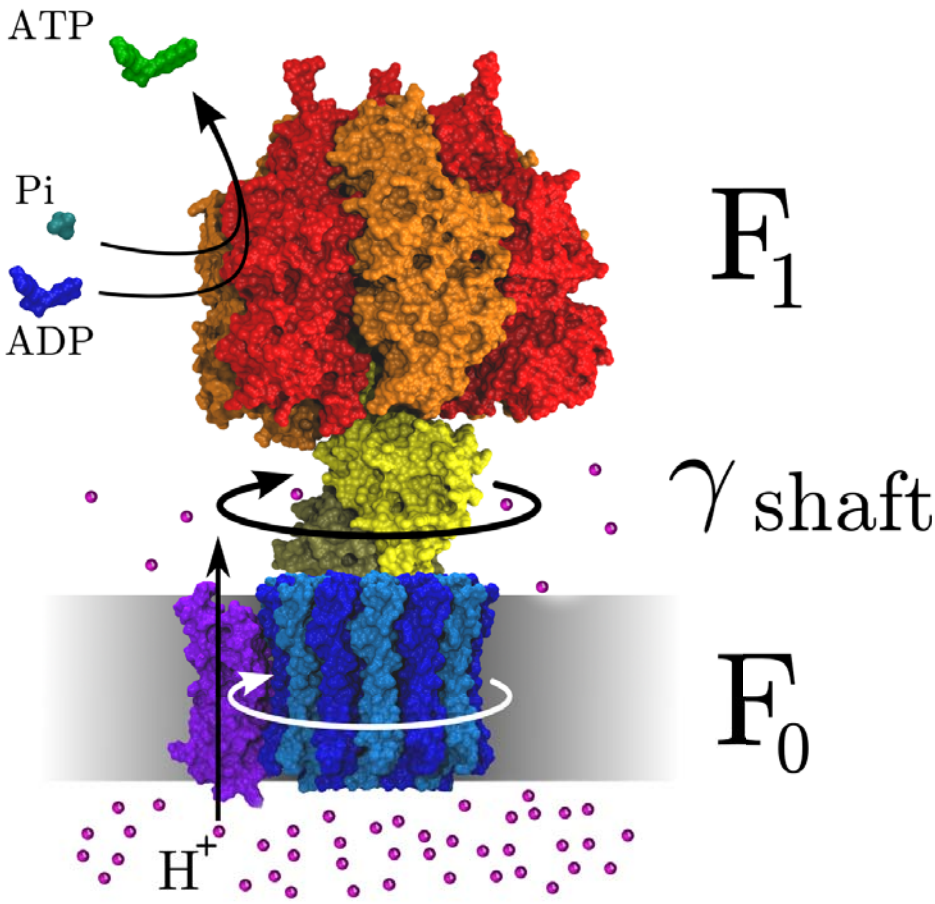

Figure 1.5: F_0F_1–ATP synthase molecular motor. F_0 subunit works as a turbine with a flux of ions H^+ ions through the stator (*stator*) inducing a rotation in the c-ring rotor (*blue*). The rotation is transmitted through the γ shaft (*yellow*) interacting with the F_1 subunit (*orange and red*) where the ATP synthesis takes place out of its hydrolysis products ADP and phosphate. Surface plot of protein based on structures 1Q01 and 1C17 from PDB.

machines, the F_0 and the F_1. This classification is not only an artifact. Both motors can be isolated in the lab where they can operate separately. Thus, the subunit portion F_0 could be employed in the lab to attain a usable rotational motion, or one can synthesise ATP by rotating the γ shaft of F_1 motor with magnetic tweezers. Additionally both motors are also reversible in the sense that they can transduct energy in opposition to their natural direction. F_0 can pump ions when a strong enough torque is applied on it and F_1 can act as a motor hydrolysing ATP to rotate the γ shaft. The direction of the transduction will depend on the energetic balance between the driving forces [29]. Among both motors, F_1 in its hydrolysis regime has been the more studied one since it is hydrophilic and its operation does not require the application of any external torque [96]. For this reason, when the F_1 motor is isolated, it is often referred as F_1–ATPase. The operation of F_1–ATPase is analysed in depth in Chapter 3.

1.3.2. Bacterial Flagellar Motor (BFM)

Often, bacteria need to propel around the media in order to look for more suitable conditions. Nature has found different solutions to this problem being one of them the propelling through flagella. Bacterial flagella are very different to eukaryotic ones. Eukaryotic flagella consist on soft long tails that oscillate through the active action of coordinated dyneins[66]. In contrast, bacterial flagella are rigid helical structures that are rotated by a molecular motor located at the joint between the flagellum and the bacteria, the Bacterial Flagellar Motor.

BFM is one of the largest molecular motors in the cell consisting on a rotor of $\sim$ 50 nm diameter crossing the inner and outer membranes of the bacteria where different stators can attach. As it happens with the F_0 motor, the stators

(Mot A/B or Pom A/B) consist on transmembrane channels coupling a electrochemically ion driven gradient with the rotation of the motor. Thus, with the force supplied by the different stators, the BFM can achieve angular velocities of 100.000 rpm, which is faster than the engine of a Formula 1 car [7]. However, the rotation of the BFM is not continuous. Instead, bacteria of different strains have developed different strategies such as changes in the velocity, stopping or even changing the rotation direction of the rotor. This, together with thermal fluctuations, allows bacteria to explore the extracelullar medium in the research for food. This mechanism is known as *chemotaxis* [4].

In contrast to the F_0 motor the stators of the BFM are not fixed to the motor. Instead, the bacterium contains a pool of stators that attach and detach continuously from the rotor with an average attached time of $\sim$ 1 minute. This mechanism can help bacteria to control the velocity and the energy transmitted to the rotor depending on the requirements of the bacteria [63].

As it happens with the ATP-synthase, BFM also shows a certain degree of modularity. In this case, different components of the BFM motor original from different bacterial strains can be mixed together generating different functionally BFM chimeras. For instance the stators of the BFM of the *V. alginolyticus* strain (proteins PomA and PomB) that work with a flux of Na^+ can be replaced by the stators of *E. coli* (proteins MotA and MotB) that work with a flux of H^+, resulting in a functional rotation chimeric motor [79]. This picture of different attaching/detaching motors that can act on the same track (in this case the rotor) is not specific of BFM but have several similarities to the kinesin and dynein motors walking along the microtubule filaments, which, in many scenarios, can also act cooperatively.

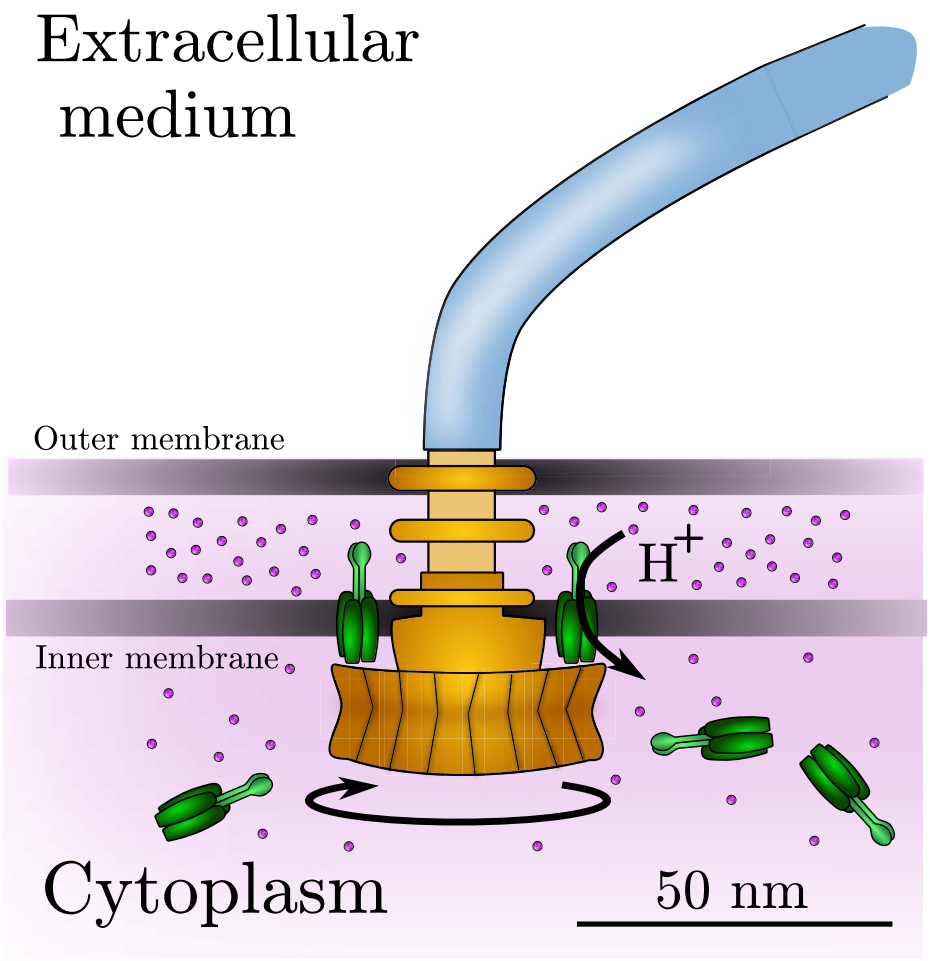

Figure 1.6: Bacterial Flagellar motor. The motor is composed by a rotor (*orange*) spanning the membrane of the bacterium and a set of stators (*green*) that only span the inner membrane. The stators are not fixed to the membrane. Instead, stators from a pool attach and detach continuously. In the figure, two stators are attached. The stators obtain energy from the flux of ions (not in scale) across the inner membrane. The energy is transferred to the rotor that transmits the rotation to the flagellum (*blue*) that is elongated outside the bacterium. Scheme inspired in [7].

To sum up, this introduction section points out the correspondence of physical and biological sciences. This becomes evident for the study of biological molecular machines. Additionally, this coupling reveals multiple outlooks in the study of molecular motors. Therefore, next chapter is dedicated to describe the methodological approach used along this work. Following on, Chapters 3 and 4 will be devoted to apply this methodology to the analysis of particular molecular motors and particular issues of cellular energy transduction. Finally some conclusions and perspectives are provided.

2

Biophysical methodology for rotatory molecular motors

Even though there is a high variety of molecular motors, all of them share common basic principles set by the physico–chemical environment in which they work. These shared properties allow to formalise a common theoretical framework that allows to tackle the comprehension of molecular motors. Hence, this chapter is devoted to set the theoretical framework used along the rest of the manuscript. Establishing a description formalism is important since alternative theoretical approaches available in the literature are multiple [12, 88]. Every theoretical approach designed to tackle a certain kind of molecular motor from a different description level. Particularly, this work is devoted to rotatory molecular motors, therefore, the current framework will lay a especial emphasis on this kind of motors. Actually, the physical magnitudes measured will be rotatory, such as angles and torques. Once the theoretical description of molecular motors is developed, it will settle the basis for the study of specific rotatory molecular motors in Chapters 3 and 4.

2.1. Stepping and cycles

The most usual experimental approach to study molecular motors consists in tracking the spatial advance $\theta(t)$ of the molecular machine. Such experiments reveal that the operation of molecular motors is based in the same principle as their macroscopic counterpart. Both operate through closed energy transduction cycles. During each cycle the motor transduces a certain amount of energy and advances a fixed spatial length θ_0. Even though the task of the machine is not to achieve a net movement, there is always a motion of the motor associated with the transduction process. This is the case of the full complex F_0F_1–ATP synthase, which requires a rotation of the F_0–γ subunit in order to attain the transduction of an ionic gradient into the catalysis of the ATP synthesis reaction.

The spatial periodicity θ_0 of the cycle comes fixed by the biomolecular structure of the motor. For linear motors, the structure is usually constrained by the track of the motor *e.g.* the 8 nm symmetry of the tubulin, usually, track of kinesins and some myosins. Rotatory motors are a different case since the track is the motor itself and therefore the distance (actually an angle) θ_0 comes determined by the quaternary structure of the protein. For rotatory motors this structure is accomplished through the circular aggregation of equivalent domains that not only give the motor its rotational symmetry but also a functional track. Thus, this symmetry is the one that selects the angle θ_0. For instance, in the case of the F_1, constituted by three $\alpha\beta$ subunits, the symmetry is a third of a turn. This is shown in Fig. 2.1 together with other rotatory molecular motor examples.

Out of this classification fall other molecular machines, not motors, that operate in close structural configuration cycles. Such machines do not produce a net displacement once the cycle is closed. An example of such machines is the Na^+/K^+–ATPase which through a cyclic movement translocates actively sodium

and potassium ions across the plasma membrane. Even in this case, the evolution of an associated configuration coordinate $\theta(t)$ can be defined, and with it a a cycle length θ_0.

The identification of θ_0 is not always straightforward. This is the case of motors with multiple stators where several cycles can happen at once, as it happens with the BFM [79] or simply motors for which the experimental observations are still incapable of resolving the different cycles of the motor. In these cases, the distance θ_0 is hidden from the observation of the motor trajectory $\theta(t)$.

On the other hand, besides θ_0, the time necessary to complete the cycle depends on the whole set of physicochemical processes occurring during the cycle. Hence, each cycle of length θ_0 and average duration $\mathcal{T}$ can be divided in subprocesses, each i-th subprocess of length θ_i and duration t_i. Again, the spatial length of each subprocess is determined by the different structural configurations of the motor at each stage,

$$\theta_0 = \sum_i \theta_i. \tag{2.1}$$

On the contrary, the duration of each subprocess results from the chemical and physical reactions defining the process. Thus, in contrast to the lengths θ_i, the duration of the processes t_i does not require to be deterministic and are usually stochastic conditioned to the actual nature of the process as is showed later on along this work. However, since each subprocess composes an independent part of the cycle, the average duration of the cycle can be expressed as the sum of the average times of each individual process,

$$\mathcal{T} = \left\langle \sum_i t_i \right\rangle = \sum_i \langle t_i \rangle. \tag{2.2}$$

Even though all the processes take a finite time, not all of them involve a net spatial advance of the motor. Such processes are related with catalytic events during which caption or release of molecules occurs, or chemical reactions un-

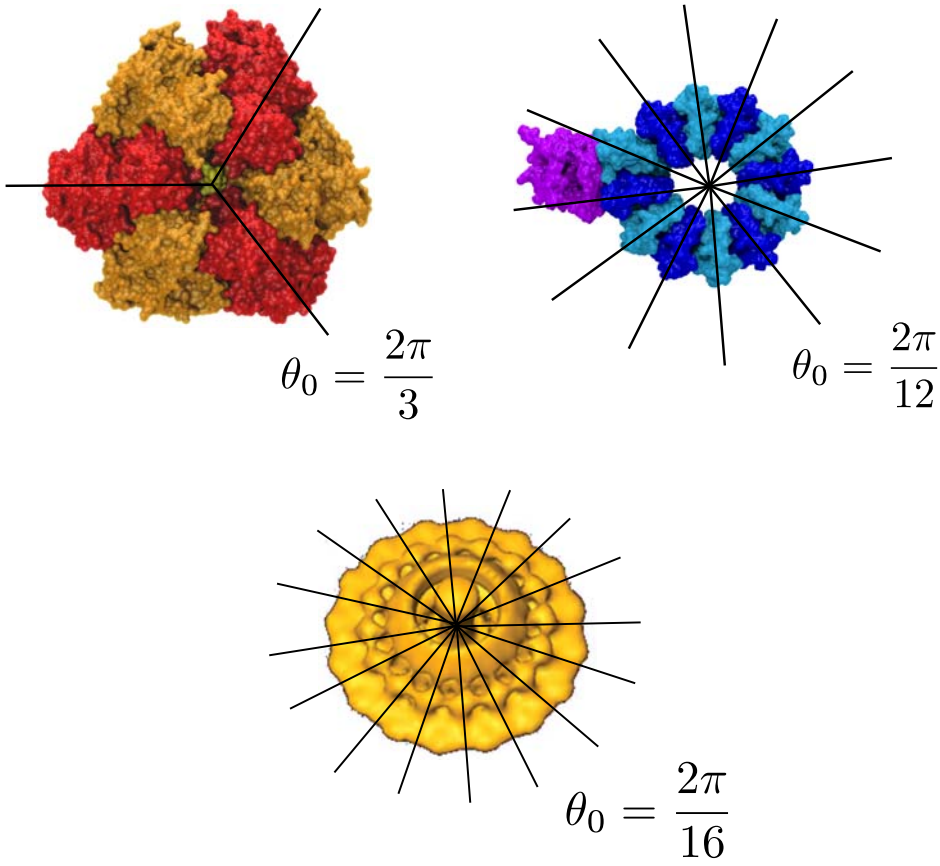

Figure 2.1: Examples of cycle angular lengths coinciding with the symmetry of the motor. Top left: F_1 subunit of yeast. Top right: F_0 subunit of *E.Coli*. Bottom: Bacterial Flagellar Motor of *Treponema primitia*. ATP–synthase surface structure reconstructed from information of PDB structures 1QO1 and 1C17. BFM figure extracted from [45]

coupled to the motion coordinate take place. Hence, during these processes with no change in the configuration of the motor relative to the spatial coordinate, the motor "waits" for this process to finish in order to continue the transduction. Since such processes do not entail any net movement, they are referred as *dwells* and their duration as *dwell times*. They can also be referred as *chemical processes* due to its catalytic nature. Both nomenclatures are used along the text. In comparison, processes that do involve a net displacement are referred as *mechanical processes* since a net force is acting on the motor generating an advance. The alternation of mechanical processes and dwell processes procure the typical stepping trajectories observed in molecular motors (Fig. 2.2). Indeed, each motor cycle can be composed by several steps corresponding to different mechanical and chemical processes. In practice, each step is considered only as such when there is enough experimental precision to observe it. A long mechanical process may divided in smaller mechanical processes separated by short dwell processes not resolved experimentally. As a particular case, the F_1–ATPase was initially observed to operate with steps of a third of a turn while the increasing in the temporal recording precision to the millisecond scale showed that each step is divided in two substeps of $\sim 80^0 - 40^0$, each one consisting in one dwell and one mechanical process (Sec. 3.1).

Due to the catalytic nature of dwell times, they appear naturally as the inverse of chemical rates and can be studied through the well known reaction kinetics theory. However, this must be done carefully since classical reaction kinetics has been developed during most part of twentieth century as the result of an average over large amount of molecules conforming the studied sample. Nevertheless, during the current century, the later advances in single–molecule techniques have provided a new insight into the nature of the kinetic reactions studying the mechanisms by which two individual diffusing molecules find each other and how the

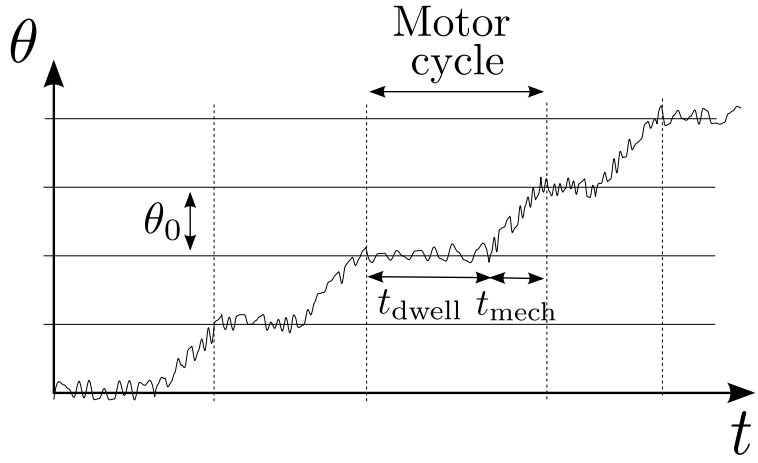

Figure 2.2: Scheme of a trajectory of a molecular motor. Each cycle of length θ_0 spanning a different random time (*discontinuous vertical lines*). In this case, each cycle is composed by two subprocesses, one dwell and one mechanical stroke producing the step–like trajectory.

intermediate reaction products take place until the reaction is complete. All this information was not fully accessible through the study of an ensemble of unsynchronised molecules. This new insight provides additional statistical information of the reaction times which are naturally stochastic. This stochasticity affects directly to the transduction cycle duration and may also affect to the actual performance of the motor. Therefore, understanding the dwell times of molecular motors requires not only the average value of the dwell times but also the knowledge of their statistical properties [41].

The simplest reaction mechanism corresponds to the situation in which the motor (M) must react with a certain substrate that is diffusing in the media (S) such as ATP in the process of ATP caption.

$$\mathrm{M} + \mathrm{S} \xrightarrow{\mathrm{k}} \mathrm{MS}. \tag{2.3}$$

In this situation the probability of an ATP diffusing into the motor is constant in time and proportional to the concentration of substrate $k[S]$ and therefore the reaction can be described as an exponential process,

$$P(t_{\text{dwell}}) = \frac{\mathrm{e}^{-k[S]t_{\text{dwell}}}}{k[S]}, \tag{2.4}$$

with a mean dwell time,

$$\langle t_{\text{dwell}} \rangle = \frac{1}{k[S]}. \tag{2.5}$$

This result is equivalent to the ensemble counterpart *i.e.* a first–order reaction describing the decay of concentration of the substrate. However, both processes, the substrate caption and the first–order reaction are different. The first–order reaction describes how an amount of substrate (several molecules) react continuously in the excess of a certain reactive, while the current case describes a single reaction of a molecule from an ensemble with a single motor.

Once, the molecule caption occurs, different internal reactions may take place in the ligand–protein complex (MS) before the motor is ready to begin the mechanical stroke (MS'),

$$\mathrm{M} + \mathrm{S} \rightleftharpoons \mathrm{MS} \rightarrow \mathrm{MS}'. \tag{2.6}$$

This set of reactions depends on the actual nature of the processes necessary to prepare the motor and may have different distributions that in average result in a dwell time,

$$\langle t_{\text{dwell}} \rangle = \frac{1}{k[S]} + t_0. \tag{2.7}$$

Where t_0 is a constant time independent of the substrate concentration. This description states that the total dwell time is the result of two contributions: the time that takes the substrate caption and the time spanned by a set of internal reactions that do not depend on the concentration of the substrate of average duration t_0. The average dwell time expression (2.7) coincides with the inverse of the reaction velocity of the Michaelis–Menten enzymatic reaction

scheme. Actually, Michaelis–Menten kinetics result from a particular case of the reaction kinetics of (2.6). However, in the current case the result is more general, expressing the average dwell time as the addition of two processes, one depending on the substrate concentration and another that doe not depends on it. As stated before, equation (2.7) contains only a partial information about the dwell times, and for each particular case, the different processes composing the dwell time must be analysed leading to different time probability distributions.

The kinetic description could also be extended to the description of mechanical times through a set of reactions describing the conformational changes taking place during the transduction [5, 12, 88]. Actually, some molecular motor models deal with all the dynamics through a set of reactions between a set of different conformational states. This simple approach returns easy analytical and numerical solutions and describe well the motor when the mechanical times are short compared with the dwell times. However, this approach fails to introduce in the description of the motor, dynamical magnitudes such as external torques applied on the machine. On the other hand, in contrast to the pure kinetic model, the motor can be described through and all atom molecular simulation in which every atom composing the protein together with the ligands and the surrounding molecules are taken into account. This description requires an exhaustive calculation over all the forces that take place between the different constituents of the motor every integration step with an accurate time resolution. Although this is the most realistic description, actual computation facilities are unable to reproduce the behaviour of the motor during a long enough time to reproduce several transduction cycles [62]. Even more important, the all atom simulation does not allow to find analytic results that help to understand the fundamental mechanisms that drive the motor. The models proposed in this work take into account an intermediate scenario in which all the forces are averaged to the effect over a single spatial coordinate θ directly related with the motion observed exper-

imentally [13, 88]. This dynamics is developed in the next section. In this level of modelling, also kinetic reactions will be taking into account in the description of the dwells. Despite all the different models available, there is no optimum model, all of them leading to different insights of the motor, every model drawing a bit of the complete whole picture of the working of these complex machines.

2.2. Forces and Velocities

Molecular Motors are subject to a very different scale than their macroscopic equivalents. This change in scale not only sets the units in which the magnitudes are described, but also the nature of the different relevant forces/torques that drive their dynamics. Particularly, the small size of molecular motors increase the relevance of the surface interaction of the motor with the surrounding molecules. As it happens with a macroscopic body, a motor advancing through the medium collides continuously with the surrounding molecules composing the medium. The average reaction torque produced by the molecules always opposes the motion and can be assumed to be proportional to the velocity $\tau_{\text{drag}} = -\gamma\dot{\theta}$, where γ is the proportionality coefficient called rotational friction coefficient. A body of inertia moment I rotating under a constant torque τ_0 and the corresponding drag force presents a exponential velocity profile solution for the corresponding Newton's second law

$$I\ddot{\theta} = \tau_0 - \gamma\dot{\theta} \qquad \rightarrow \qquad \dot{\theta} = \frac{\tau_0}{\gamma}\left(1 - \mathrm{e}^{-t/t_\gamma}\right), \tag{2.8}$$

where the timescale $t_\gamma \equiv I/\gamma$ states two different behaviours for the particle. For times lower than t_γ, the particle follows the well known linear angular velocity of an uniformly accelerated motion $\omega = \frac{\tau_0}{I}t$. In contrast, for times above t_γ the body is found in an overdamped regime in which velocity saturates exponentially to a steady state value $\omega = \frac{\tau_0}{\gamma}$ known as the limit velocity. This limit velocity is

independent of the inertia moment I and therefore is independent of the mass of the body. Because of this, the time scale t_γ is known as the time scale of inertia. A similar result can be found for the linear motion case in which $t_\gamma = \frac{m}{\gamma_x}$, being m and γ_x the mass of the body and the linear friction coefficient respectively. To understand the relevance of t_γ in molecular motors dynamics, it can be estimated for a sphere of radius r advancing straight through aqueous medium,

$$t_\gamma = \frac{m}{\gamma} = \frac{\frac{4}{3}\pi\rho r^3}{6\pi\eta r} = \frac{2\rho}{9\eta}r^2, \tag{2.9}$$

where the volume of a sphere of density ρ and the Stoke's linear friction coefficient of a sphere surrounded by a medium of dynamical viscosity η is used. Thus, for a body of a typical size of r=100 nm, a density comparable to water density $\rho = 1000\ \mathrm{kg/m^3} = 10^{-15}\mathrm{pN\,ms^2/nm^4}$ and the viscosity of water $\eta = 1\mathrm{cP} = 10^{-6}\mathrm{pN\,nm^{-2}ms}$ results in a time scale of inertia of $t_\gamma = 0.2\mu\mathrm{s}$. This value for the time scale of inertia is far smaller than the typical processes occurring in molecular motors, usually in the millisecond scale. Therefore, the relaxation to the limit velocity can be considered instantaneous. This fact results in a velocity profile that at all times is proportional to the exerted force.

The drag force is not the only way in which the fluid particles interact with the motor. Since the fluid molecules surrounding the motor are thermalised, they are in motion continuously, colliding with the motor even when no driving force is present ($\tau_0 = 0$). This results in a stochastic force $\xi(t)$ of zero mean $\langle\xi(t)\rangle = 0$ acting constantly on the motor. This force, known as Brownian force, can be described through a delta–correlated Gaussian process [21] with an autocorrelation (noise intensity) obtained from the equipartition theorem,

$$\langle\xi(t)\xi(t')\rangle = 2\gamma k_B T\delta(t - t'). \tag{2.10}$$

Hence, the intensity of the Brownian force is proportional to the friction coef-

ficient γ, which is a measure of the interaction of the body with the fluid, and $k_B T$, the thermal energy, which is a measure of the kinetic energy of the particles composing the fluid.

The Brownian force can be introduced in Newton's Second Law in the overdamped regime $t \gg t_\gamma$ resulting in the overdamped Langevin equation

$$\gamma \dot{\theta} = \sum_i \tau_i(t) + \xi(t), \tag{2.11}$$

where the constant torque τ_0 has been substituted by the sum of all the torques acting on the motor at a certain time t. Note that derivation of equation (2.11) is not straightforward since the thermal force changes rapidly in time and cannot be considered slower than t_γ. A more rigorous derivation of (2.11), also known as Einstein–Smoluchousky limit, can be found in [67, 88].

The term in (2.11) describing all the remaining torques $\sum_i \tau_i$ can be further divided in two different sources. The torques generated by the motor in its natural working τ_{in}, and the torques applied by an external agent τ_{ex}, which is the case of the experimental forces applied to study the motor. The torque generated by the motor τ_{in} contains the mechano–chemistry of the motor and understanding the response of τ_{in} to the different set of experimental parameters is one of the main objectives of this theoretical approach,

$$\gamma \dot{\theta} = \tau_{\text{in}} + \tau_{\text{ex}} + \xi(t). \tag{2.12}$$

The torques applied by an external agent can be classified, in turn, in two different kind of torques. Conservative torques τ_{c} that can be used to extract or introduce mechanical work from the motor, and dissipative torques, such as the dragging of an attached load, that are immediately dissipated to the bath. Usually, the attached load link is strong enough to consider the load–motor a rigid entity. In this case, the resulting drag force is the corresponding to a new larger effective

friction coefficient,

$$\gamma_{\text{eff}}\dot{\theta} = \gamma_0\dot{\theta} + \gamma_L\dot{\theta}. \tag{2.13}$$

Where the subindexes label the natural internal friction of the motor γ_0 and the friction coefficient of the load γ_L, resulting in a new Langevin equation,

$$\gamma_{\text{eff}}\dot{\theta} = \tau_{\text{in}} + \tau_{\text{c}} + \xi(t). \tag{2.14}$$

The load link stiffness may not be rigid, in this case two spatial variables, one for the motor and one for the load becomes necessary. This situation is further analysed in Chapter 3. Despite the considerations on the nature of τ_{ex}, mathematical expressions (2.12) and (2.14) are identical. Therefore, the analysis is continued directly with (2.14) without losing generality. However, the more general expression (2.12) will be invoked when necessary.

Langevin equation (2.14) will be the starting point in the stochastic description of the trajectories of molecular motors in this manuscript. This equation is not only useful because it contains all the dynamics of the motor allowing to describe the performance and the energetics of the motor, but also because of the simplicity to solve it numerically reproducing stochastic trajectories.

The first observable that can be extracted from (2.14) is the average angular velocity of the motor over time,

$$\omega \equiv \left\langle \dot{\theta} \right\rangle = \frac{\langle \tau_{\text{in}} + \tau_{\text{c}} \rangle}{\gamma_{\text{eff}}}, \tag{2.15}$$

where the Brownian force is cancelled in average. Nevertheless, effects due to the Brownian force are still present through the value of τ_{in} that will generally depend on the trajectory $\tau_{\text{in}}(\theta, t)$.

On the other hand, the average velocity can be related to the purely kinetic observables as the average displacement per unit of time,

$$\omega = \lim_{t\to\infty} \frac{\theta(t)}{t} = \frac{\theta_0}{\mathcal{T}} = \frac{\sum \theta_i}{\sum \langle t_i \rangle}. \tag{2.16}$$

The average velocity can be thus constructed from the information of the step length θ_0 and the average duration of the different processes composing a full cycle $\mathcal{T}$ [14]. In (2.16), also the relation of the mean velocity with the subprocesses composing each cycle is explicited using relations (2.1) and (2.2). Hence, from expressions (2.15) and (2.16), arises a relation between the experimental observables θ_0 and $\mathcal{T}$ with the still unknown internal dynamics of the motor,

$$\langle \tau_{\rm in} \rangle = \frac{\gamma_{\rm eff}\theta_0}{\mathcal{T}} - \langle \tau_{\rm c} \rangle. \tag{2.17}$$

This expression is also valid to describe different subprocesses of the full transduction cycle, by changing the kinetic observables θ_0 and $\mathcal{T}$ by its corresponding subparts θ_i and $\langle t_i \rangle$. Explicitly, this returns a formal relation for the mechanical times with the different torques

$$\langle t_{{\rm mech}\,i} \rangle = \frac{\gamma_{\rm eff}\theta_0}{\langle \tau_{\rm in} \rangle + \langle \tau_{\rm c} \rangle}, \tag{2.18}$$

where the average for $\tau_{\rm in}$ and $\tau_{\rm c}$ spans the duration of the mechanical subprocess.

2.3. Energy and Ratchets

Up to this point, all the dynamics of the motor has been studied from its trajectory. However, a formal description of a molecular motor can also be tackled from its energetic task. This is, to transduce a certain amount of supplied energy from a source into an energy of different nature. An appropriate starting point for such a description is the energy balance of the motor (Fig. 2.3). The reference framework is the the first principle of thermodynamics, which can be written for any motor trajectory as [52, 74],

$$\Delta V = W + \Delta G - Q. \tag{2.19}$$

Here ΔV is the internal change of energy of the motor, Q is the heat interchanged

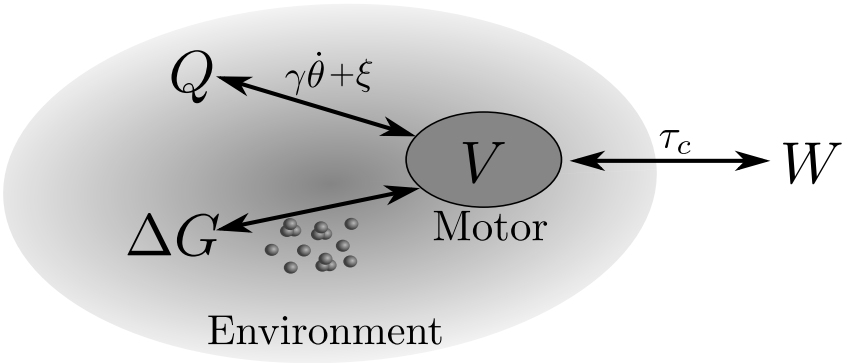

Figure 2.3: Energetic balance for a Molecular motor. The three energies W, ΔG, and Q are transduced through the motor potential V.

with a thermal bath at fixed temperature T and $W + \Delta G$ the thermodynamical work, *i.e.* all the energy supplied to or extracted from the system different from the heat. Here, the thermodynamical work is separated in two different contributions. On the one hand, W, the mechanical work, which is the performed work through an external force and the associated net motion of the motor. This is the energy supplied or extracted by an external agent such as the action of optical tweezers in the experimental setup. On the other hand, ΔG is the chemical free energy product of the chemical reactions of molecules different from the motor taking place in the transduction such as the ATP hydrolysis.

The sign convention chosen states that the thermodynamical work is positive $(W, \Delta G > 0)$ when energy is introduced in the system while in contrast, Q is the energy that leaves the motor in form of heat and therefore $Q > 0$ means that heat is leaving the motor.

Therefore, for molecular motors, the internal energy V is the energy accumulated in the motor during a transduction cycle. Thus, for instance, an ATP hydrolysis process starts with a sudden increment of the internal energy of the

motor which afterwards is transduced into useful energy and heat. The spatiotemporal description of the internal energy $V(\theta, t)$ will describe how the motor administrates the energy describing the dynamics of the motor as a minimisation of the internal energy along space and time. Thus, the internal energy will be referred hereon as *motor potential*, and the associated force will be the *motive torque* related through,

$$\tau_{\text{in}} = -\frac{\partial V(\theta, t)}{\partial \theta}, \tag{2.20}$$

where τ_{in} is the internal motive torque previously introduced in (2.12). Therefore, $V(\theta, t)$ contains all the information of the behaviour of the motor. Finding the shape and dependence of $V(\theta, t)$ is, thus, one of the main objectives in understanding the working of a molecular motor.

The exploration for a possible expression for the motor potential reveals, before long, that multiple possible definitions for $V(\theta, t)$ arise, and will depend on the degree of abstraction of the model. A reasonable approach, followed in the current manuscript, is to minimise the invocation of artificial structures looking for the minimum model able to describe the experimental information available taking as variables the angular coordinate, the time and the chemical state of the motor.

Some of the properties of molecular motors discussed in the previous sections come in handy to solve this issue. This set of physical and chemical conditions common to rotatory molecular motors can be used to fix some properties of the shape of the motor potential and gives a starting framework for the research for a motor potential. One ubiquitous property is the spatial periodicity of the generated motive torque with a period of the length of the step

$$\left.\frac{\partial V(\theta, t)}{\partial \theta}\right|_{(\theta,t)} = \left.\frac{\partial V(\theta, t)}{\partial \theta}\right|_{(\theta+\theta_0,t')}. \tag{2.21}$$

As stated in Sec. 2.1 the periodicity is not always fully achieved. In these cases, the periodicity of the motive torque relaxes and can be substituted by a an average torque for the case of an irregular track or by a potential of higher periodicity which in the case of rotatory molecular motors will not be larger than 2π. The periodicity of the motive force entails a periodicity of the spatial probability distribution of the motor in the stationary state which will be discussed later in Sec. 2.4.

Expression (2.20) relates the internal energy with the motor torque. Equivalently, the rest of the forces describing the dynamics (2.14) can be related with the energetics of the system (2.19) (Fig. 2.3) by integration along the spatial coordinate for a trajectory [74]. Thus, the external work supplied or extracted through the external torque τ_{c} is

$$W = \int_{t_i}^{t_f} \tau_{\mathrm{c}}(\theta, t)\mathrm{d}\theta(t). \tag{2.22}$$

The spatial integral covers the path of the full trajectory, which is stochastic and therefore will change in every realisation. This dependence in the trajectory is stated explicitly writing down the dependence of the position with the time in the angle differential $\mathrm{d}\theta(t)$ and integrating between the start and end times of the trajectory, t_i and t_f respectively.

Accordingly, the heat will be the resulting energy from the integration of all the forces that the motor exerts on the bath

$$Q = \int_{t_i}^{t_f} (\gamma\dot{\theta}(t) - \xi(t))\mathrm{d}\theta(t). \tag{2.23}$$

The relation of the integral expression of Q with the other forces of the system is available introducing (2.14) in (2.23) and using the previous equalities (2.20) and (2.22)

$$Q = \int_{t_i}^{t_f} \frac{\partial V(\theta, t)}{\partial \theta} \mathrm{d}\theta(t) - W. \tag{2.24}$$

On the other hand, the increment of motor potential in (2.19) can be explicitly expanded as

$$\Delta V = \int_{t_i}^{t_f} \mathrm{d}V = \int_{t_i}^{t_f} \frac{\partial V(\theta, t)}{\partial \theta} \mathrm{d}\theta(t) + \int_{t_i}^{t_f} \frac{\partial V(\theta, t)}{\partial t} \mathrm{d}t. \tag{2.25}$$

Here the integral along the spatial coordinate is the energy that the motor is transducing through the motive torque and the second integral can be identified introducing (2.23) and (2.25) in (2.19) obtaining,

$$\Delta G = \int_{t_i}^{t_f} \frac{\partial V(\theta, t)}{\partial t} \mathrm{d}t. \tag{2.26}$$

This equality is interesting since it points out explicitly that the chemical energy is introduced/extracted in the system by a variation of the potential in time. By contrast, the energy is transduced into/from other kinds of energy (either external work or heat) through a spatial motion of the motor along the potential. Therefore, when modelling the energy source in the description of the potential it is essential to control which is the temporal behaviour of the motor potential.

Traditionally, the two most studied frameworks for time dependent potentials for theoretical molecular motors are rocking potentials and flashing potentials [16, 64]. While in the first case the potential changes smoothly in time through a periodic function, for the flashing potential the change of potential occurs suddenly. This last case is of especial interest for molecular motors where changes in the structure of the motor, such as conformation changes due to ATP caption, occur in a much faster scale than the actual dynamics and kinetics of the motor.

For flashing potentials, the spatial and temporal description are separated allowing to describe the motor potential as a set of static potentials that are

interchanged in time,

$$V(\theta, t) = \sum_i V_i(\theta)\delta_{i,\eta(t)}, \tag{2.27}$$

where the subindex i runs over all the different static potentials composing the flashing mechanism, $\eta(t)$ is a stochastic function of time that returns the potential state of the motor at a given time t and δ is Kronecker's delta. This separation allows to compute the chemical energy directly from (2.26). For the sake of simplicity lets consider a trajectory that only presents a single flash at a time t_{flash},

$$\Delta G = \int_{t_i}^{t_f} \frac{\partial}{\partial t} \sum_i V_i(\theta)\delta_{i,\eta(t)} = \int_{t_i}^{t_f} \sum_i V_i(\theta) \frac{\mathrm{d}\delta_{i,\eta(t)}}{\mathrm{d}t} dt = V_{\eta(t^+_{\text{flash}})} - V_{\eta(t^-_{\text{flash}})}, \tag{2.28}$$

where it is used the fact that the time variation of Kronecker's delta only occurs during the flashing of the potential. As stated before, equation (2.28) reflects that the chemical energy reacts with the system only during the flashing of the mechanism and the amount of energy is equal to the variation of the motor potential during the jump. Expression (2.28) can be easily extended to a full trajectory with several jumps,

$$\Delta G = \sum_{\text{flash}} \Delta V_{\text{flash}}. \tag{2.29}$$

Being ΔV_{flash} the motor potential increment during each jump.

For instance, an ATP molecule arriving at an ATP hydrolysis motor, increases instantly the motor potential of the system $\Delta V = \Delta G$. If the transduction takes place, the increment in motor potential will be transduced into W and Q. It can also occur that the ATP molecule leaves the motor before any energetic reaction takes place. This results in a flashing to the initial motor potential state $\Delta V = -\Delta G$. In this example ΔG is the source of energy and W the useful

output. In other situations such as the F_1 motor in the synthesis regime, the input energy wold be the external work W and the useful energy would be accumulated in form of chemical energy ΔG of the ATP synthesis. Other situations such as machines exchanging between different sources of chemical energies are also possible within this scenario.

For the former case of a motor fuelled through chemical energy, the consumed energy can be measured directly from the output energy consisting on the output mechanical work plus the dissipated heat,

$$E_{\text{consumed}} = Q - W = -\Delta V + \sum_{\text{flash}} \Delta V_{\text{flash}}. \tag{2.30}$$

This is, that the consumed energy can be measured as all the variations that occur in the potential except the ones corresponding to the flashes. Numerically, consumed work defined this way is an easy measure since the problem is reduced to compute the increments in potential energy after each spatial step takes place. A similar formula is obtained to measure the consumed energy for a motor working with mechanical work as energy source, where the consumed energy will be

$$E_{\text{consumed}} = -\Delta V + W. \tag{2.31}$$

In order to study the performance of molecular motors, as it happens in their macroscopic counterpart, it is not only necessary to understand the energies involved in each step but also how these energies are managed in time. For each one of the energetic magnitudes abovementioned, an associated power can can be defined as the amount of that energy used per unit of time. Since motors operate in closed cycles, each power can be computed from the average energy used per

cycle. For instance, the output power can be calculated as,

$$P_{\text{out}} = \frac{\langle E_{out} \rangle_{\text{cycle}}}{\mathcal{T}}. \tag{2.32}$$

The efficiency of the motor can also be computed from the energetic framework developed as the ratio between the useful output energy and the total input energy for a long enough trajectory giving a measure of the amount of energy that is being transduced to the desirable amount of energy. This calculation is equivalent to consider the ratio between the output power and the input power,

$$\eta = \frac{E_{\text{in}}}{E_{\text{out}}} = \frac{P_{\text{in}}}{P_{\text{out}}}. \tag{2.33}$$

Efficiencies of different forces can also be computed independently measuring the ratio of the input energy that is transduced in a certain output. A particular case is the Stoke's efficiency, that measures the fraction of energy that is dissipated through the dragging of the load. The energy output of such a conversion is immediately dissipated to the bath, however it is useful to measure how effectively the input energy is devoted to the drag of the load [89].

2.4. Probability distributions and the Fokker–Planck Equation

Up to this point, all the mechano–chemistry of molecular motors is described through the theoretical reproduction of the observed trajectories by means of a Langevin equation. This description returns a set of stochastic magnitudes which usually are not easily handled. An alternative approach is to work directly with the evolution of the spatio–temporal probability profile $P(\theta, t)$ of the motor. Such a mathematical formulation for $P(\theta, t)$ allows an easier analysis in some important situations.

An equation describing the evolution of the probability density $P(\theta, t)$ can be derived directly for a Langevin dynamics [21, 22]. This is the Fokker–Planck (F–P) equation, which for the Langevin equation (2.14) with (2.20) reads,

$$\frac{\partial P(\theta,t)}{\partial t} = \frac{\partial}{\partial \theta}\frac{V'(\theta,t) - \tau_c}{\gamma_{\text{eff}}}P(\theta,t) + \frac{k_B T}{\gamma_{\text{eff}}}\frac{\partial^2}{\partial \theta^2}P(\theta,t). \tag{2.34}$$

This equation states that the evolution of the probability in time is the addition of two terms: a drift term that depends on the force $\tau_c - V'(\theta, t)$ and a diffusive term resulting from the Brownian motion, proportional to the diffusion coefficient $k_B T/\gamma_{\text{eff}}$.

In F–P equation (2.34) the cycle of the motor occurs through the change of the motor potential in time. However, for the flashing potential dynamics, the potential changes can also be addressed through a set of F–P equations for the probability density of each occupational state $P_i(\theta, t)$ inside each potential $V_i(\theta)$ composing the flashing potential. In this description, the flashing is introduced through a set of jump rates between the different states [22, 88]. Altogether, in this work, the F–P approach will be studied through the total spatial probability density evolution of (2.34) leaving the configurational changes directly in the temporal evolution of the potential.

F–P equation is a second order partial differential equation. Thus, in order to solve it, initial and boundary conditions are required. Altogether, even for a given set of conditions, an analytical solution is generally not available. The rest of the chapter is devoted to the study of some cases with analytical solution that are of special interest to study molecular motors where properties of the probability flux are known and used through Chapter 3. The analysis of the F–P equation is taken up again in Chapter 4 for the description of ionic turbines, to solve Mean First Passage Time problems.

2.4.1. Stationary probability

An alternative description of the F–P equation can be written through the probability flux $J(\theta, t)$, this is, the rate of variation of the probability density across a point θ at a certain time t. Since probability must be conserved through space and time, it follows the local conservation equation,

$$\frac{\partial P(\theta,t)}{\partial t} = -\frac{\partial J(\theta,t)}{\partial t}. \tag{2.35}$$

Introducing (2.35) in (2.34) the F–P equation is reduced to,

$$-J(\theta,t) = \frac{V'(\theta,t) - \tau_c}{\gamma_{\text{eff}}} P(\theta,t) + \frac{k_B T}{\gamma_{\text{eff}}} \frac{\partial}{\partial \theta} P(\theta,t). \tag{2.36}$$

The evolution of a diffusive a particle inside a well much higher than the thermal energy leads to an equilibrium distribution $P_{\text{eq}}(\theta)$ of the particle confined inside this well. This is usually the case of the motor along a dwell time, where the potential confines the motion of the motor in a energy minimum leading to the stall of the motor. Thus, during dwell times the probability flux must cancel. The F–P equation (2.36) corresponding to the case $J = 0$ is,

$$k_B T \frac{\mathrm{d}}{\mathrm{d}\theta} P_{\text{eq}}(\theta) = \left(\tau_c - V'(\theta)\right) P_{\text{eq}}(\theta), \tag{2.37}$$

which leads to the known equilibrium probability equilibrium distribution proportional to the Boltzmann factor,

$$P_{\text{eq}}(\theta) = \mathcal{N} \mathrm{e}^{-\frac{V(\theta) - \tau_c \theta}{k_B T}}, \tag{2.38}$$

where $\mathcal{N}$ is a constant determined by the probability normalisation,

$$1 = \int_{-\infty}^{\infty} P_{\text{eq}}(\theta) \mathrm{d}\theta = \mathcal{N} \int_{-\infty}^{\infty} \mathrm{e}^{-\frac{V(\theta) - \tau_c \theta}{k_B T}} \mathrm{d}\theta. \tag{2.39}$$

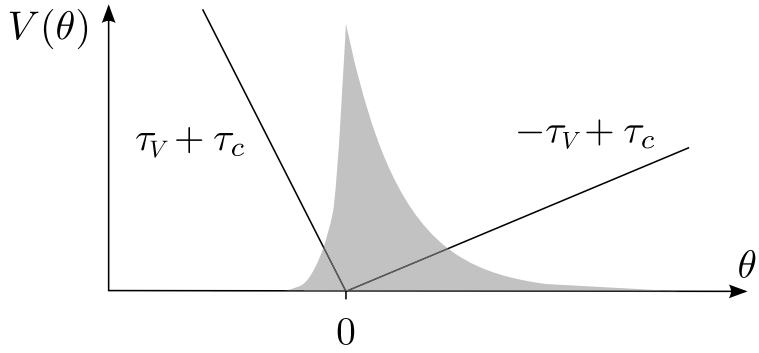

Figure 2.4: Equilibrium distribution (*grey area*) of a Brownian particle inside a piecewise linear minimum and an external conservative torque. The resulting effective potential $V(\theta) - \tau_c\theta$ (*solid line*) is also plotted.

This result is used in several points along the text where the usual potential is a piece–wise symmetric linear well (Fig. 2.4),

$$V(\theta) \equiv \tau_V \left|\theta\right| . \tag{2.40}$$

In this case, the solution of (2.38) is a piece–wise exponential distribution (Fig. 2.4),

$$P_{\rm eq}(\theta) = \begin{cases} \dfrac{1}{k_B T}\left(\dfrac{1}{\tau_c + \tau_V} - \dfrac{1}{\tau_c - \tau_V}\right) \mathrm{e}^{\frac{(\tau_c+\tau_V)\theta}{k_B T}}, & \theta < 0, \\ \dfrac{1}{k_B T}\left(\dfrac{1}{\tau_c + \tau_V} - \dfrac{1}{\tau_c - \tau_V}\right) \mathrm{e}^{\frac{(\tau_c-\tau_V)\theta}{k_B T}}, & \theta > 0. \end{cases} \tag{2.41}$$

2.4.2. White noise limit

The equilibrium probability only describes the statistical properties of the motor during a dwell time. Once the full dynamics of the flashing is introduced, the solution is only available under certain assumptions on the dynamics of the potential. To study this scenario, it is useful to consider the simplest case in which

only two chemical states occur and no external force is taken into account. This is the typical kinetic solution of a motor with a cycle composed by two subprocesses: one chemical and one mechanical. This would be a possible modelling of an ATP hydrolysing motor composed by an ATP waiting time and a mechanical hydrolysis stroke.

The dynamics of such a process can be described by introducing the flashing potential dynamics (2.27) in the general Langevin equation (2.12),

$$\gamma\dot{\theta} = V_R'(\theta) + (V_E'(\theta) - V_R'(\theta))\eta(t) + \xi(t), \tag{2.42}$$

where $V_R(\theta)$ and $V_E(\theta)$ are the two states of the potential and $\eta(t)$, already introduced in (2.27), governs the flashing dynamics and will be considered to be a dichotomous noise with two possible states $\eta(t) = \{\eta_E = 1, \eta_R = 0\}$ and transition rates between them ω_E ($\eta_E \to \eta_R$) and ω_R ($\eta_R \to \eta_E$). The average value of the dichotomous noise can be expressed in terms of these transition rates [22],

$$\langle\eta(t)\rangle = \frac{\omega_R}{\omega_E + \omega_R} \equiv \bar{\eta}. \tag{2.43}$$

The mathematical problem defined by expression (2.42) involves cumbersome analytical calculations. However, in this case, the F–P approach may allow to extract useful information of the system. Nevertheless, F–P receipt (2.34) can not be directly applied because of the dichotomous noise $\eta(t)$. Therefore, in order to find the corresponding F–P equation, expression (2.42) must be rewritten as a white noise Langevin equation.

The first step to do so is to arrange equation (2.42) in terms of a new dichotomous noise $z(t)$ of zero mean,

$$\gamma\dot{\theta} = V_{\text{eff}}' - (V_R' - V_E')z(t) + \xi(t), \tag{2.44}$$

where $V'_{\text{eff}}(\theta)$ is an effective torque defined as,

$$V_{\text{eff}}(\theta) \equiv V_R(\theta) + (V_E(\theta) - V_R(\theta))\ \bar{\eta}. \tag{2.45}$$

The two states of the new noise are,

$$z_E = \frac{\omega_E}{\omega_E + \omega_R}, \qquad z_R = -\frac{\omega_R}{\omega_E + \omega_R}, \tag{2.46}$$

which imply a zero mean value $\langle z(t)\rangle = z_E\omega_E + z_R\omega_R = 0$, and a correlation [22]

$$\langle z(t)\, z(0)\rangle = \frac{\omega_E\omega_R}{(\omega_E + \omega_R)^2} e^{-(\omega_E+\omega_R)t}. \tag{2.47}$$

Finally, the new dichotomous noise can be approximated by a white noise of zero mean and equivalent intensity σ_W given by [27],

$$\sigma_W = \int_0^\infty \langle z(t)z(0)\rangle \mathrm{d}t = \frac{\omega_R\,\omega_E}{(\omega_E + \omega_R)^3}. \tag{2.48}$$

This white noise limit approximation will work as long as the memory exponential term of the correlation (2.47) can be approximated by a delta function. This means that the correlation time $t_{\text{corr}} = (\omega_E + \omega_R)^{-1}$ has to be smaller than or comparable with any other characteristic time of the system. For convenience, this characteristic time can be chosen to be ω_E^{-1} as a typical time of the cycle that will reveal itself to be useful for nucleotide hydrolysis motors in Chapter 3. Nevertheless, other choices for the comparison time may be useful for other systems. With the present criterion, the validity of the approximation can be analysed in terms of a magnitude ϵ comparing both times,

$$\epsilon = \frac{\omega_E + \omega_R}{\omega_E}. \tag{2.49}$$

In general, a threshold value ϵ_0 can be defined such as the white noise approximation can be used for large enough values of ϵ such that $\epsilon \geq \epsilon_0$.

Introducing the noise information (2.48) in (2.44) a new Langevin equation in the Stratonovich interpretation can be written with a multiplicative white noise term including both noise contributions,

$$\gamma\dot{\theta} = -V'_{\text{eff}} + g(\theta)\chi(t), \tag{2.50}$$

being $g(\theta)$ the multiplicative noise function

$$g^2(\theta) = \left(V'_E - V'_R\right)^2 \frac{\omega_R\,\omega_E}{(\omega_E + \omega_R)^3} + \gamma k_B T. \tag{2.51}$$

The function $\chi(t)$ in (2.50) is a white noise with zero mean and autocorrelation $\langle\chi(t)\chi(0)\rangle = 2\delta(t)$. With the current Langevin equation (2.50), an associated F–P equation can be written,

$$\frac{\partial P(\theta,t)}{\partial t} = \frac{\partial}{\partial\theta}\left(\frac{V'_{\text{eff}}}{\gamma} + \frac{g(\theta)}{\gamma^2}\frac{\partial}{\partial\theta}g(\theta)\right)P(\theta,t), \tag{2.52}$$

where the Stratonovich interpretation is chosen since it is the natural interpretation when the white noise comes from an approximation of a coloured noise [27].

The symmetry properties of the potential discussed in previous sections is extended to the effective potential V_{eff} since it is a lineal combination of the different potentials composing the flashing potential. Therefore, the F–P equation solution can be reduced to a finite length θ_0 with periodic boundary conditions. In this case, a constant flux J is reached for which the probability is stationary in time [22], and the equation (2.36) takes the form

$$-J = \frac{V'_{\text{eff}}}{\gamma}P(\theta) + \frac{g}{\gamma^2}\frac{d}{d\theta}\left(gP(\theta)\right). \tag{2.53}$$

Since J states the rate of advance for the probability of finding the motor in a certain position, it can be directly related with the actual average velocity of the motor [64],

$$\omega = \theta_0\, J. \tag{2.54}$$

Defining the function $R(\theta) \equiv \left(\frac{g(\theta)}{\gamma}\right)^2 P(\theta)$, the steady–state F–P equation (2.53) can be written as a first order lineal differential equation,

$$\frac{dR(\theta)}{d\theta} = -\left(\frac{\gamma V'_{eff}}{g^2} - \frac{g'}{g}\right) R - J, \tag{2.55}$$

with the periodic boundary condition $R(0^+) = R(\theta_0^+)$, being $R(0^+)$ the value of $R(\theta)$ at $\theta \to 0^+$. The problem is closed imposing the normalisation condition $\int_0^{\theta_0} P(\theta)d\theta = 1$, obtaining the expression for the flux

$$J = -\left(\int_0^{\theta_0} \gamma^2 \frac{\mathcal{A}(\theta) + \frac{\mathcal{A}(\theta_0^+)}{\mathcal{A}'(\theta_0^+)-1}}{g^2(\theta)\mathcal{A}'(\theta)} d\theta\right)^{-1}, \tag{2.56}$$

where

$$\mathcal{A}(\theta) = \int_0^{\theta} \frac{g(0^+)}{g(y)} e^{\int_0^y \gamma V'_{\text{eff}}(x)/g^2(x)\mathrm{d}x} \mathrm{d}y. \tag{2.57}$$

These two expressions return an analytical result for the velocity through (2.54) that contains the chemical and physical information of the potential and its flashing through the quantitates V'_{eff} and $g(\theta)$. The F–P white noise approximation is further addressed in the description of F_1–ATPase in section 3.2.3.

3

ATP driven motors

Among the several sources of energy that fuel different molecular motors, the greatest part of them are those obtaining energy from the hydrolysis of nucleotide derivatives such as ATP (Adenosine Triphosphate). Such energy is stored in the molecule through high–energy phosphate bonds and released through the hydrolysis reaction resulting in their respective diphosphates. For instance, the ATP hydrolysis reaction, which is the most common energy source in the cell, decomposes the ATP in ADP (Adenosine diphosphate) and Pi (Phosphate),

$$\mathrm{ATP} \rightarrow \mathrm{ADP} + \mathrm{P_i}. \tag{3.1}$$

Molecular motors act as catalysts of this hydrolysis reaction. The reaction starts with the ATP diffusing molecule intake at the ATP affine catalytic site of the motor. There, the substrate binding reaction takes place progressively. This process results from a set of energetically favourable reactions involving different intermediate structural configurations. The final step of the reaction is the cleavage of the molecule and its subsequent release of the reaction products. This gradual mechanism for the nucleotide hydrolysis is called binding–zipper [5, 15, 49]. The binding–zipper explains the mechano–chemical coupling that gives place to the

mechanical processes observed in the motor stepping trajectories. On the other hand, the ATP absorption or the ADP and P_i release gives place to typical dwell processes.

A full fauna of motors work through ATP hydrolysis with different hydrolysis mechanisms and tasks. From linear walking motors such as the conventional kinesin, in charge of delivering cargoes along the cell; to translocases, in charge of the active transport of certain molecules across membranes. This continuous hydrolysis of ATP makes necessary an extra machinery in charge of recharging the cell by synthesising ATP from its hydrolysis products, the F_0F_1–ATP synthase already described in Section 1.3.1. A special feature of F_0F_1–ATP synthase is its modularity allowing to study F_0 and F_1 subunits separately. Specifically, the F_1 portion can act itself as an ATP consuming motor, the F_1–ATPase, that uses the hydrolysis energy to rotate the central γ shaft (Fig. 3.1). Comprehending the working of this motor is essential to understand the working of the whole F_0F_1 complex. Hence, the rest of the chapter is devoted mainly to apply the different aspects developed in Chapter 2 to unravel the transduction mechanisms of F_1 motor.

3.1. F_1–ATPase is a rotatory motor

In order to comprehend the mechanical mechanism of the F_1 motor is essential to understand its morphology. The first solved structure [1] revealed the globular shape of F_1 composed by the circular arrangement of three alternative α and β domains. This structure pointed out the rotatory mechanism of the enzyme. However, The actual rotation of the central γ shaft was not observed until 4 years later, with a rotational assay attaching actin filaments to the γ shaft [47]. The use of smaller loads and the increasing in the precision of experimental techniques allowed to resolve the stepping dynamics of the motor [94]. These

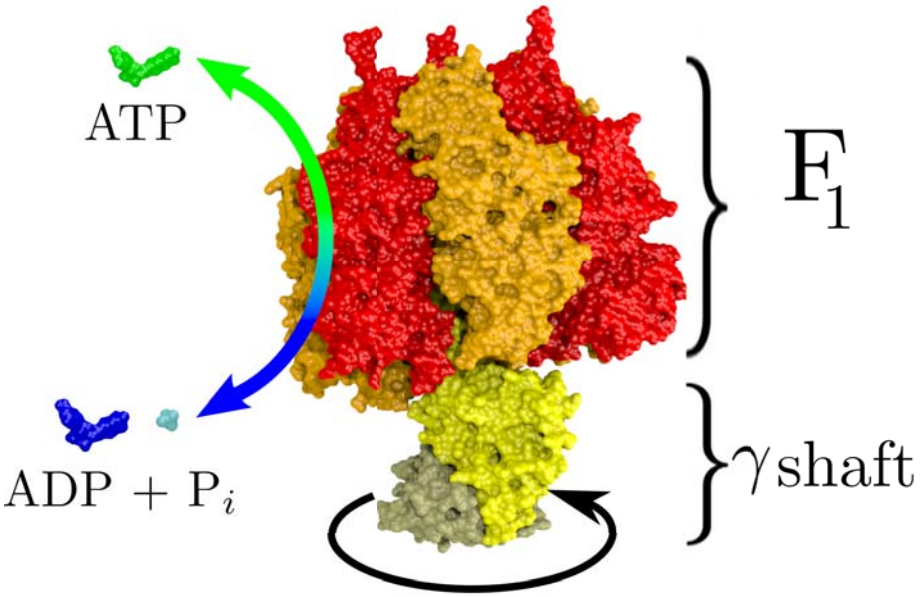

Figure 3.1: F1–ATPase is a molecular motor that generates a rotation of the γ shaft out of the hydrolysis of ATP. The work of the motor can also be reversed to synthesise ATP by exerting an external torque to the γ shaft. Surface plot reconstructed from the PDB structure 1QO1.

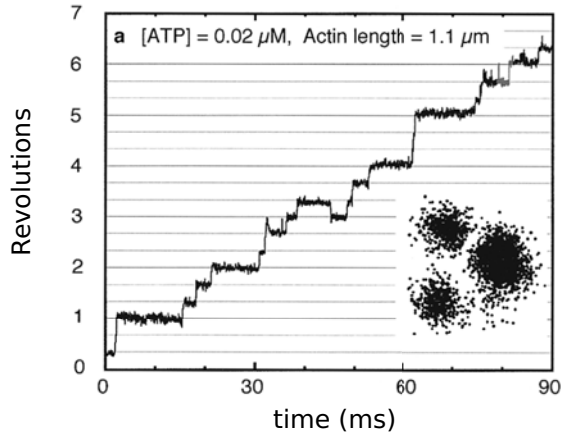

Figure 3.2: Angular trajectory for the F_1–ATPase showing a stepping behaviour of a third of a turn. Inset: Spatial distribution in the cartesian plane of the load, in this case an actin filament [94].

assays revealed that the motor rotation occurred in discrete 120° steps following the structural symmetry of the motor (Fig. 3.2).

Succeeding experimental assays with smaller cargoes not only allowed a more precise observation of the rotation but also the study of the working of the motor under different dissipative drag forces. Actual techniques allow to observe cargoes down to frictions of $\sim 10^{-4}$ pN nm s for gold nano–metric beads [95]. Also the use of different materials for the cargoes provide the possibility to apply a conservative torque on the load with different techniques such as electrorotation [90] or through a magnetic field [50]. The different trajectories resulting from these assays will be the dynamical information available used in this work to decipher the internal mechanism of the F_1–ATPase.

The description developed in this work is valid for a generic F_1 motor. How-

ever, different organisms exhibit differences in the working of the motor [25, 81]. Therefore, in order to obtain a soundness quantitative test on the model is necessary to choose a specific organism of study. Thus, henceforth, all the experimental information corresponds to the thermophilic *Bacillus PS3*. This bacterium is of special interest due to the extensive amount of experiments performed with it. Despite choosing a specific strain, the model can incorporate easily the parameters of other strains following the same methodology described hereon. For this reason, it is necessary to split the parameters into three groups. On one hand the experimental external controllable parameters such as the ATP concentration or the different external torques applied on the motor. This first group will be referred as *Control Parameters*. A second group comprises those parameters that are specific to the *Bacillus PS3* F_1 motor. The values of these parameters do not have significant variations with experimental conditions *e.g.* internal torques generated by the motor. The parameters of this group are referred as *Motor Intrinsic Parameters*. Finally, a third group contains those parameters that depend on the experimental set up. These parameters are, in general, those related to the chemical kinetics of the motor *i.e* reaction rates. This variation with the experimental set up is a signature of a lack of information from the experimental conditions such as the concentrations of ADP, phosphate or other ions changing the ionic strength. Parameters composing this group will be referred hereon as *Experimental Setup Parameters*. In the course of the chapter different parameters will arise, all of them are gathered in Tables 3.1–3.4. Some of them, specially the Experimental Setup Parameters, may change among different experimental works. In these cases, the variations will be addressed specifically.

3.2. F_1–ATPase under dissipative forces

As is stated in Section 2.2, forces of different nature *i.e.* dissipative and conservative, have very different implications in the motion of a molecular motor. While dissipative act passively through the drag force, conservative torques are able to produce a more active action on the protein changing the mechanical and chemical properties of the motor. Therefore, a set up under purely dissipative forces is a good starting point to unravel the underlying mechanism driving the F_1 motor. The procedure employed to study the purely dissipative scenario is the following: First an average velocity is studied to determine the leading mechanisms of the motor dynamics, then a motor potential is presented to explain the stepping dynamics, after that, the stochastic elements of the motor are introduced (thermal fluctuations and chemical kinetics) and studied through computer simulations.

3.2.1. Deterministic Analysis

The stepping behaviour of the F_1 motor follows the biomolecular symmetry of the motor fixing the cycle length $\theta_0 = 2\pi/3$ (Figs. 2.1 and 3.2) implying at least two different leading processes at each cycle, one dwell and one mechanical stroke. The characterisation of these processes through its mean duration is enough to obtain a first guess to the average velocity of the motor through expression (2.16).

Assays with variation of [ATP] reveal a high dependence of the dwell duration with the nucleotide concentration, pointing out that the dwell time is the chemical time necessary for the motor to wait for the motor and start the hydrolysis. This process can be described using the corresponding reaction kinetics scheme (2.6)

resulting in the average reaction time (2.7) that can be written as

$$\langle t_{\text{dwell}} \rangle = t_0 \left(\frac{k_0}{[ATP]} + 1 \right). \tag{3.2}$$

The values of the two parameters describing the dwell time, namely, t_0 and k_0, can be extracted from the intensive exploration of the dwell times using $[ATP]$ as Control Parameter [95] and are gathered in Table 3.1.

On the other hand, the average time for the mechanical stroke can be described through the average overdamped time required to advance the whole motor step θ_0 with a certain energy ΔG_{ATP} (2.18)

$$\langle t_{\text{mech}} \rangle = \theta_0^2 \frac{\gamma_0 + \gamma_L}{\Delta G_{\text{ATP}}}, \tag{3.3}$$

where the total energy is supposed to be released homogeneously along the stroke $\Delta G_{\text{ATP}} = \tau_{\text{in}} \theta_0$. In addition, the effective total friction for the tight coupling (2.13) $\gamma_{\text{eff}} = \gamma_0 + \gamma_L$ is used. It comes in handy to keep both friction coefficients separated in the description of the motor since γ_L is a Control Parameter. The tight coupling approximation is fully addressed later on through stochastic simulations in Section 3.2.2 attesting the validity of the approximation.

The internal friction γ_0 can be estimated from experiments where the velocity of the motor is studied for different load sizes. These experiments show two different behaviours: For low enough values of the friction of the load, γ_L is not rate limiting *i.e.* the velocity is independent of γ_L. This is the situation in which the internal friction of the motor is higher than the friction of the load ($\gamma_0 > \gamma_L$). On the other hand, for large values of the load, there is a dependence of the velocity of the motor with γ_L slowing the motor. This is the situation in which the friction of the load is larger than the internal friction of the motor ($\gamma_0 < \gamma_L$). The intermediate value of γ_L for which the behaviour changes, will correspond with the point at which the friction of the load is comparable with the internal

friction of the motor ($\gamma_0 \simeq \gamma_L$) (Table 3.1).

The energy resulting from the hydrolysis of the ATP molecule may not be fully used in the transduction cycle. As a result, the energy obtained from the hydrolysis reaction ATP is actually an upper boundary to the energy used by the motor. However, since the transduction is expected to be quite efficient, both quantities should be close to each other. For this reason, both energies are referred hereon ΔG_{ATP} for the sake of simplicity if not stated otherwise. In the current work, typical values of the hydrolysis energy in the cytoplasm is used [2] (Table 3.1).

The description of the total average cycle time of the motor $\langle \mathcal{T} \rangle = \langle t_{\mathrm{dwell}} \rangle + \langle t_{\mathrm{mech}} \rangle$ implies a deterministic average velocity

$$\omega = \frac{\theta_0}{\langle \mathcal{T} \rangle} = \frac{\theta_0}{t_0 \left(\frac{k_0}{[\mathrm{ATP}]} + 1 \right) + \theta_0^2 \frac{\gamma_0 + \gamma_L}{\Delta G_{\mathrm{ATP}}}}, \tag{3.4}$$

which returns a prediction for the average velocity of the motor under the variation of the two main Control Parameters: ATP concentration and the friction of the load γ_L. The resulting velocity can be contrasted with experimental results obtaining a very good match between experimental information and the main velocity prediction (Fig. 3.3). In order to extend the validity of the model, the experimental information used for the parameter extraction is different from the one used for the average velocity testing, *i.e.* there is no parameter fitting in the velocity prediction of Fig. 3.3.

So far, the analysis carried out only takes into account the average velocity of the motor without considering the specific dynamics composing each step (Section 2.3). This information can be obtained from submillisecond precision trajectories involving a better analysis of chemical processes [81]. Additionally,

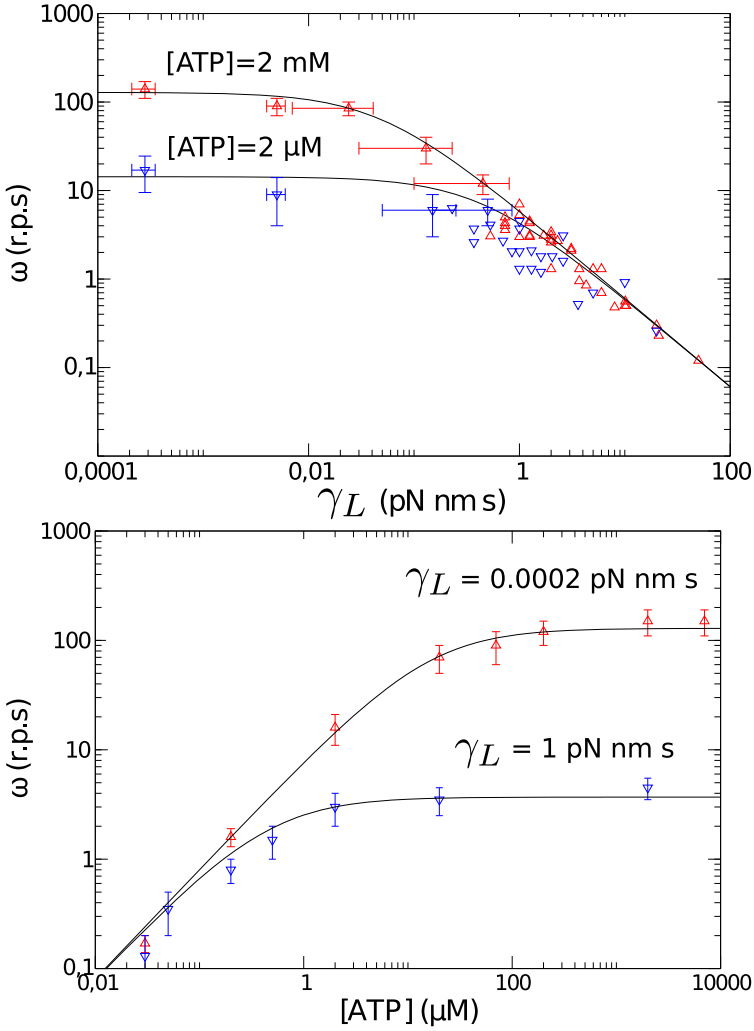

Figure 3.3: Analytical prediction (*solid line*) for the average angular velocity (3.4) compared with experimental data (*triangles*) [95] Top: Velocity *vs.* load friction. Bottom: Velocity *vs.* [ATP]. Parameters used are those of Table 3.1.

	Parameter	Value
Motor Intrinsic Parameters	γ_0	5 pN nm ms
	ΔG_{ATP}	90 pN nm
Experimental Setup Parameters	k_M	18 μM
	t_0	2.3 ms

Table 3.1: Parameters used in the description of F_1 motor for *Bacilus PS3*.

a submillisecond analysis shows that the cycle is not divided in a single step but in two substeps of different length and duration. The first substep is the largest spanning $\sim 80°$–$90°$ while the second one is shorter and spans the remaining $\sim 30°$–$40°$ (Fig. 3.4). The nature of each substep was revealed with experiments where the hydrolysis of ATP and product release is decelerated. This involves experiments with mutants [26, 75, 90]; assays with ATPγS, a slow hydrolisable ATP analog [75] or ATP–Mg analysis [26]. These experiments show that the two substeps are the result of the different stages of the ATP hydrolysis. In first place, the empty motor waits a dwell time t_s for an ATP to arrive at the catalytic site. Then, the hydrolysis reaction starts producing the first mechanical substep of $\theta_1 \sim 85°$. After that, the system waits for a catalytic time t_c for the reaction products (ADP and P_i) to leave the motor. Finally, the $\theta_2 \sim 35°$ substep occurs through the release of the elastic energy stored by the structural deformation of the catalytic site once the hydrolysis products leave the motor. Once the second stroke ends, the motor returns to the starting configuration closing thus the mechano–chemical cycle (Fig. 3.4 Bottom). In order to describe the angular advance of the steps, it comes in handy to describe each substep as a fraction of the total angular length of the cycle as,

$$\theta_1 = \alpha\theta_0, \qquad \theta_2 = (1-\alpha)\theta_0. \tag{3.5}$$

Allocating two different mechanical strokes of a torque τ_1 and τ_2 each one consuming a energy $E_{1,2}$ as

$$\tau_1 = \frac{E_1}{\theta_1} = \frac{E_1}{\alpha\theta_0}, \qquad \tau_2 = \frac{E_2}{\theta_2} = \frac{\Delta G_{\mathrm{ATP}} - E_1}{(1-\alpha)\theta_0}. \tag{3.6}$$

Where the energy conservation is used so the hydrolysis energy is distributed among the two substeps

$$\Delta G_{\mathrm{ATP}} = E_1 + E_2. \tag{3.7}$$

Motive torques τ_1 and τ_2 give some information of the motor potential (2.20). However, they do not describe the whole motor potential since there is still a lack of information on the structure of the potential during the dwells.

In the search for a suitable motor potential, is mandatory to find the essential different conformational states composing the transduction cycle (Sec. 2.3). In the present case there are two well differentiated states. On the one hand, the state in which the active catalytic site of the motor is empty. This state will be called hereon *relaxed state*. On the other hand, the state in which the active catalytic site is occupied either by an ATP molecule or by its hydrolysis products. This state will be referred hereon as *excited state*. The simplest way to describe both states comes through linear piecewise potentials following the angular symmetry of the motor together with the rest of mechano–chemical constrains (3.5) and (3.6). From the flashing between both states the substep dynamics will emerge naturally. The concrete description of each potential is constructed as follows.

During the ATP dwell times when the catalytic site is waiting for an ATP, the active potential is the relaxed one $V_R(\theta, n)$. Therefore, this potential must have three minima following the three–fold symmetry of the motor coinciding with the three angular dwell positions (Fig. 3.5 A.1). For the n-th step, the potential

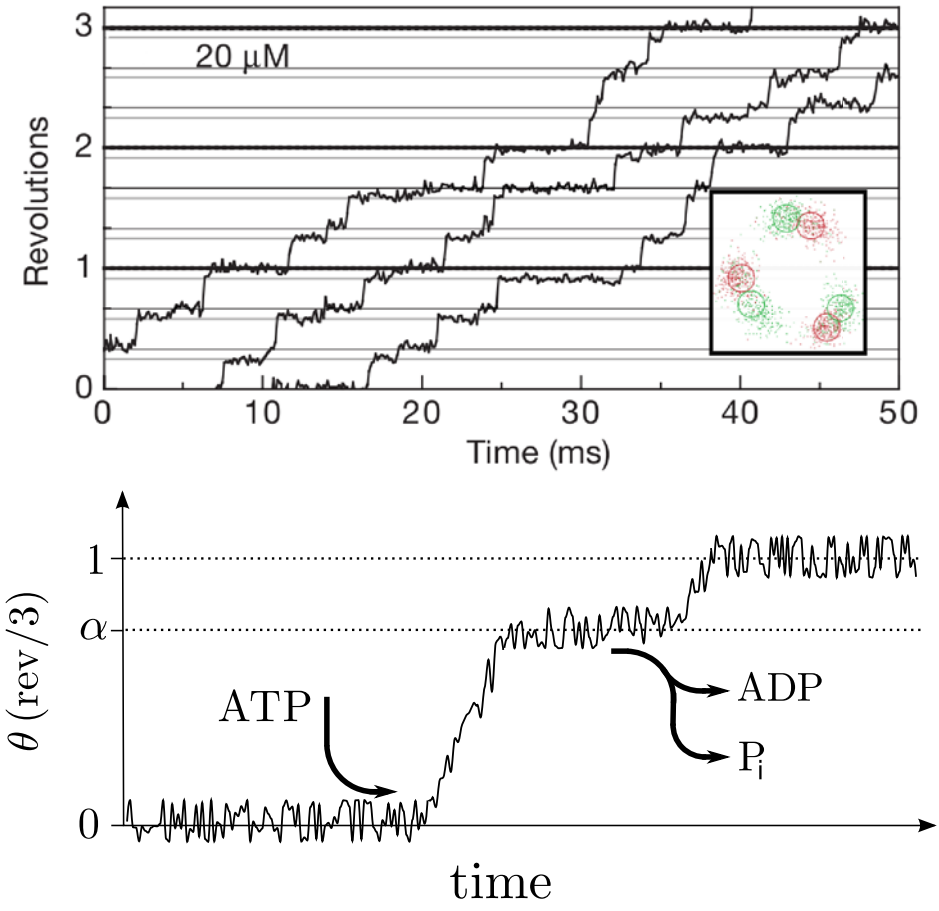

Figure 3.4: Top: Experimental trajectory of the F_1–ATPase showing the substep dynamics. Different lines correspond to the same trajectory but are compacted for the sake of visualisation. Inset: Spatial density in the cartesian plane of the load residence time revealing the substeps [95]. Bottom: Scheme of a full step of a trajectory pointing out the chemical occupation at each stage.

reads

$$V_R(\theta,n)=\begin{cases} -V_0\left(\dfrac{3\theta}{\pi}-2n\right), & \dfrac{2\pi}{3}\left(n-\dfrac{1}{2}\right)\leq\theta\leq\dfrac{2\pi}{3}n, \\ \\ V_0\left(\dfrac{3\theta}{\pi}-2n\right), & \dfrac{2\pi}{3}n\leq\theta\leq\dfrac{2\pi}{3}\left(n+\dfrac{1}{2}\right). \end{cases} \tag{3.8}$$

Being V_0 the energetic height of the potential. On the other hand, the excited potential in charge of driving the shaft during the hydrolysis will be a local potential with its minimum shifted an angular distance $\alpha\theta_0$ from the relaxed potential minimum (Fig. 3.5 A.2). The analytical form of the excited potential for the $n-$th step is

$$V_E(\theta,n)=\begin{cases} \dfrac{-V_1}{\alpha+1/2}\left(\dfrac{3\theta}{2\pi}-\alpha-n\right), & \theta\leq\dfrac{2\pi}{3}(n+\alpha), \\ \dfrac{V_1}{\alpha+1/2}\left(\dfrac{3\theta}{2\pi}-\alpha-n\right), & \theta\geq\dfrac{2\pi}{3}(n+\alpha), \end{cases} \tag{3.9}$$

where V_1 is the height of the excited potential and is directly related with the torque of the first substep.

The flashing mechanism along the n-th cycle works as follows. Initially, the motor is found in the ATP waiting dwell confined by the potential $V_R(\theta,n)$ (Fig. 3.5 A.1). When an ATP molecule arrives at the empty catalytic site, the allocation of the ATP molecule changes the energetic configuration of the motor to the excited state $V_E(\theta,n)$ starting the n-th step. The stroke generated by the excited potential τ_1 is in charge of the first substep (Fig. 3.5 A.2). Once the shaft arrives at the minimum of the excited state $V_E(\theta_n)$, the potential does not change until the hydrolysis products ADP and P_i are released to the medium, giving place to the catalytic dwell. Once the products are released, the energetic landscape returns to its original relaxed state $V_R(\theta,n+1)$. However, since the shaft is not located in the minimum of the relaxed state, there is a net torque τ_2 which produces the second substep (Fig. 3.5 A.3). Once the shaft reaches

the minimum of the potential, the transduction cycle is closed and the n-th step finishes.

Even though the whole potential landscape cannot be obtained from the available experimental measures, they provide enough information to have the evidence of the flashing mechanism and the value of the torques that involve each potential. They also provide information about the height of the potentials, which are unknown parameters related directly with the substep torques through the slope of the potentials (3.8) and (3.9),

$$V_0 = \tau_2 \frac{\theta_0}{2}, \qquad V_1 = \tau_1 \theta_0 (\alpha + 1/2), \tag{3.10}$$

which are expected to be comparable ($V_0 \sim V_1$). For the sake of simplicity the analysis will continue with the assumption $V_0 = V_1$. Later on the text, the more general case $V_0 \neq V_1$ will be addressed showing analog results. In this scenario, the energies consumed in each substep can be expressed in terms of the potential height V_0 introducing (3.10) in (3.6).

$$E_1 = V_0 \frac{2\alpha}{1+2\alpha}, \qquad E_2 = 2V_0(1-\alpha). \tag{3.11}$$

Inserting these equations in the identity (3.7) , the relation $V_0(\Delta G_{ATP})$ becomes available

$$V_0 = \frac{\Delta G_{ATP}}{2 - \frac{4\alpha^2}{1+2\alpha}}. \tag{3.12}$$

The fact that all the energetic parameters can be described in terms of the energy consumed from the hydrolysis of ATP leaves α as the only unknown parameter. Parameter α determines the length of the substep. The case $\alpha = 1$ would return a one–step average model equivalent to the initial average guess (3.4), while experimental observations show that the substep length spans 80^0–90^0. However, instead of fixing this angular distance it is interesting to leave it as a free

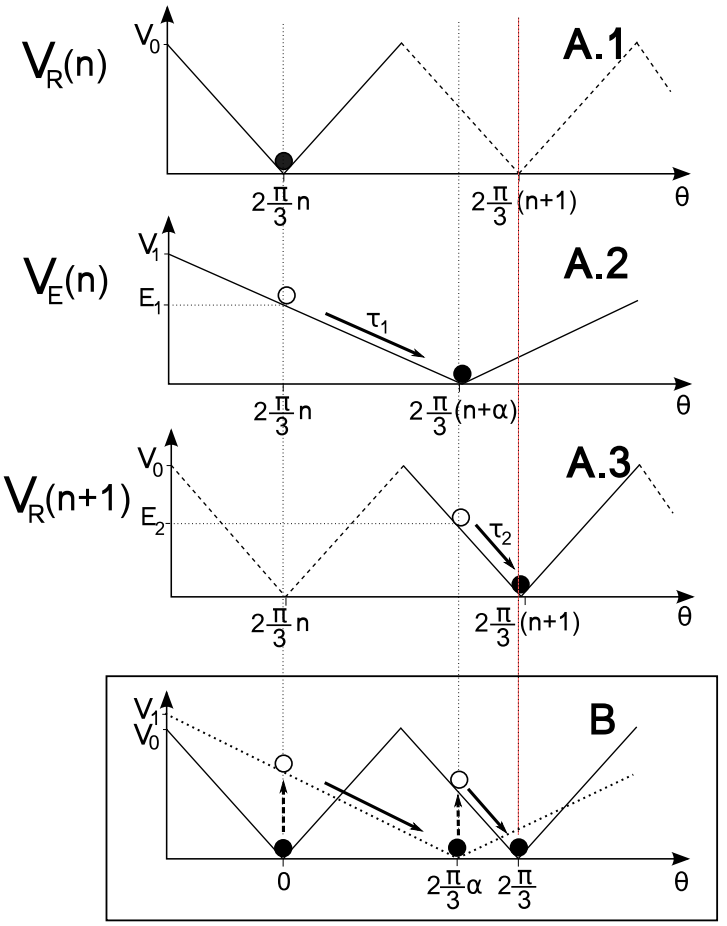

Figure 3.5: Flashing mechanism describing the dynamics of the $n-$th step. The different phases composing the step A.1-3 are summed up in the final scheme B. The flashing of the potential (*dashed arrows*) induce the mechanical strokes (*solid arrows*) in charge of the motion o the shaft (*circle*).

parameter and study how the working of the motor changes with it. From a evolutionary point of view, it is expected that the motor has evolved to operate in an optimum regime. For instance, a motor such as the kinesin may have evolved to travel through the actin tracks as fast as possible. However, F_0F_1–ATP synthase, which is an energy transducer, is expected to transduce the energy available in the most effective manner. In this case the opposite to the kinesin is true, a slow transduction time (mechanical time) not only allows for other different internal catalytic processes to take place but also returns a more reliable energy transduction. For the flashing mechanism, the total mechanical time is,

$$t_{\rm mech} = t_{\rm mech\,1} + t_{\rm mech\,2} = (\gamma_0 + \gamma_L)\left(\frac{\theta_1}{\tau_1} + \frac{\theta_2}{\tau_2}\right) \tag{3.13}$$

$$= \left(\frac{2\pi}{3}\right)^2 \frac{\gamma_0 + \gamma_L}{\Delta G_{ATP}} \left(2 - \frac{4\alpha^2}{1+2\alpha}\right)\left(\alpha^2 + \frac{1}{2}\right). \tag{3.14}$$

which can be optimized as a function of α,

$$\left.\frac{{\rm d}t_{\rm mech}}{{\rm d}\alpha}\right|_{\alpha_M} = 0 \quad \Rightarrow \quad 1 - 2\alpha_M^2 = 0. \tag{3.15}$$

Giving an universal value of α that maximises the mechanical time (see Fig. 3.6) and is independent of any other parameter of the system

$$\alpha_M = 1/\sqrt{2}. \tag{3.16}$$

The resulting value coincides with the experimentally observed substep angles $\theta_1 = 2\pi\alpha/3 = 85^{\rm o}$ and $\theta_2 = 35^{\rm o}$. This result not only enhances the validity of the model but also points out that the angle obtained does not depend on any magnitude or any fitting but is an universal value resulting from the optimisation of the flashing mechanism in which two different strokes corresponding to two different occupation states are considered *i.e.* the substep angle does not depend in any parameter of the model. For this optimum value for α, the torque observed values are $\tau_1 = 27$pN nm and $\tau_2 = 65$pN nm.

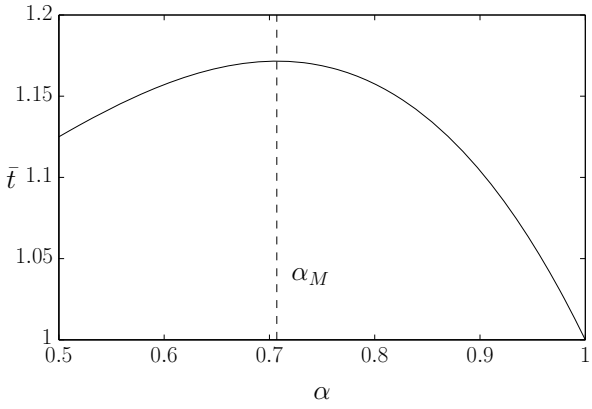

Figure 3.6: Mechanical time versus the substep angle parameter α. There is a maximum of the mechanical time for a value $\alpha_M = 1/\sqrt{2}$. A dimensionless value of the mechanical value is used $\bar{t} = \left(\frac{3}{2\pi}\right)^2 \frac{\Delta G_{\rm ATP}}{\gamma_0+\gamma_L} t_{\rm mech}$.

The experimental values of each torque separately are difficult to measure experimentally due to the speed and fluctuations of each trajectory. The difficulty lies in the determination from the trajectory of the beginning of each substep. Measures from the average torque for a whole step report torques around 40 pN, which is in agreement with the average angular torque predicted for α_M,

$$\langle \tau \rangle = \frac{\tau_1\theta_1 + \tau_1\theta_2}{\Delta\theta_0} = \tau_1\alpha + \tau_2(1-\alpha) \simeq 38 \text{ pN nm}. \tag{3.17}$$

So far, the condition $V_0 = V_1$ has been used along eqs. (3.11–3.17). However, this condition can be loosened introducing the dimensionless parameter $\varepsilon \equiv \dfrac{V_0}{V_1}$. Actually, the hydrolysis energy can be changed experimentally [44]. If this change in $\Delta G_{\rm ATP}$ has a mechanical effect it would be reflected in the model as a variation of the height of the excited potential V_1.

A variation of ε will also change the torques and the substep angles changing

the energetic relations (3.11) obtaining a new energy balance

$$\Delta G_{\mathrm{ATP}} = E_1 + E_2 = \frac{2\alpha}{1+2\alpha} V_1 + 2(1-\alpha)V_0 \tag{3.18}$$

$$= \left(\frac{2\alpha\varepsilon}{1+2\alpha} + 2(1-\alpha) \right) V_0, \tag{3.19}$$

which can be rewritten to obtain a relation for ε,

$$\varepsilon(\alpha, \Delta G_{\mathrm{ATP}}/V_0) = \left(1 + \frac{1}{2\alpha}\right) \left(\frac{\Delta G_{\mathrm{ATP}}}{V_0} - 2(1-\alpha) \right). \tag{3.20}$$

Proceeding as previously (3.14), the energetic relation (3.19) sets a new mechanical time

$$t_{\mathrm{mech}} = \left(\frac{2\pi}{3}\right)^2 \frac{(\gamma + \gamma_L}{\Delta G_{\mathrm{ATP}}} \left(\frac{\alpha\varepsilon}{1+2\alpha} + 1 - \alpha \right) \left(\frac{\alpha(1+2\alpha)}{\varepsilon} + 1 - \alpha \right) \tag{3.21}$$

which returns a maximum time for a new optimum value $\alpha = \alpha_M$ that follows the relation

$$\varepsilon = -5 + 6\alpha_M + \frac{-6 + 12\alpha_M}{-1 + 2\alpha_M(1+\alpha_M)}. \tag{3.22}$$

From conditions (3.20) and (3.22) results the maximum value α_M that corresponds to a certain ratio $\Delta G_{\mathrm{ATP}}/V_0$ (Fig. 3.7). This analysis predicts that for biological parameters, the variation produced for different hydrolysis energies is minimum compared with the obtained for $\varepsilon = 1$. Therefore, in general, the values and expressions (3.11–3.16) are good approximations for the real motor. In general, the concrete values used for the model will change for motors of different strains which will present different energetic parameters. Thus, this analysis guarantee a comparable quantitative analysis between them.

Experiments performed on and ADP–inhibited conformation of F_1 where the release of products to the media is slowed [26], allows to observe the behaviour of

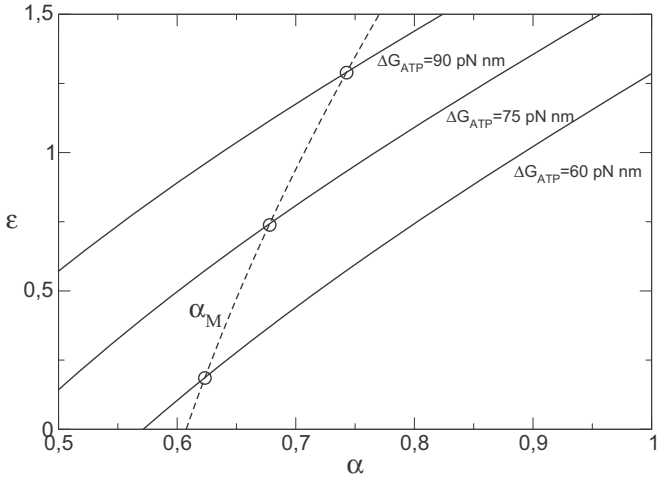

Figure 3.7: The corresponding value of α_M can be found as the intersection between the α_M relation (Eq. 3.22) (*dashed line*) and the energy conservation relation (Eq. 3.20) (*solid lines*). $V_0 = 70$ pN nm.

the shaft during the substep dwell. Therefore, this information permits to explore the energetic landscape corresponding to the minimum of the excited potential. These measures confirm that the excited potential can be treated as a lineal piece–wise potential for a large part of its path in harmony with the potential description (Fig. 3.8). From a linear fitting to the potential, the experimental torque can be calculated obtaining a consistent value of $\tau_1 = 35$ pN nm, which corresponds to a value of $\varepsilon = 1.25$, a little larger than the unity, and a value of $\alpha = 0.74$ corresponding to an angle of 88°. These values return a better approximation to the experimental average torque $\langle\tau\rangle = 40.5$ pN nm. Therefore, despite the approximation $\varepsilon = 1$ is good, the value of $\tau_1 = 35$ pN nm will be used for the rest of the work.

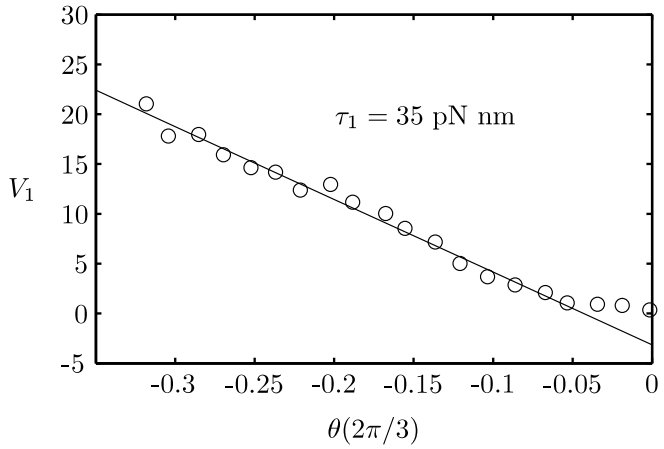

Figure 3.8: Experimental measures of the energetic landscape of the excited potential [26]. The torque associated associated is obtained by fitting a linear regression on the linear part of the potential.

3.2.2. Stochastic analysis

The potential described so far, only takes into account the spatial dependence of the potential. However, for a full description of the dynamics, the temporal description of the potential, laying emphasis in its stochastic nature, is necessary as well. In the current case, the temporal description of the four different processes composing the cycle must be studied: The first stroke ($t_{\mathrm{mech}\,1}$) and the catalytic dwell (t_s), corresponding to the excited potential; and the second stroke ($t_{\mathrm{mech}\,2}$) and the ATP dwell corresponding to the relaxed potential (t_0). In contrast to the deterministic average case, now, a full probabilistic description of each process is analysed.

The ATP dwell time t_s is the kinetic time to absorb an ATP and start the stroke. Experimentally, it has been identified as a two–step rate–limiting reaction

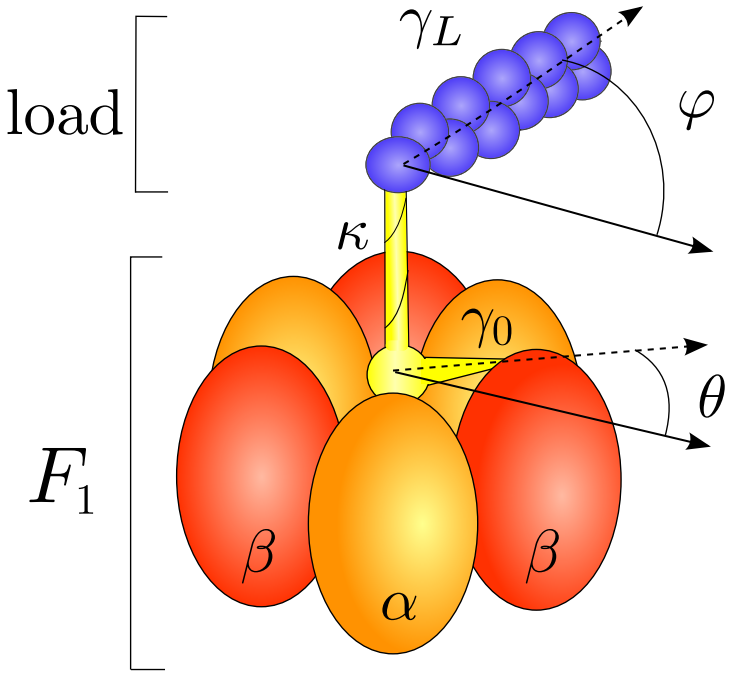

Figure 3.9: Scheme showing the shaft-load system where there are two different free coordinates θ and φ describing the position of the shaft and the load respectively. Both entities are joined by a harmonic torsional spring of stiffness κ

that can be well approximated by a single–step first–order reaction [75] (2.4),

$$P(t_s) = \frac{\exp^{-t_s k_{ATP}[ATP]}}{k_{\mathrm{ATP}}[ATP]}, \tag{3.23}$$

entailing an average reaction time $\langle t_s \rangle = k_{\mathrm{ATP}}[\mathrm{ATP}]$, coinciding with the [ATP] addend part of the dwell time used in the initial average description (3.2), thus, having the relation $k_{ATP} = (t_0 k_0)^{-1}$. On the other hand, the catalytic products release time can be related to the lapse of the dwell time without dependence on [ATP] *i.e.* t_0. In contrast to t_s, the catalytic time t_0 and the mechanical times have not been seen to have a relevant variation over different cycles compared with their average value and therefore will be considered constant for the rest of the study. The low variation coefficient for the mechanical times can be attributed to the high number of chemical reactions taking place during the stroke making up the binding zipper [5, 40]. This choice for the temporal distribution specifies that once the motor flashes to the excited state, it remains in it a deterministic time $t_E = t_{\mathrm{mech1}} + t_0$, then it flashes back to the relaxed state for a stochastic lapse $t_R = t_{\mathrm{mech2}} + t_s$ closing the motor cycle and closing the definition of $V(\theta, t)$ (Fig. 3.10 Bottom).

Additionally, a more realistic generic scenario than the one studied in previous sections, can be studied in which the bulge joining the load and the shaft is not completely rigid as described in expression (2.13)[19, 51, 76]. This situation can be described with two coupled Langevin equations (2.12), one describing the angular coordinate of the shaft (θ), and one for the angular position of the load (φ), which is the experimental observable. Therefore, the different dynamical output magnitudes such as the average velocity of the motor ω will be measured in terms of the measurable variable φ. In the same way, the different external forces applied on the motor will be applied directly in the load. On the other

hand, the internal torque of the motor is directly applied to the spatial coordinate of the shaft θ,

$$\begin{aligned} \gamma_0\dot{\theta} &= -V'(\theta,t) + \kappa(\varphi-\theta) + \xi_0(t), \\ \gamma_L\dot{\varphi} &= -\kappa(\varphi-\theta) + \xi_L(t), \end{aligned} \tag{3.24}$$

where the term $\kappa(\varphi-\theta)$ is the binding force between the load and the shaft described through an harmonic potential of stiffness κ,

$$V_K(\varphi,\theta) = \frac{1}{2}\kappa(\varphi-\theta)^2. \tag{3.25}$$

The thermal force acting on each coordinate $\xi_0(t)$ and $\xi_L(t)$ depends on the specific friction coefficient of each entity obtaining two uncorrelated white Gaussian noises following the fluctuation–dissipation relation (2.10),

$$\begin{aligned} \langle\xi_0(t)\xi_0(t')\rangle &= 2\gamma_0 k_B T\delta(t-t'), \\ \langle\xi_L(t)\xi_L(t')\rangle &= 2\gamma_L k_B T\delta(t-t'). \end{aligned} \tag{3.26}$$

A high enough value of the stiffness drives the motion to the adiabatic case in which the velocities of both coordinates is the same (2.13), thus adding both equations in (3.24), the problem would be reduced to the single Langevin equation (2.14)

$$(\gamma_0+\gamma_L)\dot{\theta} = -V'(\theta,t) + \xi(t), \tag{3.27}$$

where the effective noise $\xi(t) = \xi_0(t) + \xi_L(t)$ is the addition of two Gaussian noises and therefore is a Gaussian noise itself with zero mean and a correlation,

$$\langle\xi(t)\xi(t')\rangle = 2(\gamma_0+\gamma_L)k_B T\delta(t-t'). \tag{3.28}$$

Which is the white noise corresponding to the effective friction $\gamma_{\text{eff}} = \gamma_0 + \gamma_L$.

	Parameter	Value
Stiffness of the shaft	κ	750 pN nm
Excited state torque	τ_1	35 pN nm

Table 3.2: Motor Intrinsic Parameters used in the stochastic simulations for the F_1 motor for *Bacilus PS3* extracted from [26] and [76].

In contrast, a low enough value of κ could hinder the motion of the load or conceal the stepping trajectories from the experimental observations. For the current study, biological values of the stiffness are used [76] (Table 3.2).

Langevin equations (3.24) can be solved numerically using parameters gathered in Tables 3.1 and 3.2 obtaining trajectories for different values of the Control Parameters (Fig. 3.10). Again, there are no fittable parameters, since all the parameters have been extracted from experimental information. The resulting trajectories exhibit the same performance reported experimentally displaying the substepping behaviour, the stochastic dwell times, and angular fluctuations. From the trajectories, average values of the velocity can be compared with experimental average velocities obtaining a very good fit (Fig. 3.11).

Actually, a detailed comparison of the stochastic and the average deterministic prediction (3.4) reveals some discrepancies. Simulations drop out a lower value of the average velocity than the deterministic description. These smaller values of the velocity turn to be a better prediction to experimental data. This effect becomes clearer for high values of the friction of the load (Fig. 3.12). A parameter exploration reveals that the performance of the motor is not affected by the flexibility of the shaft for biological values of κ (Fig. 3.13) observing that in this working regime, the model coincides with the simulations resulting from the adiabatic approximation (3.27). Therefore, the reduction in the velocity is not

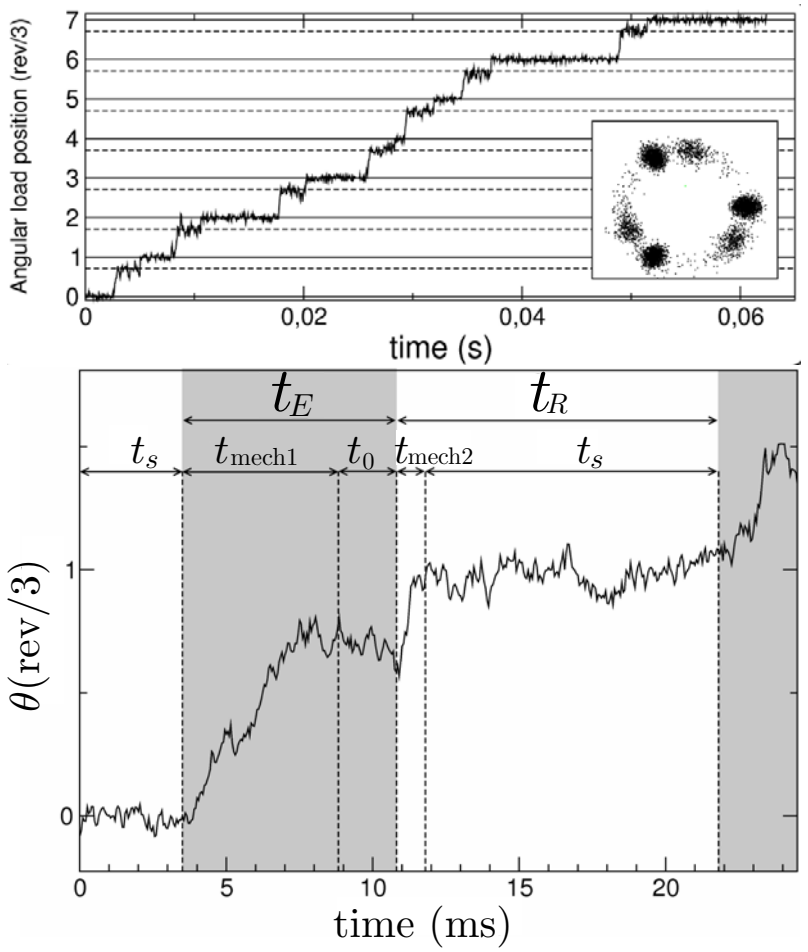

Figure 3.10: Results of the dynamics simulation of the Langevin equations (3.24) using parameters of Tables 3.1 and 3.2. Top: Computational trajectory of the load marking the substepping angles (*dashed lines*). Inset: Spatial occupation density of the load in the cartesian plane. Bottom: Fragment of a trajectory along one full cycle pointing out the different temporal lapses. The excited state (*shadowed zones*) takes a time $t_E = t_{\mathrm{mech1}} + t_0$ whilst the relaxed state (*non–shadowed zones*) takes a stochastic time $t_R = t_{\mathrm{mech2}} + t_s$.

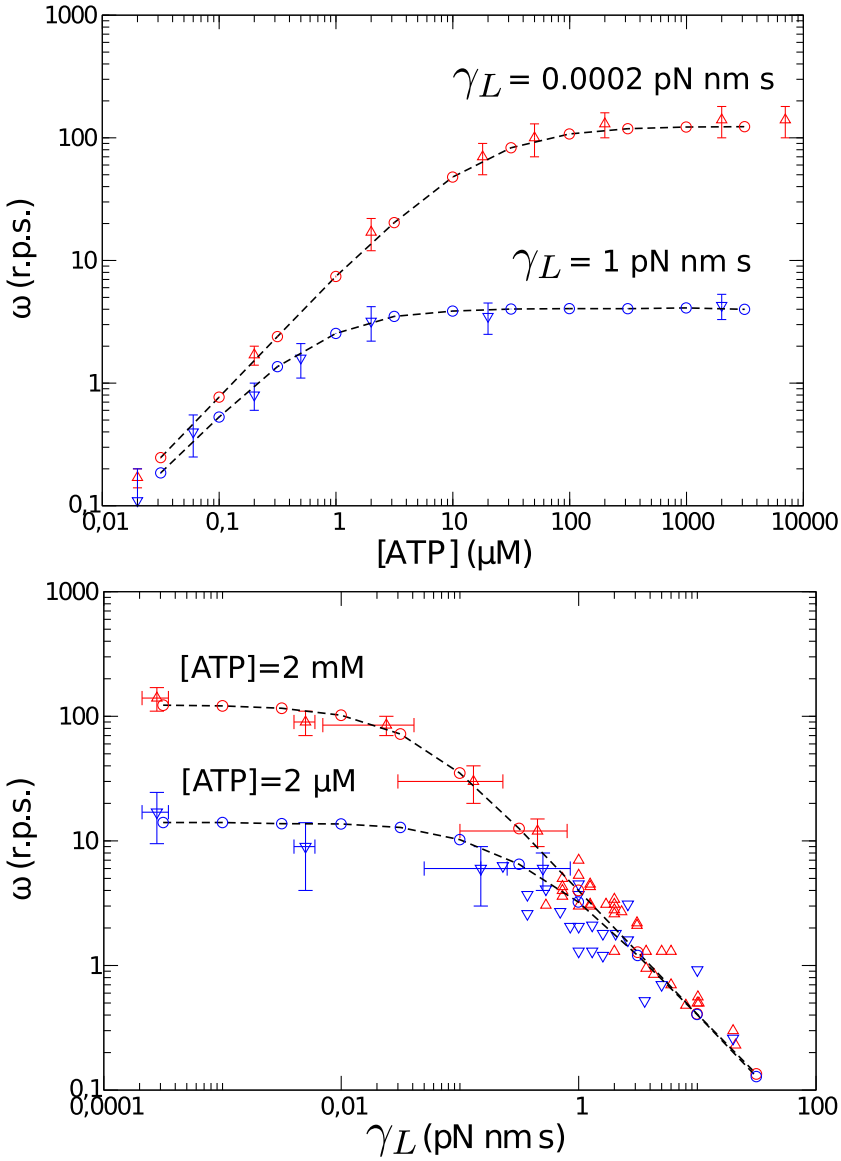

Figure 3.11: Average velocity resulting from stochastic simulations (*circles joined by dashed lines*) compared with experimental data (*triangles*) [95]. Top: velocity *vs.* ATP concentration. Bottom: velocity *vs.* friction of the load.

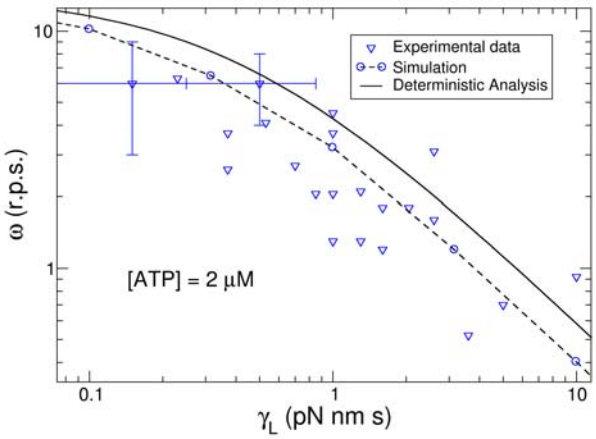

Figure 3.12: Magnified views of Figs. 3.3 and 3.11 showing the discrepancies between the stochastic and the deterministic average predictions.

caused by the elastic load–shaft coupling.

A careful analysis on the resulting stochastic trajectories reveals the existence of missing steps, this is, complete motor cycles that do not produce a successful step (Fig. 3.14) *i.e.* after the full flashing cycle, the dwell position of the shaft corresponds to the initial dwell position. Missing steps occur on account of the stochastic nature of the trajectory that competes with the dynamics imposed by the potential. This effect is difficult to measure experimentally since the occupation of the motor is unavailable and therefore it is complicate to discern between a missing step from a mere fluctuation. Even though missing steps are not producing a successful advance, the ATP hydrolysis necessary to complete the cycle takes place and the energy is wasted (Fig. 3.14). This can be measured in the simulations by measuring the amount of energy consumed by the motor directly available from the evolution of the motor potential (2.30).

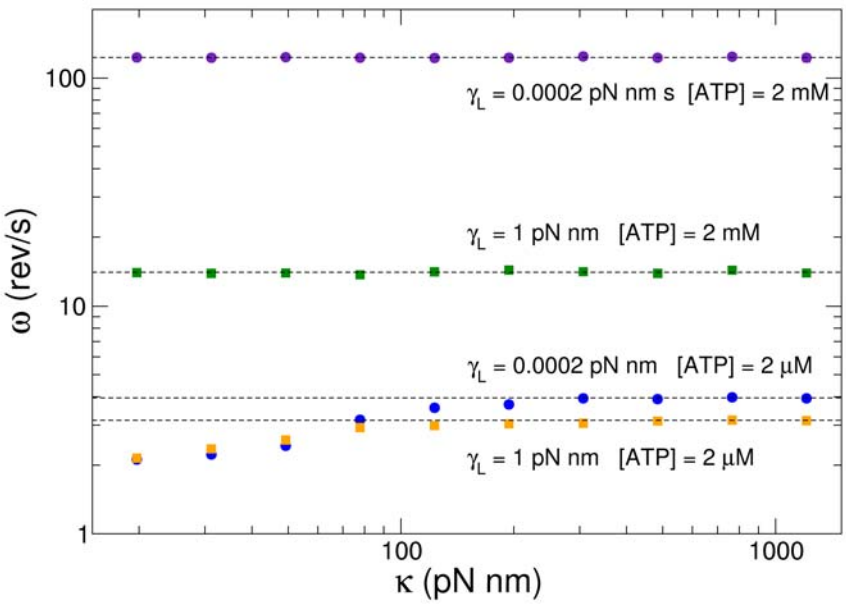

Figure 3.13: Comparison of the resulting average velocity of the stochastic model with the stiffness of the joint κ. Dashed lines are the computational resulting velocities for the adiabatic model. Biological stiffness $\kappa \sim 750$ pN nm falls in a region where the velocity coincides with the adiabatic prediction.

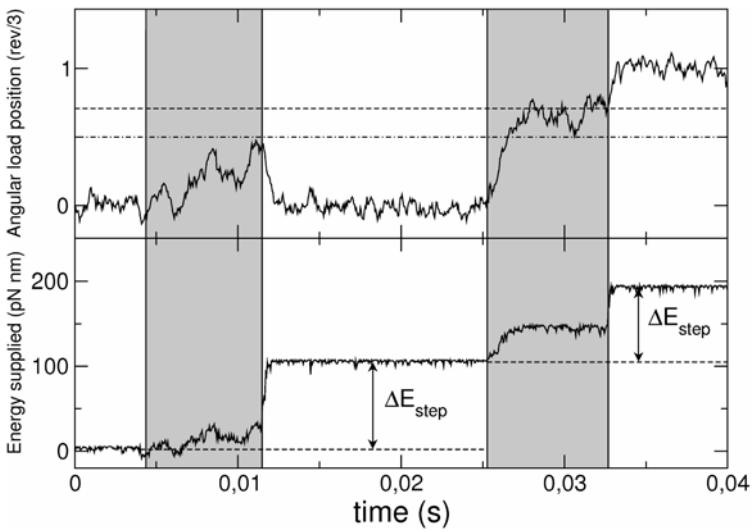

Figure 3.14: Evolution of the motor along two cycles. The first cycle does not produce a successful step while the second one is sucessful. Relaxed (*non–shadowed zones*) and excited (*shadowed zones*) states of the motor are also indicated. Top: Spatial trajectory of the load. After the first cycle, the motor falls back to the initial dwell position. On the contrary, the second one produces a successful step. The substep angle (*dashed line*) and the maximum of the relaxed potential (*dot–dashed line*) are shown. Bottom: Energy consumed by the motor, both cycles consume energy independently of their success.

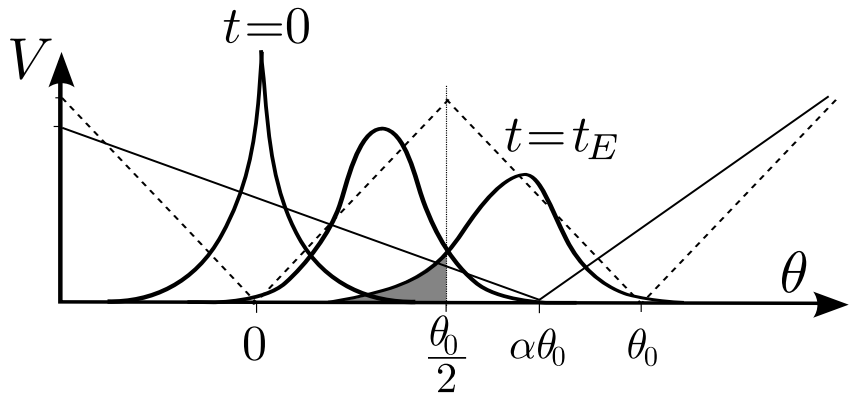

Figure 3.15: Scheme for the evolution of the probability distribution function of the load along the first substep (*thick curves*). When the potential flashes back from the excited potential (*solid straight lines*) to the relaxed state (*dashed lines*). There is a portion of the probability density that does not surpass the maximum of the relaxed state and falls back to the original state (*shaded area*).

Missing steps occurs mainly before the second substep. Just when the potential flashes to the relaxed state the stochastic position of the shaft in the potential determines the success of the cycle. If the shaft has not surpassed the maximum of the relaxed potential, the shaft will be driven back again to the initial dwell position by the relaxed potential (Fig. 3.14). This phenomenon can be studied through the probability distribution of the shaft during the excited state $P_E(\theta, t)$ (Fig. 3.15) by means of the Fokker–Planck equation (2.34), which for the case being reads,

$$\frac{\partial P_E(\theta,t)}{\partial t} = \frac{1}{\gamma_0+\gamma_L}\frac{\partial}{\partial\theta}\left(V_E'(\theta) + k_BT\frac{\partial}{\partial\theta}\right)P_E(\theta,t). \tag{3.29}$$

The spatiotemporal probability solution of this equation is complex due to the non–linearity of the potential. Since the interest in the problem is at the left tail of the distribution, the problem can be simplified by replacing the excited

potential in a first approximation by a linear potential *i.e.* the problem can be tackled by considering an initial probability distribution at a time t=0 that advances under a constant torque τ_1 during a time t_E. The initial distribution at the beginning of the cycle is the equilibrium probability distribution in the relaxed potential minimum prior to the excitation which for a linear well is composed by two exponentials (2.41),

$$P_R(\theta) = \begin{cases} \frac{1}{2}\frac{\tau_2}{k_B T} \mathrm{e}^{\frac{\tau_2}{k_B T}\theta} & , \theta < 0, \\ \frac{1}{2}\frac{\tau_2}{k_B T} \mathrm{e}^{-\frac{\tau_2}{k_B T}\theta} & , \theta > 0. \end{cases} \tag{3.30}$$

For the sake of simplicity, this distribution can be approximated by a Gaussian distribution of the same mean $\langle\theta\rangle = 0$ and the same variance $\langle(\theta - \langle\theta\rangle)^2\rangle = 2\left(\frac{k_B T}{\tau_2}\right)^2$,

$$P_E(\theta, 0) \simeq \frac{1}{\sqrt{4\pi}} \frac{\tau_2}{k_B T} \mathrm{e}^{\left(\frac{\tau_2}{2k_B T}\theta\right)^2}. \tag{3.31}$$

The evolution of this Gaussian profile under a constant torque will remain Gaussian, therefore, the temporal evolution of the mean and the variance are enough to describe the distribution $P_E(x, t)$. These both quantities can be obtained directly from the formal solution of the Langevin equation of the shaft (3.27)

$$\theta(t) = \theta(0) + \frac{1}{\gamma_0 + \gamma_L} \int^t (\tau_1 + \xi)\mathrm{d}t. \tag{3.32}$$

Averaging the stochastic angle $\theta(t)$ over different realisations, the mean and the variance at a time t are

$$\langle\theta\rangle = \frac{\tau_1 t}{\gamma_0 + \gamma_L}, \quad \langle\Delta\theta^2\rangle = 2\left(\frac{k_B T}{\tau_2}\right)^2 + \frac{2k_B T}{\gamma_0 + \gamma_L} t. \tag{3.33}$$

The coupling ratio is a measure of transduction effectiveness of the motor, measuring the fraction of ATP hydrolised molecules that produce a successful step. In this case, the coupling ratio corresponds to the fraction of the distribution

that falls at the right of the next maximum located at $\theta_0/2$ of the excited potential at a time t_E (Fig. 3.15)

$$cr(\gamma_L) = \int_{\theta_0/2}^{\infty} P_E(\theta, t_E)\mathrm{d}\theta = \frac{1 + \mathrm{fer}(\mu_c)}{2}, \tag{3.34}$$

with,

$$\mu_c = \left. \frac{\langle\theta\rangle - \theta_0/2}{\sqrt{\langle(\Delta\theta^2)\rangle}} \right|_{t_E}. \tag{3.35}$$

At this point it is worth to evaluate carefully the dependence of the coupling ratio with the friction of the load along the excitation time t_E. Since the mechanical time $t_{\mathrm{mech}\,1}$ is proportional to the effective friction coefficient $(\gamma_0 + \gamma_L)$ (3.13), the resulting probability density function after $t_{mech\,1}$ does not depend on the friction of the load during this first evolution period,

$$\langle\Delta\theta^2\rangle\big|_{t_{\mathrm{mech}\,1}} = 2\left(\frac{k_B T}{\tau_2}\right)^2 + \frac{2k_B T\alpha\theta_0}{\tau_1}. \tag{3.36}$$

On the contrary, the dependence of the distribution with the load firction appears in the waiting step of duration t_0. Since t_0 is independent of the friction of the load and the dynamics of the system with a lower friction are quicker to that of a system with a bigger load, the shrink of the left tail of the probability distribution function will be greater the smaller is the friction, increasing thus the coupling ratio of the motor.

So far, the current expression for the coupling ratio (3.34) does not take into account the reflecting part of the excited potential beyond its minimum. This force hinders the advance of the probability distribution increasing the area of the probability distribution that falls back to the initial state. This forbids a coupling ratio equal to 1 even in the best scenario case in which the stationary distribution around the minimum of the excited potential is reached. This is the situation in which the dynamics of the load is much faster than t_0 ($\gamma_L \to 0$). The

stationary distribution around the minimum of the excited potential is given by expression (2.41),

$$P_E^{\infty}(\theta) = \begin{cases} \dfrac{\tau_3\tau_2}{\tau_2+\tau_3} \mathrm{e}^{\frac{\tau_2}{k_B T}\theta} \\ \\ \dfrac{\tau_3\tau_2}{\tau_2+\tau_3} \mathrm{e}^{-\frac{\tau_3}{k_B T}\theta} \end{cases} \tag{3.37}$$

Being τ_3 the reflecting torque given by the slope of the excited potential (3.9). The corresponding coupling ratio for this probability profile is,

$$cr^0 = \int_{\theta_c}^{\infty} P_E^{\infty}(\theta)\mathrm{d}\theta = \frac{\tau_3\tau_2}{\tau_2+\tau_3}\mathrm{e}^{\frac{\tau_2}{k_B T}\theta_c}, \tag{3.38}$$

For the working parameters, this corresponds to a maximum coupling ratio of $\mathrm{cr}^0 \simeq 0.96$ which is in agreement with the computational results for trajectories with a small load. This result can be used in order to obtain a better approximation $\mathrm{cr}^*(\gamma_L)$ that can be written in a compact analytical way by interpolating the coupling ratio in (3.34) with the maximum value cr^0 (3.38),

$$cr^*(\gamma_L) = \frac{cr(\infty)(cr(0)-cr^0)}{cr(0)-cr(\infty)} + \frac{cr^0-cr(\infty)}{cr(0)-cr(\infty)} cr(\gamma_L), \tag{3.39}$$

returning a better prediction for the coupling ratio of the motor (Fig. 3.16). This coupling ratio explains thus the difference between the deterministic average approach and the stochastic simulations. Actually the coupling ratio can be used to obtain a better analytical description for the velocity,

$$\omega^* = \omega\, cr^*, \tag{3.40}$$

since the advanced distance along a trajectory used in the average velocity deterministic approach is reduced a fraction equal to the coupling ratio.

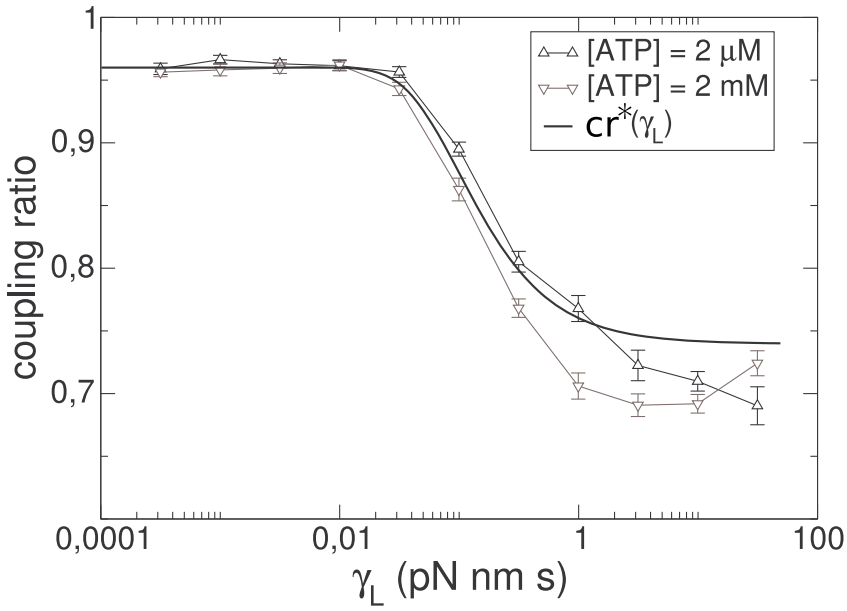

Figure 3.16: Results for the theoretical predicted coupling ration (*thick line*) versus the viscous friction of the load. This is contrasted with the numerical coupling ratio obtained for different ATP concentrations (*triangles joined by lines*).

3.2.3. F_1–ATPse white noise limit

In the previous section, the dynamics of the motor are treated analytically for the deterministic case, solving the noisy dynamics only by numerical means. However, the problem following the white noise Fokker–Planck methodology described in Sec. 2.4.2 can also be applied to study the system analytically from its noisy nature. For this purpose, the motor potential of the F_1 motor is introduced in the white noise limit Langevin equation (2.50). This results in an analytical expression for the probability flux of the shaft and thus the velocity of the motor (2.56).

For the sake of simplicity, a reduced potential description is chosen in which the relaxed state keeps its original form but the excited potential is substituted by the one corresponding to a constant torque $V'_E = \tau_1 = \Delta G_{\mathrm{ATP}}/\theta_0$. Therefore, in this case, the substeps are not taken into account focusing the study on a flashing potential with a complete symmetry of a third of a turn for both potentials (Fig. 3.17). For the F_1 motor, the rates of excitation and relaxation correspond with the inverse of the occupation times at each process of the cycle *i.e.* the inverse of the catalytic and the mechanical times (Eqs. (3.2) and (3.3)) respectively,

$$\omega_R = t_{\mathrm{dwell}}^{-1} = \left(t_0 \left(1 + \frac{k_0}{[ATP]} \right) \right)^{-1}, \qquad \omega_E = t_{\mathrm{mech}}^{-1} = \frac{\Delta G_{\mathrm{ATP}}}{\gamma \theta_0^2}. \tag{3.41}$$

With this description, the resulting Langevin equation (2.50) describes the behaviour of the shaft advancing along a tilted sawtooth potential (Fig. 3.18) and a white Gaussian noise with a spatial dependent intensity. The advance of the motor is not guided anymore by a flashing potential but through the jumping across the barriers of the potential. Introducing the actual expressions for the rates (3.41) into the general expression of the mean value of the potential noise $\bar{\eta}$ (2.43), the mean value of the dichotomous noise is

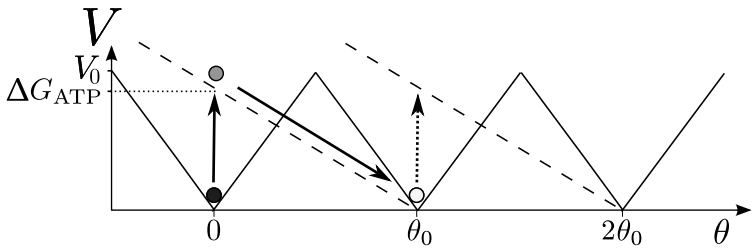

Figure 3.17: Scheme of the simplified flashing potential used for the Fokker–Planck analysis. The relaxed potential (*solid line*) and the excited potential (*dashed lines*) drive the dynamics of the motor. The scheme shows the advance of the shaft (*solid arrows*) along the full first step ($n = 0$), subsequent steps (*dotted arrow*) are equivalent.

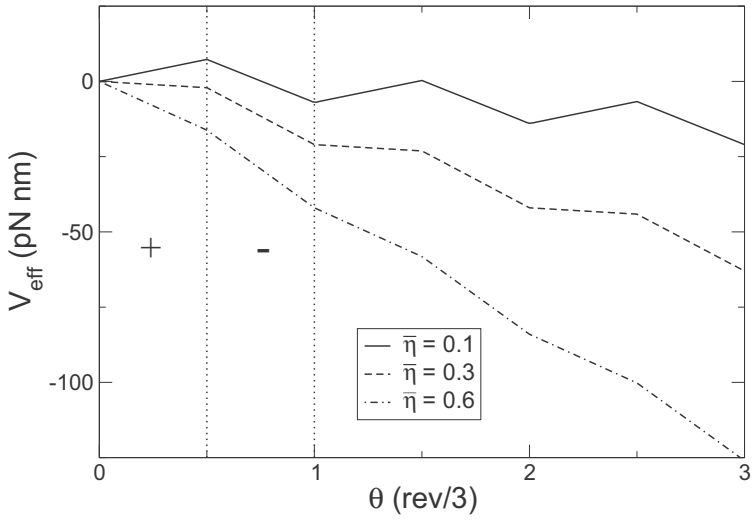

Figure 3.18: Effective potential for different values of the mean value of the dichotomous noise $\bar{\eta}$ and an ATP hydrolysis of 80 pN nm.

$$\bar{\eta} = \left(1 + \frac{\gamma\theta_0^2 t_M}{\Delta G_{\mathrm{ATP}}}\left(1 + \frac{k_M}{[ATP]}\right)\right)^{-1}. \tag{3.42}$$

This value is important because it is directly related to the effective torque averaged along a step θ_0

$$\langle V'_{\mathrm{eff}}\rangle_{\theta_0} = \frac{1}{\theta_0}\int_{\theta_0 n}^{\theta_0(n+1)} V'_{\mathrm{eff}}\mathrm{d}\theta = -\frac{1}{\theta_0}\int_{\theta_0 n}^{\theta_0(n+1)} \bar{\eta}\tau_E \mathrm{d}\theta = -\frac{\bar{\eta}\Delta G_{ATP}}{\theta_0}, \tag{3.43}$$

where it has been used the symmetry of the relaxed potential and (2.45). The average $-\langle V'_{\mathrm{eff}}\rangle_{\theta_0}$ coincides with the value of a constant torque that acting on the particle for a whole period entails the same potential increment that the effective potential, *i.e.* $\langle V'_{\mathrm{eff}}\rangle_{\theta_0}$, and consequently $\bar{\eta}$, returns the tilting of the effective potential (Fig. 3.18). This effective torque must not be confused with the average torque the motor exerts in time, which needs the dynamics of the shaft along the potential and can be extracted directly from Eq. (2.56).

The parameter $\bar{\eta}$ also controls the height of the effective potential barriers through Eq. (2.45) as a factor of V_R. There is a maximum of height for a minimum value of $\bar{\eta}$ ($\bar{\eta} = 0$), while the barriers disappear for a maximum value of the $\bar{\eta}$ ($\bar{\eta} = 1$) (Fig. 3.18). Thus the parameter $\bar{\eta}$ is acting as the driving element of the motor.

In addition the effective diffusion coefficient is not constant but can take two values as a function of the angular position: in the left zone of the rest state (+) of the effective potential it is found diffusion coefficient greater than the one in the right side of the rest state (−). This variability of the diffusion coefficient also assists the forward motion of the particle. The balance of these contributions is

$$g_+^2 - g_-^2 = \frac{6}{\pi^2}\Delta G_{ATP}\frac{\omega_E\omega_R}{(\omega_E + \omega_R)^3}, \tag{3.44}$$

being g_+ and g_- the fluctuation weight in the reflecting and advancing zone of

the effective potential.

The velocity predicted by the model through the flux has been computed for the parameters values of Table 3.3. The values chosen are based in the same experimental information used in previous sections. The resulting average velocity compares very well with experimental data specially for large values of the friction and large values of the ATP concentration (Fig. 3.19). Simulations of the dichotomous model without approximations can also be computed to compare exactly the differences obtained through the Fokker-Planck approach, obtaining a good match between them. The effective Langevin equation used (2.50) can also be solved numerically to reproduce motor trajectories, however, the numerical integration must be taken carefully since the multiplicative noise is discontinuous in space and therefore the standard stochastic integration methods fail to converge to the correct solution. A special algorithm solving this issue is covered at Appendix A.

Parameter	Fit Value
t_0	2.5 ms
k_0	18 μM
ΔG_{ATP}	70 pN nm
γ_0	10 pN nm ms
V_0	12 pN nm

Table 3.3: Parameter values of the model.

The white noise limit theory also provides the parameter ϵ that evaluates the goodness of the approximation (2.49). Here, through the comparison of the theory with exact results, the role of ϵ can be analysed clarifying analytically the

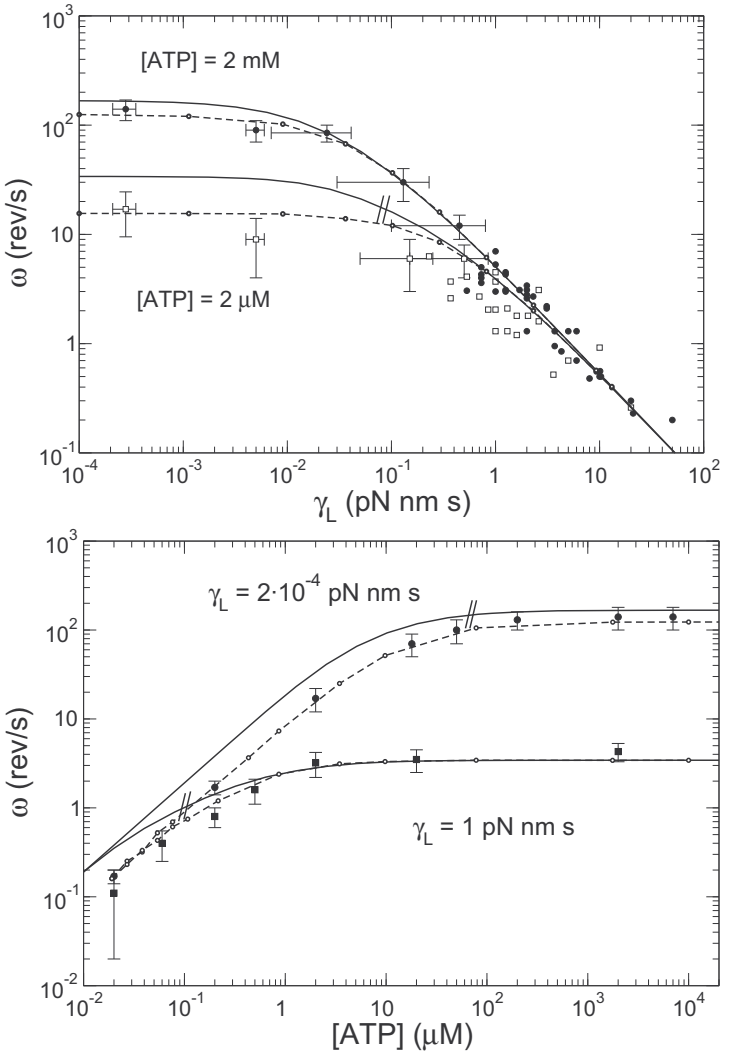

Figure 3.19: Angular velocity *vs.* load friction (Top) and ATP concentration (Bottom) where experimental data (*symbols*) from [94] and the Fokker–Planck prediction (2.56) (*solid lines*) are compared. Simulation results for the model with the dichotomous noise are also shown (*dashed lines*). Double slashes mark the position with $\epsilon_0 = 1.2$ for each curve. ϵ is greater than ϵ_0 to the right of the double slash. For [ATP]=2 mM, $\epsilon > \epsilon_0$ for the whole curve.

domains of this agreement. Fig. 3.19 shows that ϵ proves to be a good parameter to evaluate the accuracy of the theoretical prediction. For this motor it is found that the theory and experiments match well for $\epsilon > \epsilon_0 = 1.2$. Furthermore, the greater the parameter ϵ is, the better is the approximation. This property is quantified in Fig. 3.20 for different parameter values.

Also the power consumed (energy consumed per unit time) can be computed to compare the differences between the white noise limit and see if the predictions are also valid to measure the energetic performance of the motor. In this case, in order to compute the energy consumed for the white noise limit, the potential used for the energy consumption calculation (2.30) is

$$V(\theta, t) = V_R(\theta) + (V_E(\theta) - V_R(\theta))\,\pi(t), \tag{3.45}$$

where $\pi(t)$ is a white gaussian noise with the corresponding intensity of the motor flashing (2.48) *i.e.* the component of $\chi(t)$ different from $\xi(t)$. The resulting consumed power compares with the dichotomous case in a similar way than the average velocity in the expected variable domains (Fig. 3.21). For values of $\epsilon < \epsilon_0$ the power supplied prediction of the white–noise approximation decays much faster than the computational results.

The energetic analysis together with the results for the average velocity shows that the white noise limit proves to be a good analytical tool to describe the operation of biological molecular motors working in biological regimes. Actually, the goodness of the analysis is determined by the working regime of the motor increasing its validity for large values of [ATP] and the friction of the load. This corresponds to the situation where the relative duration of dwell times inside the cycle is shorter than the mechanical times and are well characterised by the control parameter ϵ. Thus, the white noise limit is a good analytical approach

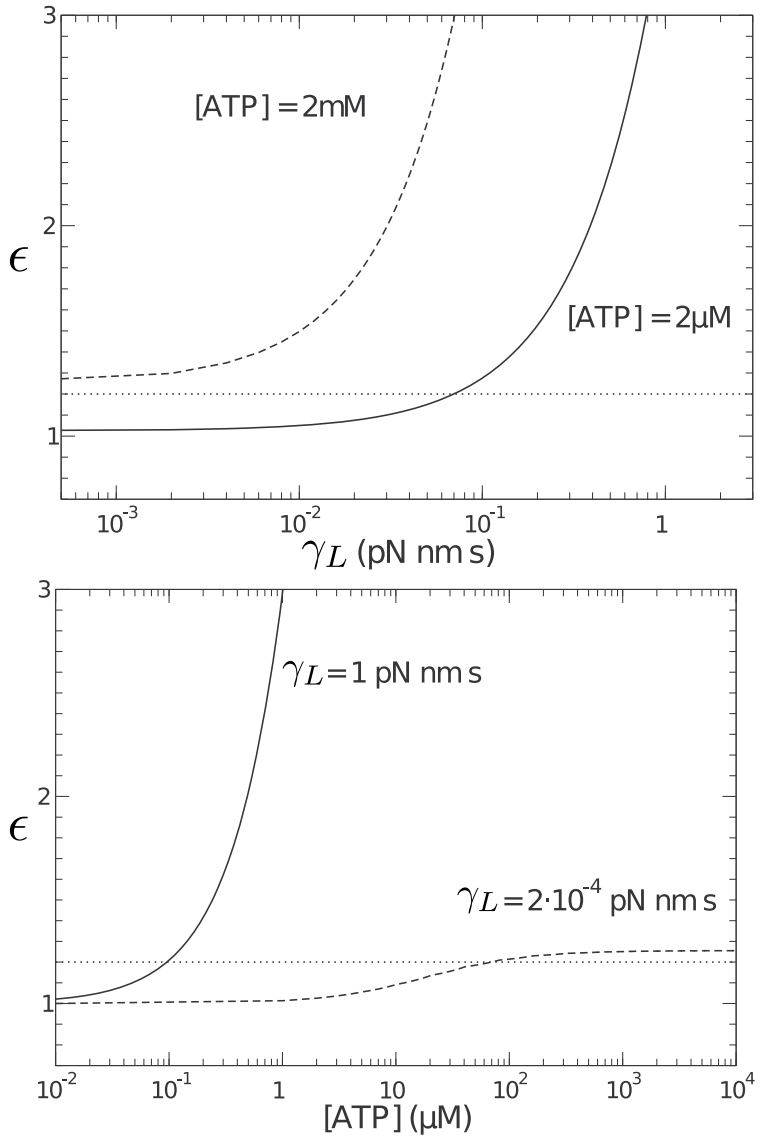

Figure 3.20: Results for the predictor ϵ for the same parameters value as in Fig. 3.19. Top: predictor *vs.* load friction. Bottom: predictor *vs.* ATP concentration. In both graphics the horizontal dotted line indicates $\epsilon_0 = 1.2$.

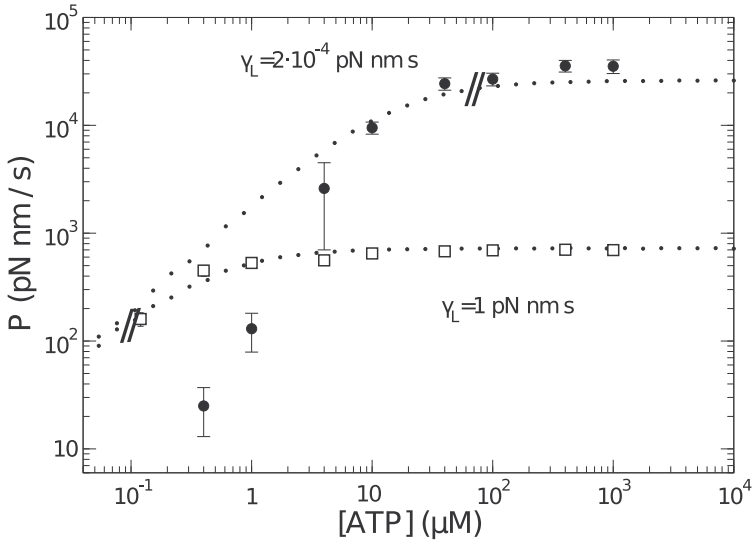

Figure 3.21: Comparison of the power consumed between the Fokker–Planck approximation (*symbols*) and the dichotomous model (*dots*). Double slashes mark the point in which $\epsilon = \epsilon_0$ getting $\epsilon > \epsilon_0$ to the right of the double slashes.

and can be used to analyse the operation of other molecular motors from its noisy nature following the same methodology described in this section.

3.3. F_1–ATPase under conservative torques

Thus far, the analysis of the behavior of F_1–ATPase is made from experimental observations where the only external force applied is that of the dissipative torque generated by the dragging of the attached load. However, the response of the motor under conservative forces can also be studied experimentally obtaining a different output from its dissipative counterpart. The performance of F_1 under assisting and hindering conservative torques and the corresponding input of energy and output of useful mechanical work are of special interest since

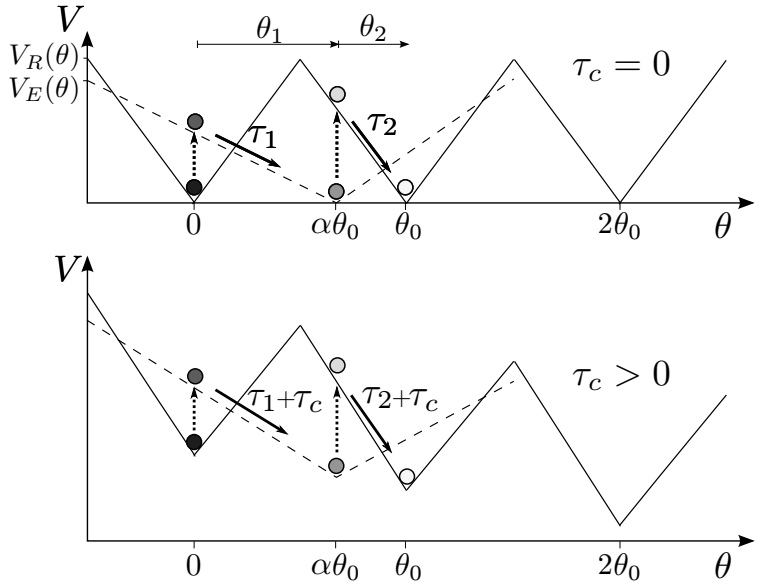

Figure 3.22: An external constant conservative torque is equivalent to consider a tilting of the motor potential.

F_1 motor works in the cell together with the F_0 transducing energy between them.

3.3.1. Effects of the conservative torque

The trivial consequence of a conservative force is the one reported in (2.14), where an additional torque τ_c is introduced directly in the Langevin equation of motion. This is equivalent to a tilting of the potential where the value of all the torques are increased by a quantity τ_c. (Fig. 3.22). Thus, the mechanical times required will change accordingly with the external torque applied (2.18)

$$t_{\mathrm{mech}_i} = \theta_i \frac{\gamma_0 + \gamma_L}{\tau_i + \tau_c}. \tag{3.46}$$

In contrast to the dissipative torque, the conservative torque acts at every

moment of the trajectory, even during the motor dwells. Actually, since the effective relaxed potential is tilted, the probability distribution of the shaft around the potential minimum is shifted (Fig. 3.23). Thus, the average starting point after a dwell changes. Consequently, there is also a change in the effective distance to cover during the next mechanical step once the flashing occurs. An assisting torque will reduce the distance to cover while a hindering torque increases it. The new average starting position for the next step can be analytically estimated from the equilibrium distribution $P(\theta)$ around the minimum of the relaxed potential, which can be approximated locally as an infinite linear piecewise well (2.41)

$$\begin{aligned} P_-(\theta) &= \frac{1}{k_B T}\left(\frac{1}{\tau_c+\tau_2}-\frac{1}{\tau_c-\tau_2}\right)^{-1} \mathrm{e}^{(\tau_c+\tau_2)\theta/k_B T} \quad , \quad \theta<0, \\ P_+(\theta) &= \frac{1}{k_B T}\left(\frac{1}{\tau_c+\tau_2}-\frac{1}{\tau_c-\tau_2}\right)^{-1} \mathrm{e}^{(\tau_c-\tau_2)\theta/k_B T} \quad . \quad \theta>0. \end{aligned} \tag{3.47}$$

The value of the shift $\delta\theta(\tau_c)$ is

$$\delta\theta(\tau_c) = \langle\theta\rangle = \int_{-\infty}^{\infty} \theta P(\theta)\mathrm{d}\theta = k_B T \frac{2\tau_c}{\tau_2^2-\tau_c^2}, \tag{3.48}$$

which increases linearly with the temperature. The dependence on the temperature points out that the shift is a result of thermal fluctuations. Without thermal fluctuations, the average relaxed position would always coincide with the minimum of the relaxed potential giving a null shift $\delta\theta(\tau_c, T\to 0)=0$.

Equation (3.48) will be valid only if the dwell time is long enough to allow the shaft to reach the equilibrium probability distribution. The shift (3.48) occurring during the ATP binding dwell changes the distance to cover during the first substep $\theta_1 \to \theta_1 - \delta\theta$ entailing a variation in the mechanical time (3.46). In the case of the second substep, the catalytic dwell time prior to the second stroke is not long enough to reach the equilibrium distribution [95]. Hence, the shift for

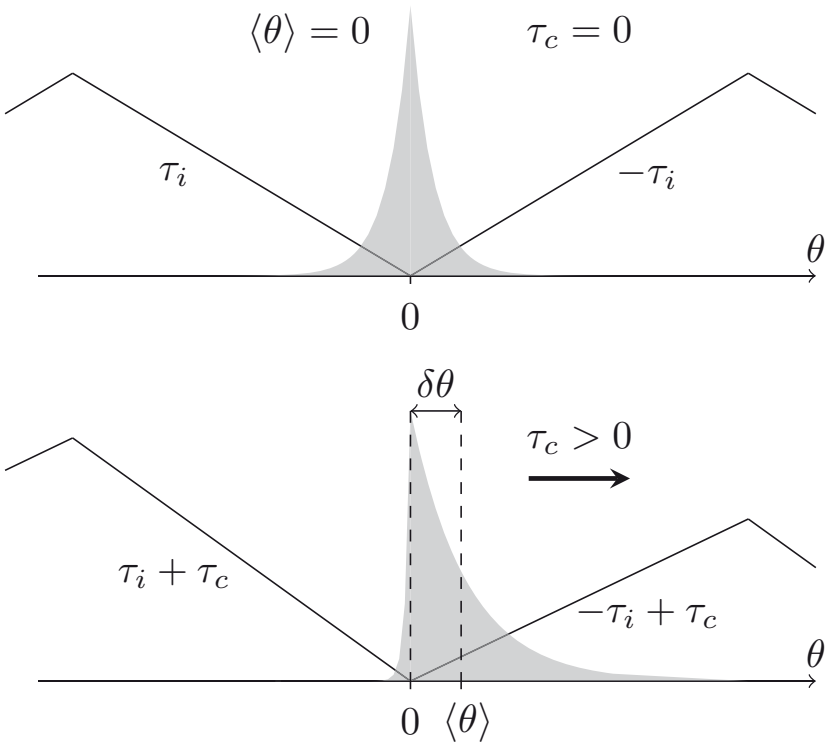

Figure 3.23: Effect of a conservative torque in the equilibrium probability distribution of the shaft (*grey shade*) during dwells around the minimum of a linear piecewise dwell (*solid line*). When no external torque is considered (Top) the profile is symmetric and centred in the minimum of the potential, while an external applied force (Bottom) shifts the profile changing the average position of the shaft from the minimum of the potential.

Parameter	Value
k_0^0	9.164 $\mu M^{-1}s^{-1}$
k_0^1	0.183 $pN^{-1}nm^{-1}\mu M^{-1}s^{-1}$
t_0	0.6 ms

Table 3.4: Experimental Setup Parameters used in the analysis of F_1 motor under conservative torques.

θ_2 will not be taken into account.

The phenomena introduced in expressions (3.46) and (3.48) through the effective torque and the distribution shifting have both a mechanical origin. However, chemical reactions are also affected by conservative torques. Experimentally, it has been observed that an assisting conservative torque reduces the dwell times while a hindering torque increases them [90]. Similar results have been observed for other molecular motors [39, 87]. An accepted theory to explain this phenomenon is that the catalytic site is deformed due to the external force [46]. Thus, the active conservative force modifies the biological structure of the machine and therefore changes the affinity of the catalytic site to ATP. This phenomenon is equivalent to consider the external torque as an external catalyst or inhibitor of the reaction [13]. However, due to the limited experimental information for the F_1, the relation of the reaction rate with the external torque is considered linear

$$k_{\mathrm{ATP}} = k_0^0 + k_1^0 \tau_c. \tag{3.49}$$

The values for k_0^0 and k_1^0 are obtained from the linear fitting of (3.49) to experimental observations [90] (Fig. 3.24) and gathered in table 3.4.

Thus, gathering the described dependences of the dynamics of the motor

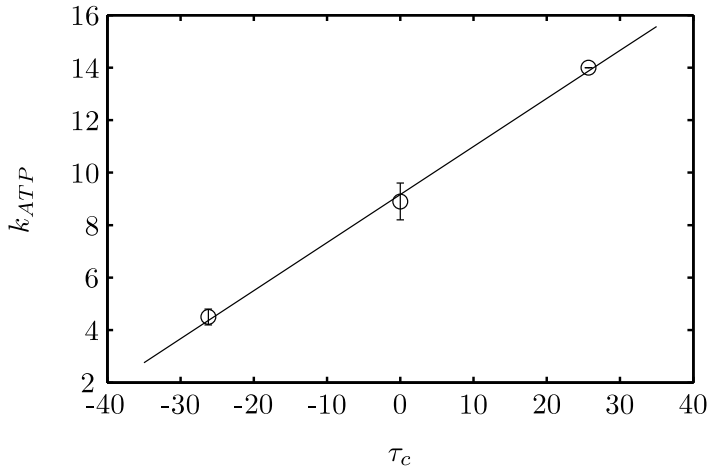

Figure 3.24: Experimental results for the ATP binding constant (*circles*). The linear fit returns the parameters used in (3.49) (Table 3.4). Data obtained from [90]

((3.46), (3.48) and (3.49)), the average change in the duration of the different processes composing the cycle can be used to write the average velocity as in (3.4)

$$\langle\omega\rangle = \frac{\theta_0}{[\theta_1 - \delta\theta(\tau_c)]\frac{\gamma_0+\gamma_L}{\tau_c+\tau_1} + \theta_2\frac{\gamma_0+\gamma_L}{\tau_c+\tau_2} + t_0\left(1+\frac{k_M(\tau_c)}{[ATP]}\right)}, \tag{3.50}$$

where, the dependence in τ_c has been stated explicitly. As in the purely dissipative case, expression (3.50) gives the velocity for a cycle with a full coupling ratio where all the reactions take place ideally. This preliminary expression for the velocity in the wide domain (-40,80) pN nm, returns a good prediction for the experimental values without fitting any new parameter from the velocity–torque experimental data (Fig. 3.25). This confirms that the effects of the conservative torque are well controlled by the model for the current precision of the experiments.

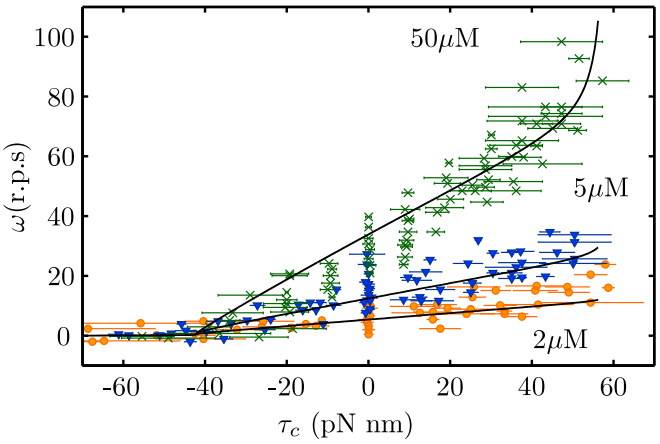

Figure 3.25: Comparison between the angular mean velocity predicted analytically (3.50) (*solid lines*) with experimental data (*symbols*) extracted from [90] with a corresponding friction of the load of $\gamma_L = 0.14$ pN nm s.

At this stage, it is interesting to note how torques of different nature (dissipative and conservative) makes the motor to respond differently even with torques of the same magnitude, providing different velocity–torque curves (Fig. 3.26). One particular feature of these differences is the stall force of the motor. For a conservative hindering torque, the motor stalls when the torque applied counters the lowest of the motive torques, $\tau_c(\text{stall}) = -\tau_1$. In contrast, one could guess that a dissipative torque will never be able to stop the motor. Nevertheless, for large enough values of the friction of the load, the motor velocity decreases so dramatically that the dissipative torque tends to a constant value, which can be calculated from (3.50),

$$\tau_{\text{diss}}(\text{stall}) = \gamma_L \omega|_{\gamma_L \to \infty} = \frac{\theta_0}{\frac{\theta_1 - \delta\theta}{\tau_1} + \frac{\theta_2}{\tau_2}}. \tag{3.51}$$

This result also shows that the average stall dissipative torque can be larger

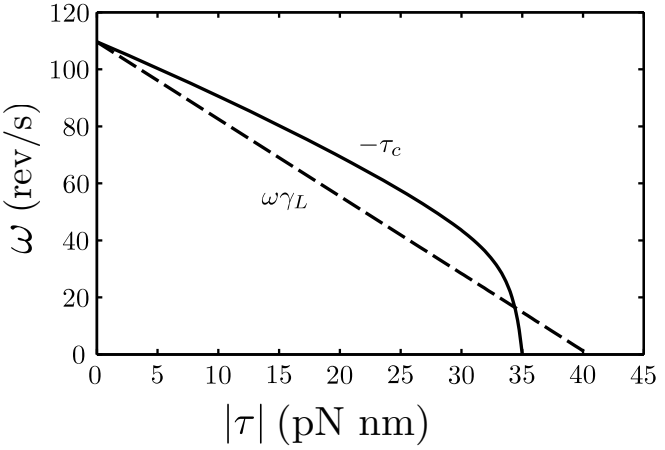

Figure 3.26: Comparison of the resulting torque-velocity curve (3.50) for hindering conservative torques (*solid line*) and dissipative torques in the same range of values (*dashed line*). The dissipative torque is obtained through the variation of γ_L. Parameters used are $\gamma_L = 0.14$ pN nm s for the conservative torque and buffer conditions of [ATP]=50 μM.

than the internal torques of the motors, which is not true for the conservative case. Therefore, this result reveals the complexity of evaluating the performance of the motor, highlighting the importance of considering the nature of the torque together with the actual motor potential.

3.3.2. Numerical analysis

Following the same methodology as in the purely dissipative case, the stochasticity of the system can be studied through stochastic simulations. While the tilting effect is introduced directly from the Langevin equation, the shift change in mechanical times and the ATP binding rate are introduced by changing accordingly the flashing dynamics. The simulation results are quantitatively similar to those of the deterministic theoretical prediction (Fig. 3.27). However, simu-

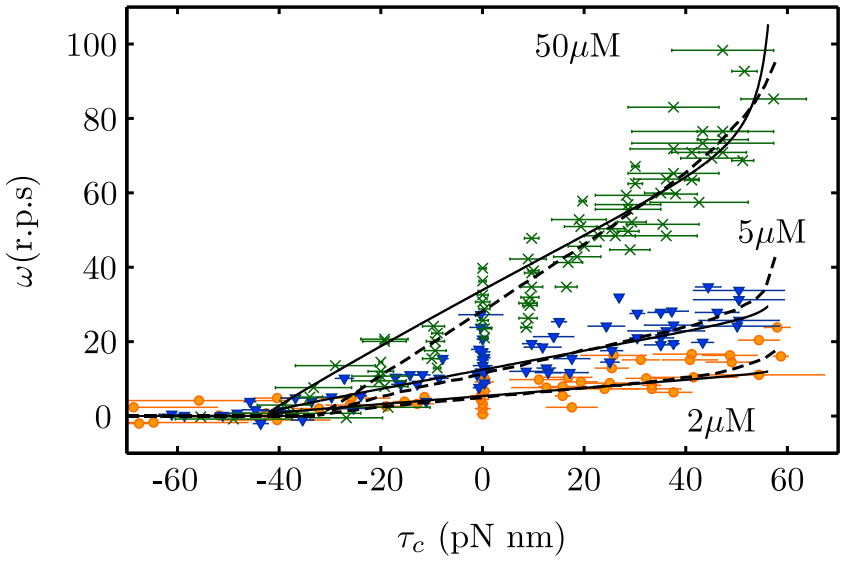

Figure 3.27: Angular mean velocity versus conservative torque for three ATP concentrations. Analytical prediction (3.50) (*solid lines*) and numerical simulations (*dashed lines*) are compared with experimental data (*symbols*) extracted from [90] with a corresponding friction of the load od $\gamma_L = 0.14$pN nm s.

lations show again a better prediction that, in contrast to the pure dissipative case, returns faster velocities than the deterministic prediction for large values of the external torque and slower velocities lower values of the torque. Differences between the average analytical prediction and the simulations become larger for high assisting or hindering torques where not only the coupling ratio is more important but also the approximation (3.47) is no longer valid. For larger torques, the motor potential is not able to arrest the motor in one minimum obtaining a motion of the motor out of the motor cycle.

Is of special interest the behaviour of the motor for high hindering conservative torques. The time distribution proposed for the mechanical times is based on the strict motor cycle coupled with the potential timing. This is valid as long

as the external conservative torques are smaller than the internal motive torques of the motor. Once the internal torques are exceeded, the motor is not able to retain the shaft and the stepping is not driven by flashing assisting torques but by jumps through a set of potential barriers. In this regime, experimental information is very poor and no conclusive statements can be formulated. Two different behaviours have been observed: The motor either stalls and stays fixed for large values of the torques or breaks and rotates backwards [50, 90], this event is known as slippage. The stalling regime suggests that the excited state is not stable when the motor goes backward flashing to the relaxed state, which is able to retain the motor. This can reflect that the relation (3.49) is not linear anymore and there is a chemical stalling of the motor. Therefore, in general the motor is able to retain the shaft for hindering torques larger than the excited advancing torque (Fig. 3.28).

In contrast, the slippage effect shows that the stalling mechanism does not always work. In terms of the current model, this would mean that the motor is not able to flash to the relaxed state. It remains in the excited state and hence a high enough hindering torque may cause backward steps. This is equivalent to the case of a particle falling along a tilted sawtooth potential. Experiments show that the slippage effect is not permanent, but lasts only a few steps. Therefore, the experimentally observed backward velocity will have a maximum value corresponding with the situation in which the particle is trapped all the time in the excited state *i.e.* in the slippage regime. However, since motor present both behaviours, slippage and stall behaviour, the velocity measured must take an intermediate value. (Fig. 3.28).

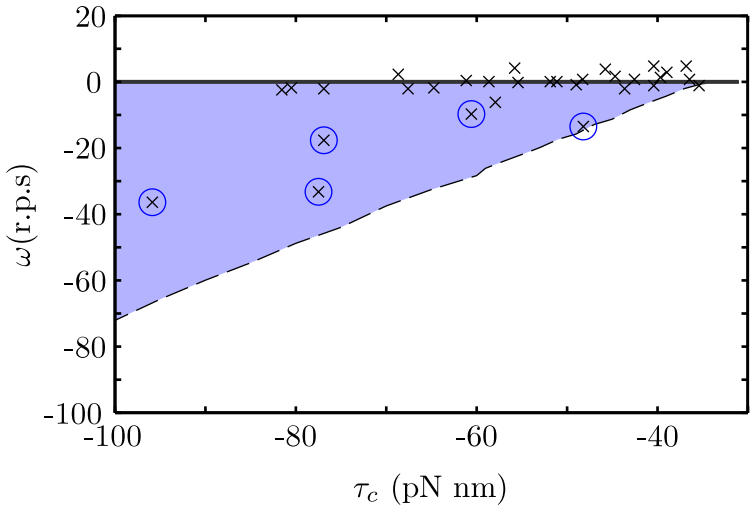

Figure 3.28: Average F_1 angular velocity for high values of the hindering torques. Experimental observations (*crosses*) show that usually the motor stays still around $\omega = 0$; however, some measures contain slippage events (*crosses inside circles*) that allow backward rotation. The velocity during the slippage is the one fixed by the excited potential (*dashed line*), while the measured velocity must be a result of a mixture of both behaviours, fixed and slippage (*shaded area*). Experimental data are extracted from [90].

3.4. Energetics of F_1–ATPase

Considering that the role of the F_0F_1 complex is the transduction of energy, the understanding of F_1–ATPase energetics is essential to comprehend this motor. It is expected for the components of ATP synthases to have evolved to transduce energy in the most effective way. Unfortunately, energetic magnitudes are not direct observables from experimental results. In particular, the occupational state of the motor or the ATP hydrolysis are not available experimentally. Nevertheless, the motor potential developed in previous sections have proved to gather the physics of the motor and can be used to predict the energetic performance of the motor. Again, the study can be made from the analytical deterministic prediction or from the stochastic simulations, which give a more realistic information. In this section, the analytical expressions for the deterministic analysis are stated explicitly, while the methods for extracting the information on the energetics from stochastic simulations are those described in Section 2.3.

The first energetic discrepancy between both predictions is the actual energy input. While in the deterministic approximation the input energy of the system is always that of the energy hydrolysis of ATP, in the stochastic model not all the flashings take place exactly in the potential minimum and the energy will be different for different cycles (Fig. 3.14). In fact, due to the geometry of the motor, the energy introduced per cycle in the system is always lower than the energy of the hydrolysis of the ATP and will depend on the experimental conditions (Fig. 3.29) never exceeding 1-2 k_BT. This loss of energy will be considered an intrinsic loss of the motor and not a variation in the hydrolysis input energy.

Since the input energy in the ideal case is that of the hydrolysis of ATP per

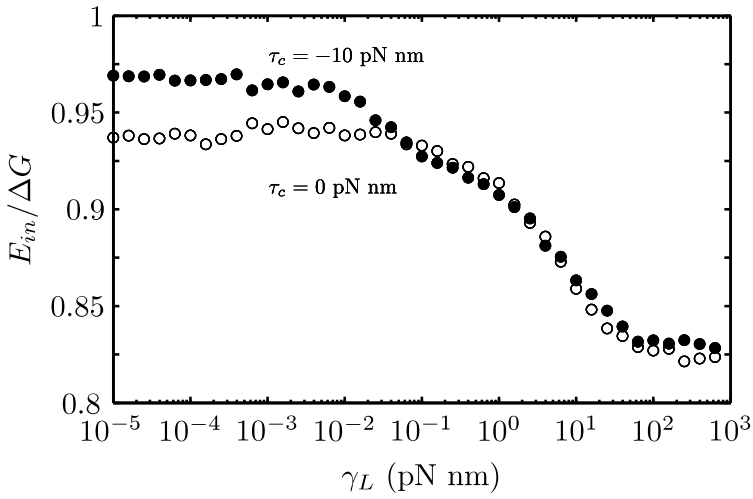

Figure 3.29: Ratio between the input energy of the motor per cycle and the hydrolysis energy of the ATP for different experimental conditions.

cycle, the input power that can be obtained proceeding as in (2.32),

$$P_{\text{in}} = \frac{\Delta G_{\text{ATP}}}{\mathcal{T}}, \tag{3.52}$$

being, $\mathcal{T}$ the average time that takes a full cycle of the motor (2.2). On the other hand, the input energy can be transduced in useful energy W_{out} through a hindering force τ_c or dissipated as heat Q through the load and the shaft. The output useful power obtained through τ_c, corresponds in the ideal deterministic case with,

$$P_{\text{out}} = \tau_c \langle \omega \rangle, \tag{3.53}$$

which returns the classical parabolic relation with τ_c (Fig. 3.30). The output power is null at $\tau_c = 0$ and at the stall torque $\tau_c \simeq 35$ pN nm, achieving a maximum power value for an intermediate value of the hindering torque. The power is also very sensitive to ATP concentration. Low concentrations of ATP result in longer dwell times reducing the velocity of the motor and with it the

output power. In simulations, a much lower value of the useful power is obtained (Fig. 3.30). This difference comes mainly from missing steps which do not provide useful work even consuming energy (Sec. 3.2). Not only the magnitude of the power is decreased but also the value of the conservative torque that maximizes the power is shifted. Again, this shift is a signature of the noisy nature of the leading mechanism of the motor. Hence, this shift is of special interest if the motor is expected to have evolved to work in an optimum value of the power.

With the output power information, the efficiency of the motor can also be obtained (2.33). For the deterministic case, the efficiency is linear with the conservative torque (Fig. 3.30),

$$\eta = \frac{P_{\text{in}}}{P_{\text{out}}} = \frac{\tau_c \theta_0}{\Delta G_{\text{ATP}}}, \tag{3.54}$$

This returns a maximum of efficiency for a maximum value of the torque *i.e.* for the stall torque. In this situation the motor would work infinitely slow but with a minimum dissipation.

On the other hand, the stochastic simulations diverge completely with the deterministic prediction for high values of the hindering torque (Fig. 3.30). While the deterministic case predicts an efficiency maximum at maximum torque, the missing steps, that increase with the hindering torque, produce a decay in the velocity. This results in a dramatical decay of the efficiency near the stall torque when thermal fluctuations are considered. In opposition to the power, the efficiency does not generally depend on the dwell times. During the dwell times, there is no input of energy neither energy output. Therefore, there is no dependence of the efficiency with [ATP]. On the other hand, due to the dependence of the coupling ratio with the friction of the load (Fig. 3.16), the efficiency is sensitive to γ_L. The maximum efficiency for the stochastic case (around 40 %) is obtained at an average value of $\tau_c \simeq 20$pN nm which is again of special interest in studying the optimisation properties of the motor.

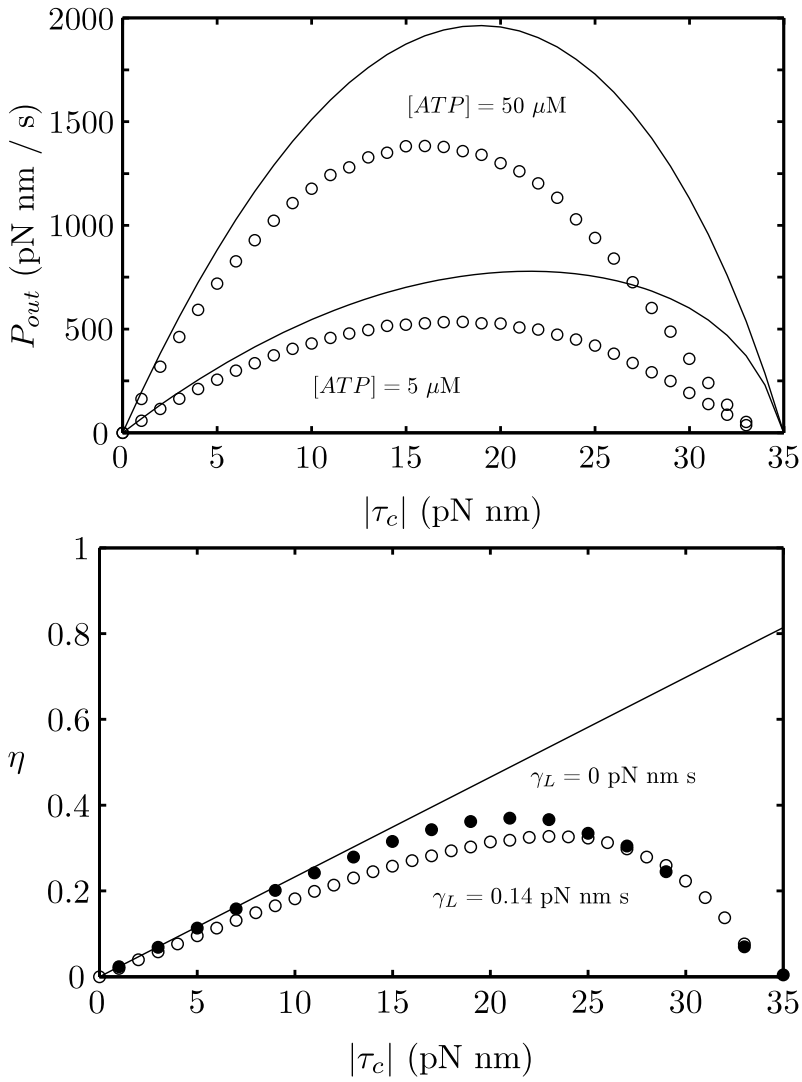

Figure 3.30: Useful output of the motor under a constant conservative torque τ_c. The Stoke's prediction (*lines*) and the stochastic analysis (*circles*) are compared. Top: Useful power ($\gamma_L = 0.14$ pN nm s). Bottom: Efficiency ([ATP]=50 μM).

The same analysis of power and efficiency can be applied to the dissipative torque. However, this energy is not used but is dissipated to the thermal bath (it cannot be stored). This energy is employed partially in dragging the load across the medium. Since the drag of the load is not conservative, the fraction of energy dissipated through the load depends on the trajectory of the motor. Therefore, the average velocity is not enough information when computing the average dissipated energy. However, as in the case of the conservative scenario, the average ideal velocity gives an approximation and an upper boundary to the real expected value.

Since the coupling between the shaft and the load is stiff, the dissipation is proportional to the friction of the shaft–load and, therefore, the energy dissipated through the load per unit time is,

$$\dot{Q}_L = \frac{\gamma_L}{\gamma_0 + \gamma_L} \frac{\Delta G_{\mathrm{ATP}}}{\mathcal{T}}, \tag{3.55}$$

for the case in which no conservative torque is present and all the energy introduced is dissipated. Again, there is a maximum power at an intermediate value of the torque (Fig. 3.31). Low values of the dissipative torque, correspond to low values of the load friction, where the internal friction of the motor dissipates all the energy returning $\dot{Q}_L = 0$. In contrast, large values of the dissipative torque correspond to large values of the load, which slow down the motor and therefore the transduction rate, obtaining again a null value of the dissipative power. From simulation results, the same behaviour is obtained but with a lower dissipation through the load.

Also the ratio between the energy dissipated by the shaft and the input energy (Stoke's efficiency) (Sec. 2.3) can be studied,

$$\eta_L = \frac{\dot{Q}_L}{P_{\mathrm{in}}} = \frac{\gamma_L}{\gamma_0 + \gamma_L}, \tag{3.56}$$

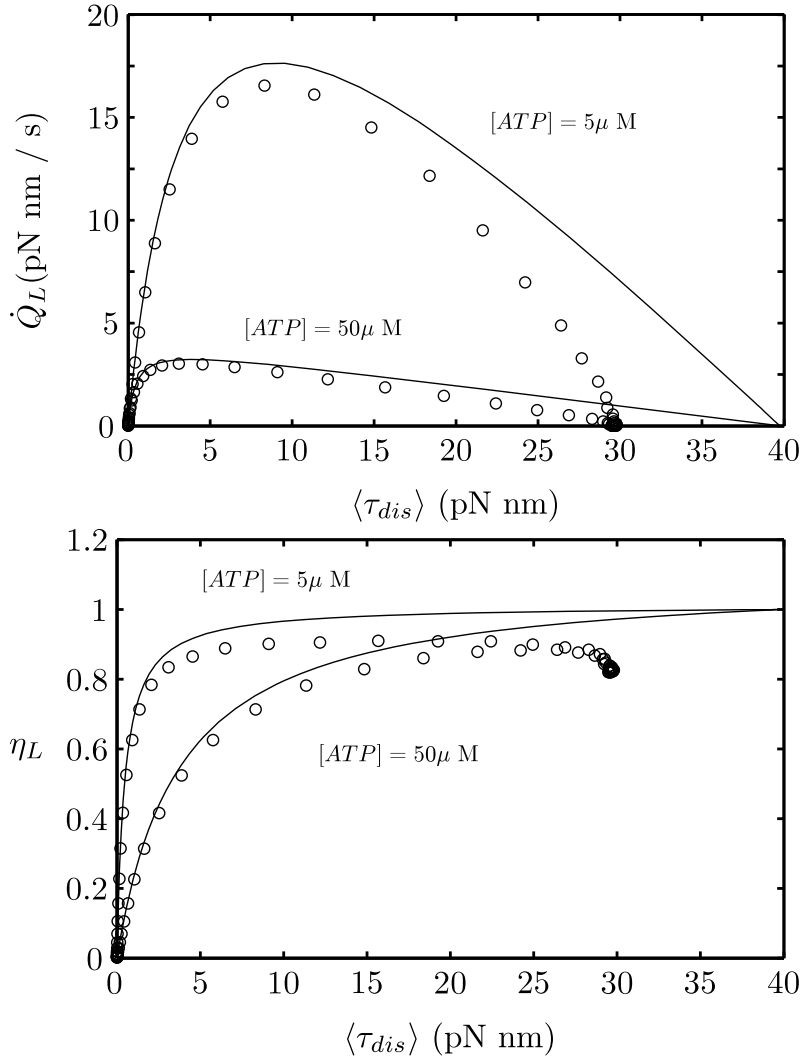

Figure 3.31: Dissipation through the load for different values of [ATP]. The Stoke's prediction (*lines*) and the stochastic analysis (*circles*) are compared. Top: Dissipated power through the load. Bottom: Ratio between the energy dissipated by the load and the energy dissipated through the shaft.

so the fraction of energy dissipated by the load increases with the load friction. Since all the energy must be distributed between the load and the shaft, for large values of the friction of the load, almost all the energy is dissipated via the load (Fig. 3.31). In simulations, a similar behaviour is obtained. The dissipative efficiency is larger than the conservative counterpart but this only means that energy is more easily dissipated than stored in a conservative potential.

Thus, all the energetic results gathered in this section points out two important ideas. First, the resulting energy outputs and efficiencies decrease once all the noisy dynamics of the motor are taken into account. The second remark is that there is a change in the value of the torque that optimises the different energetic magnitudes. This result can not be obtained directly from the initial observations of the trajectory and makes necessary the proposal of a specific motor potential developed in the previous sections from different experimental observations and the correct analysis through its noisy dynamics.

4

Ion flux driven motors

In the previous chapter, motors operating with ATP hydrolysis were studied. In contrast, there is a second primary source of energy in the cell driving molecular motors: electrochemical potential across membranes.

Energy from ionic gradients can be managed in a similar way to macroscopic batteries. In this case, the energy is generated and preserved through the ionic concentration across biological membranes. An ion crossing a membrane has an associated energy due to electrostatic and entropic contributions. For this reason the electrochemical energy associated to ionic gradients is also referred as membrane potential. In contrast to nucleotide driven motors, where the energetic carrier diffuses through the aqueous cytoplasm, the energy of the ionic gradient is stored locally, through the membrane. For this reason, a motor using its energy must be placed across the membrane allowing an ionic flux across the machine. This flux will be finally transduced by the machine. Actually, transmembrane motors not only uses the ionic flux but can also store energy in it by pumping ions reversing the direction of the spontaneous flux determined by the membrane potential.

Ionic channels are the passive counterpart of ion driven molecular motors

where no energy is transduced in the translocation. Both biological structures, channels and machines, work with a very high specificity for a certain ionic species *i.e.* they only allow the translocation of one specific ionic species despite the similarity between different ions. Ionic rotatory molecular motors mainly operate with protons (H^+) or with sodium ions (Na^+) for the case of the BFM of some bacterial species.

In order to study the membrane potential, it is interesting to measure which is the energy variation of the ion of the corresponding species crossing the membrane. This energetic difference has two components, namely, an electrostatic and an entropic component (Fig. 4.1). On the one hand the electrostatic component ΔV originates with the difference in charge of the cytoplasm at both sides of the membrane. This difference creates an electric field inside the membrane that drives any ion crossing the membrane. On the other hand there is an entropic component of the membrane potential driven by the diffusion of ions across the membrane when there is a difference in concentration at both sides. Thus, even in the situation where the ions were not charged particles, a difference in concentration at each side of the motor would generate a directional net flux driving the system to the homogeneous state. This flux can also be transduced by the molecular motor. With both components, the membrane potential reads,

$$\Delta\phi = \Delta V + k_B T \ln \frac{\rho_1}{\rho_2}, \tag{4.1}$$

where ρ_1 and ρ_2 are the ionic concentration at each side of the membrane. From this energy, an associated force can be derived known as Ionic Motive force (IMF) or Proton Motive Force (PMF) for the case of H^+ ions. This ionic force corresponds to a homogeneous force acting on the ion along the membrane width D, $IMF = -\phi/D$.

Experimentally, the study of rotatory molecular motors presents similar challenges than the nucleotide ones, such as the lack of observation of the energetic

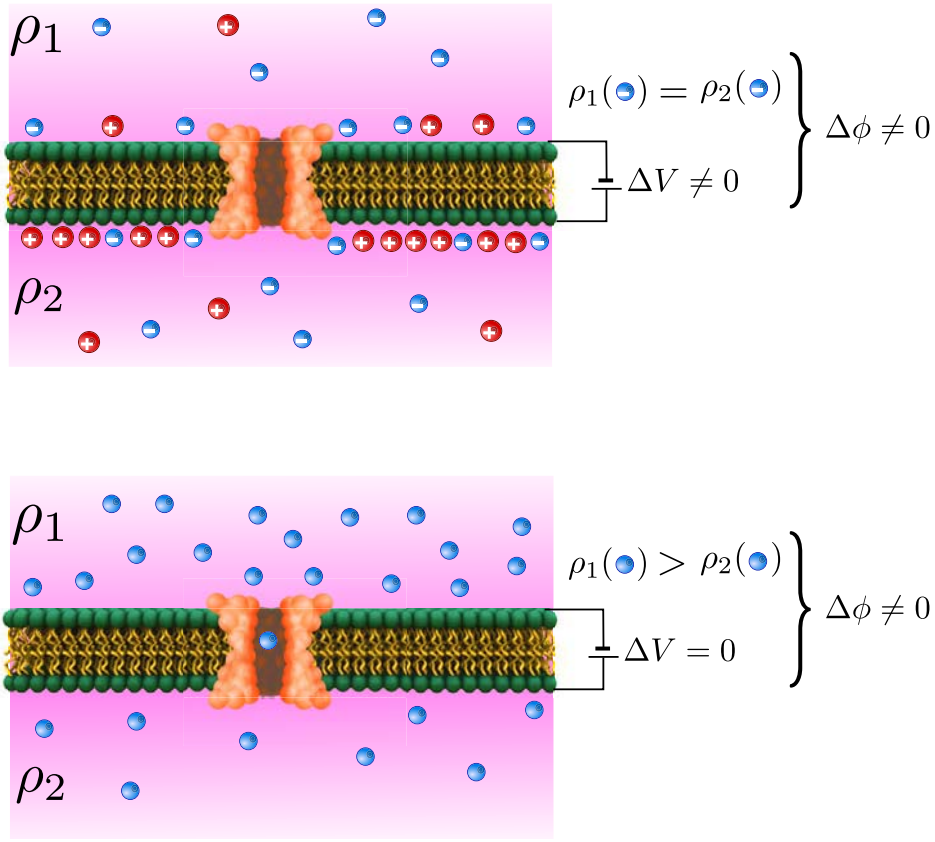

Figure 4.1: Membrane potential generating the Ionic Motive Force can be used by transmembrane proteins that operate with the directional flux of particles. Top: The electrostatic component of the membrane potential is generated by a difference in electric charge at each side of the membrane. In this case, the density of the translocable ionic species $(-)$ is the same at both sides but another ionic species $(+)$ generates the charge difference. Bottom: The entropic component of the membrane potential is driven by diffusion and appears from a concentration difference across the membrane.

transduction, in this case the measure of the ionic flux. Furthermore, transmembranal motors have an additional difficulty: they must be placed across a membrane with well controlled conditions at each side. This problem has been tackled experimentally in two different ways. On the one hand the use of liposomes, spherical lipidic vesicles, prepared with the desired conditions and containing the desired motor in its surface. This method has been applied in the study of the F_0 motor [91, 92]. Such a set up allows to measure directly the actual ionic density inside the liposome, and therefore gives and indirect measure of the flux. However, it makes difficult to track the rotation of the motor. On the other hand, rotational assays can be performed using the biological native membranes. This can be done in BFM assays where flagella can be detached from the motor and replaced by a load [28, 80]. This set up allows longer and more precise trajectories than the obtained with the liposome but does not allow the tracking of the flux.

4.1. Minimal transduction cycle

Again, the average velocity of the motor is available from the knowledge of the duration and length of each transduction cycle. In this case, the mechanical time (2.18) will be determined by the membrane potential energy, and the chemical time (2.7) by the ionic concentration of the driving side, obtaining

$$\omega = \frac{\theta_0}{t_0 \left(1 + \frac{k_0}{\rho_1}\right) + \theta_0^2 \frac{\gamma_0 + \gamma_L}{\Delta\phi}}. \tag{4.2}$$

In this description the possibility of an ion crossing the motor opposing the gradient and reversing the flux is neglected. The average velocity obtained can be compared with experimental assays on the BFM [36] obtaining a good match (Fig. 4.2). These experiments studied *Vibrio alginolyticus* where the motor works with

Parameter	Value
$[Na^+]_{in}$	5 mM
θ_0	$2\pi/26$
t_0	4 ms
k_0	5 μM s
γ_0	26 meV s

Table 4.1: Parameters of the model used in Fig. 4.2. Biochemical values extracted from [36].

sodium ions crossing the peptidoglycan membrane. Hence, in this description, $\rho_1 \equiv [Na^+]_{ex}$ and $\rho_2 \equiv [Na^+]_{in}$. It is interesting to note that the effect of both components of the membrane potential do not affect in an equivalent way to the measured velocity. While a change in ΔV only modifies the actual value of $\Delta\phi$, a change in the ionic concentration ρ_1 not only modifies $\Delta\phi$ but also affects to the waiting chemical time. This effect, experimentally reported [36], is showed in Fig. 4.2.

This preliminary result does not take into account the complex stechiometry of ion driven molecular motors absent in nucleotide hydrolysis motors *i.e.* which is the number of ions needed to perform each rotor step. Actually, a measure of the energetics of rotatory motors shows that usually a fractional number of ions is necessary to perform one motor step [60]. This problem is stressed when several stators can be attached to the same rotor, as it happens with the BFM. All these issues are translated in a loss of the picture of a single transduction cycle tightly coupled with the motive coordinate. In order to tackle this problem, more complex models following the average Stoke's description can be tested (Chap. 6). Nevertheless, such approaches are unable to account naturally for the mechanistic interaction of the transduction process and its relation with the flux. For this

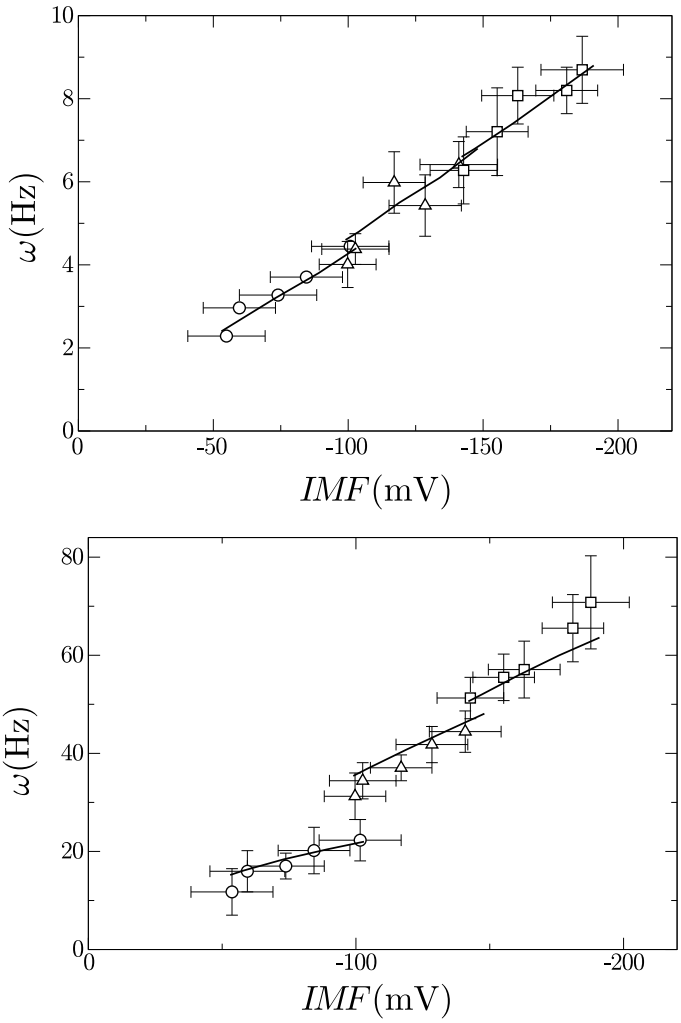

Figure 4.2: Average velocity of the motor *vs.* Ionic Motive Force for Bacterial Flagellar Motor for different values of $[Na^+]$ and load size. Experimental results (*symbols*) [36] show a nonlinear dependence with the IMF predicted by (4.2) (*lines*). Top: Assays with a large spherical load of 1μm radius ($\gamma_L = 520$meV s). Bottom: 0.35μm radius ($\gamma_L = 31.2$meV s). $[Na^+]_{ex}$=85mM (*squares*), $[Na^+]_{ex}$=10mM (*triangles*) and $[Na^+]_{ex}$=1 mM (*circles*). The rest of parameters are gathered in Table 4.1.

purpose a different model focused in the mechanical transmission between motor and particles is developed in the following section.

4.2. Ionic turbines

The coupling between flux and mechanical work is well known in the macroscopic world. Such machines include the windmill or the Archimede's screw, and can be referred in a general way as *turbines*. The basic principle for these devices is that of a certain fluid colliding with the vanes of the turbine that generates the rotation of the motor. Such motors can also reverse their work regime by forcing externally the rotation of the motor in a direction opposite to the flux and being able to invert the natural direction of the flux *i.e.* turbines can also work as pumps.

Actually, this general description can be applied to ion motive rotatory devices in which the flux of ions is coupled to the rotation of the motor. Note that following this description where different forces act on a vane on a continuous way does not need of the transduction cycle timing described previously. Furthermore, it also gathers the basic features of ionic turbines. For instance, one of the main differences between hydrolysis motors and ion motive motors is the possibility to reverse the rotation direction directly from the chemical energy source. In the F_1–ATPase motor, the hydrolysis of ATP produces a directional rotation that can only be reversed through an external conservative force opposing the rotation of the motor and promoting the ATP synthesis. Nevertheless, ionic turbines can change its directionality due to a change in the direction of the Ionic Motive Force.

4.2.1. The simplest mechanistic case

One simple model to start the study of such systems is that of a purely mechanistic device where a piston of section A and length D separates two particle reservoirs (Fig. 4.3). Following the symmetry of the rotor, when the piston reaches one of its ends another piston enters again from the other end. Accordingly, in each step of length D a volume $V_0 = DA$ of particles is translocated between both reservoirs. The dynamics equation for the rotation will follow again the reported Brownian overdamped dynamics, in opposition to macroscopic turbines (2.11),

$$\gamma \dot{x} = \overline{F} + \xi(t). \tag{4.3}$$

Here, the spatial coordinate of the turbine is the linear position normal to the membrane width and is labelled x to differentiate it from the angular coordinate of the motor θ. Despite this change in the reference system, spatial and rotatory coordinates are directly related and can be easily transformed between them. The rest of elements of elements in (4.3) are equivalent to those described in (2.11) where the sum of forces $\overline{F} \equiv \sum_i F_i$ has two main components $\overline{F} \equiv F_p - F_{\mathrm{c}}$. The force F_p is the average force that the particles exert on the piston, while the external force F_{c} extracts or introduces work into the system. For the sake of simplicity, the particles can be considered to behave as an ideal gas so their contribution corresponding to the balance between the pressure (P_i) of both reservoirs can expressed as

$$F_p = (P_2 - P_1)A = k_B T A(\rho_2 - \rho_1), \tag{4.4}$$

obtaining a linear dependence on the concentrations. This relation for the force has been tested numerically to be the force that two non–interacting Brownian gases apply on the piston for biological parameters (Table 4.2)(Sec. 4.2.3). More complex dependences for F_p can be considered taking into account individual ions

Parameter	Value	Description
kT	4.1 pN nm	Biological Temperature
γ	10 pN nm μs	Stokes friction for a sphere of radius $\simeq$ 8 nm
A	150 nm^2	Section of a channel of 7 nm radius
D	4 nm	Width of F_0 motor
ρ_2	20 mM	Biological concentration

Table 4.2: Biological parameters used for testing the molecular turbines.

and membrane potential. However, they will still contain the physical phenomena described hereon that will only depend on the generic net force $\overline{F}$. Without loss of generality, $\rho_1 > \rho_2$ will be fixed. This way, when no external force is applied the velocity and the flux are defined positive. Also F_c has been considered to be positive when it hinders the movement *i.e.*, $F_c > 0$ is a force used to extract work from the turbine or to pump particles against the gradient (Fig. 4.3).

The mean velocity $v = \langle \dot{x} \rangle$ can be obtained by averaging eq. (4.3) coinciding with the steady state Stoke's velocity (Fig. 4.4),

$$v = \frac{\overline{F}}{\gamma} = \frac{(\rho_1 - \rho_2)Ak_BT - F_c}{\gamma}. \tag{4.5}$$

This simple result returns a linear decreasing function of the the velocity with external force F_c. The external force that stalls the motor is,

$$F_c(v = 0) \equiv F^M_{\text{stall}} = (\rho_1 - \rho_2)Ak_BT. \tag{4.6}$$

For larger values of F_c than the stall force, the velocity of the motor will be reversed forcing the piston to advance against the particle gradient. Equivalently, for a fixed value of the external force, a motor stall gradient appears (Fig. 4.4),

$$\Delta\rho^M_{\text{stall}} = \frac{F_c}{Ak_BT}, \tag{4.7}$$

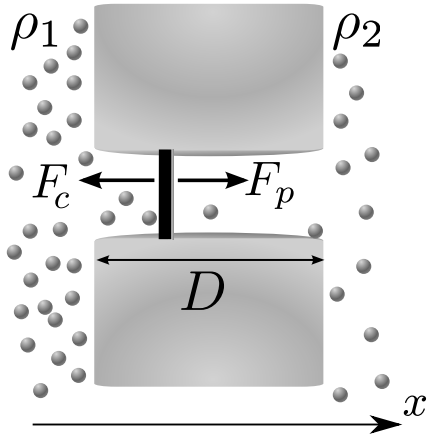

Figure 4.3: Scheme indicating the working of the piston turbine. The black piston has periodic boundary conditions between both motor ends. The position x, the force of the particles F_p and the external force $F_{\rm c}$ are considered positive in the direction of each respective arrow.

for which the velocity of the motor is reversed.

The particle flux that crosses the turbine is quantified as the average number of ions that are transported across the membrane per unit of time. Therefore, the flux is related with the velocity of the motor and the ionic density at each side of the turbine. For a turbine that advances with a constant velocity, the flux in the deterministic approximation (without considering thermal fluctuations) can be calculated as the number of particles ($V_0\rho_i$) that are transported in each complete cycle of the piston.

$$\begin{aligned} J_{\rightarrow} &= \frac{V_0\rho_1}{\mathcal{T}_v} = vA\rho_1, \;\; F_{\rm c} < F^M_{stall}, \\ J_{\leftarrow} &= \frac{V_0\rho_2}{\mathcal{T}_v} = vA\rho_2, \;\; F_{\rm c} > F^M_{stall}, \end{aligned} \tag{4.8}$$

being $J_{\rightarrow}$ and $J_{\leftarrow}$ the forward and backward flux of the turbine when the constant

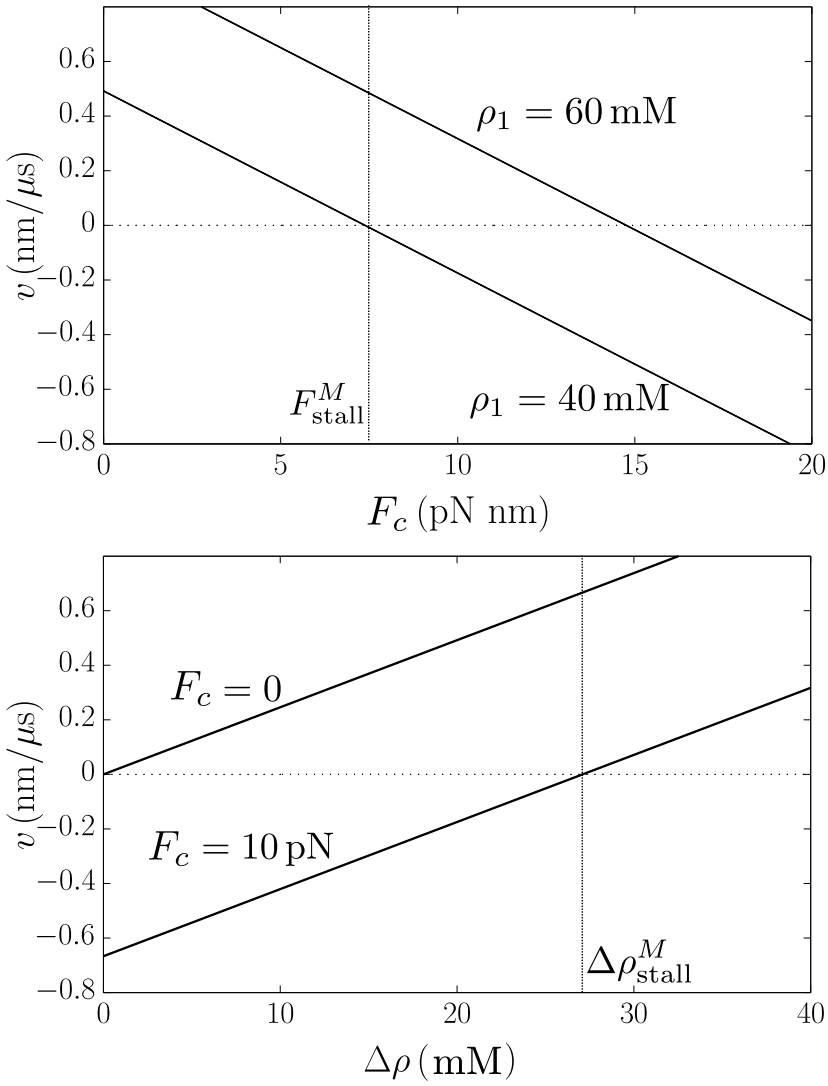

Figure 4.4: Velocity of the turbine. Top: Velocity versus external force opposing the natural motion for different values of ρ_1. The stall force necessary to stop the motion of the motor $F_{\mathrm{c}} = F_M^{\mathrm{stall}}$ is indicated for $\rho_1 = 40\mathrm{mM}$. Bottom: Velocity versus the density difference $\Delta\rho$. The stall gradient $\Delta\rho^M_{\mathrm{stall}}$ is indicated for the case $F_{\mathrm{c}} = 10$ pN. Parameters used are those of Table 4.2.

velocity v is positive or negative and $\mathcal{T}_v = D/v$ the Stoke's (deterministic) average duration of the cycle. However, due to the non–equivalence between backward and forward flux, the deterministic prediction (4.8) is not valid at the molecular scale where the introduction of the thermal fluctuations is mandatory. This becomes clear at the motor stall force F^M_{stall} situation where the average velocity is null ($v = 0$). In this situation, due to thermal noise, the piston is constantly fluctuating producing an equal number of complete cycles in the forward and the backward direction maintaing $v = 0$. Nevertheless, steps in the gradient direction transport more particles ($V_0\rho_1$) than steps in the opposite direction ($V_0\rho_2$) resulting in a net flux $J \neq 0$ in opposition to the deterministic prediction (4.8).

Thermal fluctuations can be introduced in the flux definition by taking into account that the average duration of each cycle $\mathcal{T}$ does not coincide with the deterministic description $\mathcal{T}_v = D/v$ but with the time that takes a stochastic trajectory of the motor to complete one step in either the gradient direction or in the opposite direction,

$$J = \frac{\langle \Delta N \rangle}{\mathcal{T}} = AD\frac{P_{\rightarrow}\rho_1 - P_{\leftarrow}\rho_2}{\mathcal{T}}, \tag{4.9}$$

where $P_{\rightarrow}$ and $P_{\leftarrow}$ are the probabilities of a successful step in the gradient direction or against it. For the transducing mechanism described, a step translocating particles requires the piston to advance a net distance $|\Delta x| = D$ (Fig. 4.5). If this distance is advanced in the forward direction $\Delta x = D$, an amount $V_0\rho_1$ particles will be translocated. However, if the distance is covered backwards $\Delta x = -D$ an amount of $V_0\rho_2$ particles will be translocated. This description is equivalent to a mean first passage time (MFPT) problem in which the piston starting at a position $x_0 = 0$ under a stochastic force $\overline{F} + \xi$ ends its trajectory when it reaches a position $x = \pm D$ (Fig. 4.5). The MFPT $\mathcal{T}(x_0)$ with x_0 as the starting position

of the piston follows the equation,

$$\frac{\overline{F}}{\gamma}\frac{d}{dx_0}\mathcal{T}(x_0) + \frac{k_B T}{\gamma}\frac{d^2}{dx_0^2}\mathcal{T}(x_0) = -1, \tag{4.10}$$

which can be derived from the Focker–Planck equation with absorbing boundary conditions at $x = \pm D$ corresponding to the Langevin equation describing the dynamics of the motor (4.3) [22]. The absorbing boundary conditions necessary to solve (4.10) can be written in terms of $\mathcal{T}(x_0)$ indicating that the mean step time for a cycle starting at a turbine end is zero,

$$\mathcal{T}(D) = 0, \quad \mathcal{T}(-D) = 0. \tag{4.11}$$

The solution of (4.10) evaluated in the starting point of a cycle ($x_0 = 0$) returns the average cycle time

$$\mathcal{T} \equiv \mathcal{T}(0) = \frac{\gamma D}{\overline{F}}\left(\frac{\cosh\frac{\overline{F}D}{\mathrm{k_B}T} - 1}{\sinh\frac{\overline{F}D}{\mathrm{k_B}T}}\right). \tag{4.12}$$

Equivalently, from the Fokker–Planck equation corresponding to (4.3) the probability of ending the step in the gradient direction $P_{\rightarrow}(x_0)$ starting the step at a position x_0 can be obtained,

$$\frac{\overline{F}}{\gamma}\frac{d}{dx_0}P_{\rightarrow}(x_0) + \frac{k_B T}{\gamma}\frac{d^2}{dx_0^2}P_{\rightarrow}(x_0) = 0. \tag{4.13}$$

With boundary conditions,

$$P_{\rightarrow}(-D) = 0, \quad P_{\rightarrow}(D) = 1. \tag{4.14}$$

Boundaries (4.14) state that the probability of a successful step in the gradient direction starting at the gradient end of the turbine $x_0 = D$ is one, and the probability of ending the step in the gradient direction starting the cycle in the end of the turbine opposite to the gradient direction $x_0 = -D$ is null. The solution for $P_{\rightarrow}$ starting at point $x_0 = 0$ returns the probabilities needed in eq.

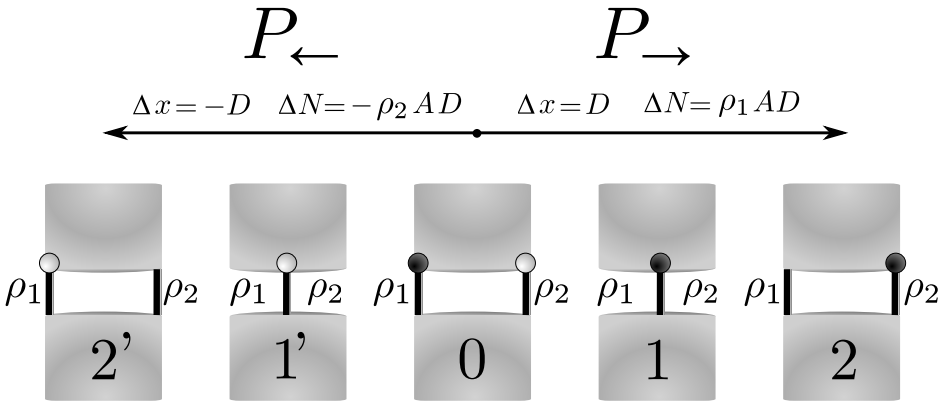

Figure 4.5: Scheme indicating one complete step of the piston. It starts at $x_0 = 0$ (0) and follows a stochastic trajectory that can achieve intermediate positions (1,1') but does not end until a net advance $\Delta x = D$ or $\Delta x = -D$ is achieved (2,2'). The probabilities probabilities $P_{\rightarrow}$ and $P_{\leftarrow}$ to finish the step in each direction are different and will depend on the net force and the diffusion of the piston. Additionally, the step in each direction carries a different quantity of particles ΔN. The initial position $x_0 = 0$ corresponds with the situation in which the piston exits one side of the machine and another piston enters from the opposite side. Each piston from the initial position (0) is marked with a circle (white or black) to facilitate its tracking along the scheme.

(4.9),

$$P_{\rightarrow} \equiv P_{\rightarrow}(x_0 = 0) = \frac{e^{\frac{\overline{F}D}{k_B T}} - 1}{2\sinh\frac{\overline{F}D}{k_B T}}, \quad P_{\leftarrow} = \frac{1 - e^{\frac{-\overline{F}D}{k_B T}}}{2\sinh\frac{\overline{F}D}{k_B T}}. \tag{4.15}$$

Where the probability $P_{\leftarrow}$ is obtained following the same prescription or using the normalization property $P_{\rightarrow} + P_{\leftarrow} = 1$. Introducing (4.15) and (4.12) in (4.9) an explicit expression for the flux is procured,

$$J = \frac{\overline{F}A}{2\gamma} \frac{\rho_1 \left(e^{\overline{F}D/k_B T} - 1\right) - \rho_2 \left(1 - e^{-\overline{F}D/k_B T}\right)}{\cosh(\overline{F}D/k_B T) - 1}, \tag{4.16}$$

able to reproduce the flux of particles in a thermal bath (Fig. 4.6). The further the external force is from the net stall force, the better is the match between the deterministic prediction of the flux (4.9) and the stochastic one (4.16). This is so, because for a large driving force the relative number of cycles against the motion direction is reduced. This leakage of ions at the motor stall force situation implies that a greater force than the stall force is needed to reverse the flux of ions. This force will be referred hereon as the pump stall force. This new stall force can be obtained from (4.16) at $J = 0$,

$$F^P_{\text{stall}} \equiv F_E(J = 0) = F^M_{\text{stall}} + \frac{k_B T}{D} \ln\frac{\rho_1}{\rho_2}, \tag{4.17}$$

which fulfills the relation $F^P_{\text{stall}} > F^M_{\text{stall}}$. The new term coincides with the force required to move a particle a distance D doing a work equivalent to the chemical free energy of the particle crossing the membrane $\Delta g = k_B T \ln\frac{\rho_1}{\rho_2}$.

Since the effect is thermal, expression (4.16) coincides with (4.9) in the low temperature limit ($T \to 0$) where thermal fluctuations disappear. The same occurs, for expression (4.17) where for $T \to 0$ the motor stall force and the pump stall force converge.

The same argumentation holds fixing F_{c} and varying the particle gradient to stall the flux. In this case, the pump stall gradient $\Delta\rho^P_{\text{stall}}$ obtained from (4.16)

has not a simple expression and has to be calculated numerically (Fig. 4.6).

The appearance of two different stall forces for the flux and the velocity entail three different energetic regimes of the transducer (Fig. 4.7). For external forces under $F^M_{\rm stall}$ ($v > 0$ and $J > 0$) the transducer works as a motor in which the force $F_{\rm c}$ opposes the motion of piston extracting work from it. In this situation the energy source is the depletion of particles in the gradient direction. On the other hand, for forces greater than the stall force of the pump $F^P_{\rm stall}$ ($v < 0$ and $J < 0$) the force is used to pump particles against the gradient. Here the energy source is the external force.

Finally, a third regime occurs where no useful energy can be obtained. This regime occurs between the two stall forces ($F^P_{\rm stall} < F_{\rm c} < F^M_{\rm stall}$). In this regime, there is not useful output energy neither as work, since the v and $F_{\rm c}$ have the same direction; nor as a chemical potential through particle pumping, since the flux follows the direction of the gradient (Fig. 4.7). In this regime not only there is no energy output but also there is a constant loss of energy through the non–zero flux. For this reason, this region is referred hereon as the leakage regime. The width of the leakage zone for biological parameters is large enough (~ 1 pN) to be of relevance in the performance of molecular motors. In fact, the width of the leakage regime depends on the free energy of a particle crossing the membrane (4.17), revealing again the thermal nature of the process that would disappear in the limit $T \to 0$.

During the motor regime, the energy extracted through the force $F_{\rm c}$ entails a power

$$P_M = F_{\rm c} v = \frac{(\rho_1 - \rho_2) A k_B T - F_{\rm c}}{\gamma} F_{\rm c}, \quad F_{\rm c} < F^M_{\rm stall}, \tag{4.18}$$

which exhibits the well known parabola with a maximum power at $F_{\rm c}(max) = F^M_{\rm stall}/2$ as it is seen in Fig. 4.8.

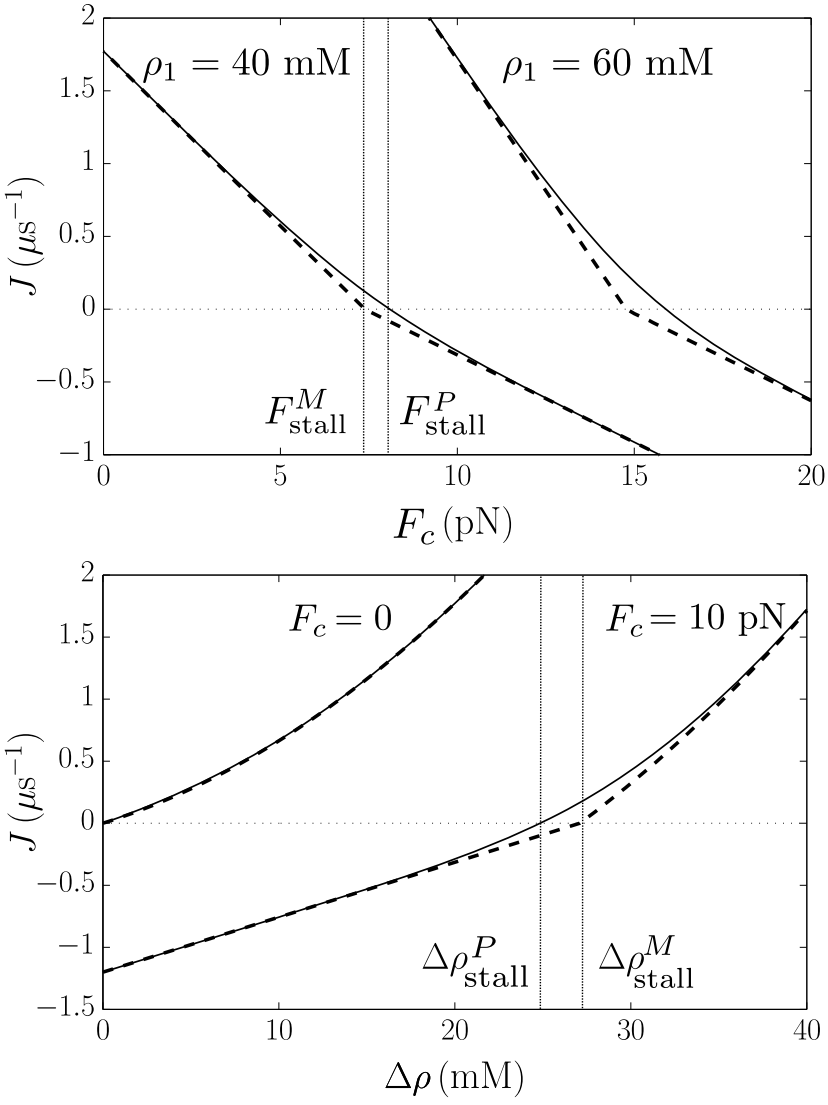

Figure 4.6: Flux of particles of the piston turbine against a conservative external force (Top) and the particle concentration difference (Bottom). The stochastic results (*solid line*) differ from the deterministic prediction (*dashed line*) near the motor stall force $F^M_{\rm stall}$. Parameters used are those of Table 4.2.

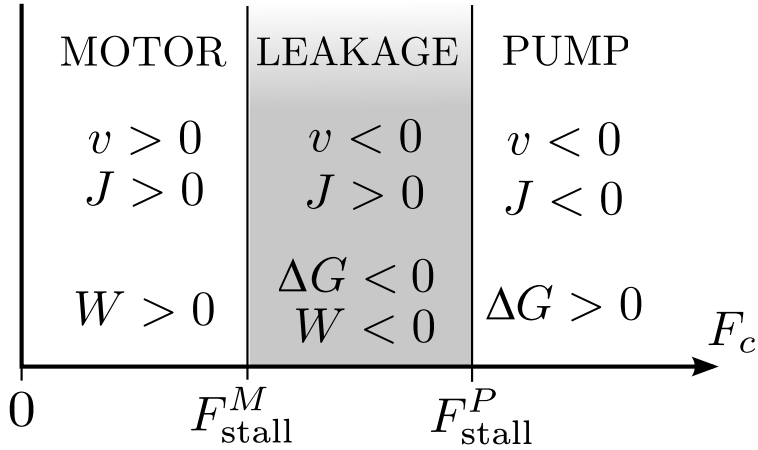

Figure 4.7: The turbine has three different regimes depending on the external force applied. In the motor regime the energy is extracted in form of work ($W > 0$) while in the pump regime, the energy is stored as an increment in the particle density difference ($\Delta G > 0$). In the leakage zone (*gray zone*), no useful energy can be obtained.

On the contrary, the pump power is the variation per unit of time of the gain in free energy in the reservoirs. This is the free energy of a particle passing between both reservoirs times the flux of particles,

$$P_J = |J|\Delta g = -Jk_BT \ln \frac{\rho_1}{\rho_2}, \quad F_{\text{c}} > F^P_{\text{stall}}. \tag{4.19}$$

The relation of the power with the external force is obtained introducing (4.16) into (4.19) procuring an increasing function of the power with F_{c}. This is so because the greater is the external force the greater is the flux of particles (Fig. 4.8).

While the motor power depends on the average velocity (4.18), the pump power depends on the particle flux (4.19). These dependences make the deterministic prediction correct when describing the motor power but not for the pump power that requires the understanding of the effect of thermal fluctuations. Ad-

ditionally, since no useful energy can be obtained in the leakage zone, no output power can be defined in this zone.

The leakage of ions is even more important for the efficiency. For the motor regime, the efficiency is

$$\eta_M = \frac{P_M}{P_J} = \frac{vF_c}{J\Delta g}, \quad F_c < F^M_{\text{stall}}. \tag{4.20}$$

In the Stoke's prediction, the efficiency reaches its maximum at the stall force. In this situation the motor achieves the transduction with a minimum dissipation. However, the results of the stochastic analysis returns a completely different scenario. For forces near the leakage zone, η_M presents a complete deviation from the deterministic prediction (4.8) decaying dramatically to zero (Fig. 4.8). Near the stall force, the output efficiency is low because the low velocity of the motor is decompensated by the continuous wasting of energy through the leakage. This decaying entails the arising of a new efficiency maximum for intermediate values of the external force. Nevertheless, the position of the maximum efficiency does not coincide with the point of maximum power which have implications in the effective energy transduction of these kind of motors since there is not an optimum regime with a maximum efficiency and maximum power.

Moreover, the deterministic efficiency is always greater than the stochastic one. However, the deterministic efficiency itself never achieves a maximum efficiency of $\eta = 1$ at the stall force F^M_{stall} because the finite difference in concentrations keeps this state far from thermodynamic equilibrium.

Similar results are obtained for the pump regime where the role of the powers is reverted. The input power will be the mechanical power and the output power is the chemical one,

$$\eta_P = \frac{P_J}{P_M} = \frac{J\Delta g}{vF_c}, \quad F_c > F^P_{\text{stall}}. \tag{4.21}$$

Again, the resulting efficiency is null at the stall force and reaches a maximum

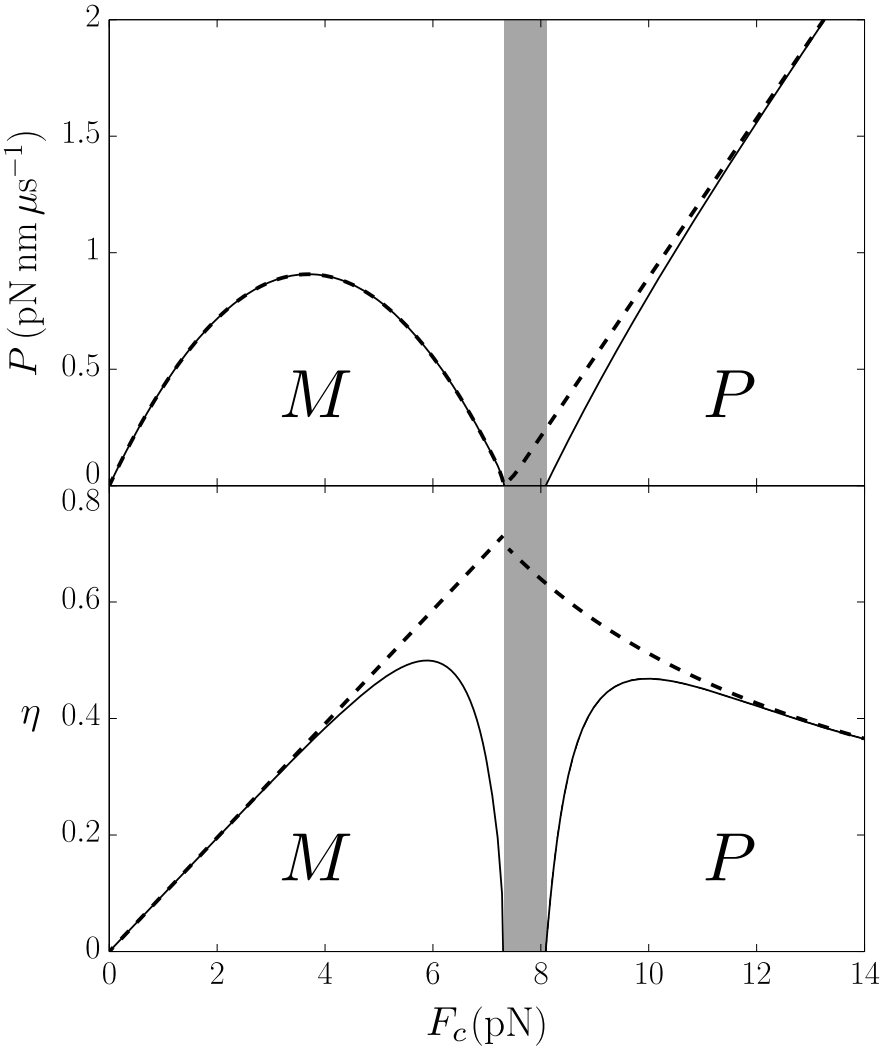

Figure 4.8: Turbine power and efficiency versus external force. Motor regime is at the left side and pump regime at the right one. The shaded zone corresponds with the force gap where power and efficiency are null. The deterministic power and efficiency (*dashed line*) is always greater than the stochastic one (*solid line*) specially near the leakage zone. Concentration $\rho_1 = 40\,\mathrm{mM}$, other parameters used are those of Table 4.2.

for an average force far from the stall force. For larger forces, the deterministic result is recovered saturating at $\eta_P(F_c \to \infty) \sim A\rho_2/F_c$ (Fig. 4.8). Thus, in the whole working scheme of the turbine the single efficiency optimum point at the stall force is replaced by two new efficiency maxima, one for the motor regime and another one for the pump regime. This result is of special interest for biological motors that have evolved along time to perform optimally taking into account the stochastic dynamics inherent to the biomolecular scale.

The same description is obtained studying the dependence of the power and the efficiency with the particle gradient $\Delta\rho$ (Fig. 4.9). In this description the roles are exchanged, having the power parabola for the pump regime and the increasing power for the motor regime. This is only a signature of the opposition of the particle force F_p increasing with $\Delta\rho$ and the external force F_c.

This description of a turbine is ideal in the sense that is not treating properly the stochastic dynamics of individual particles. In addition, it does not consider other relevant effects in real turbines such as a membrane potential, the internal structure of the channel or the interaction between particles. In the following section, the ionic turbine model is improved to deal more realistically with diffusive particles. Finally, in the last section, a theoretical framework taking into account the individual particles is developed with the corresponding numeric modelling.

4.2.2. Turbine with multiple vanes

The turbine described with one piston results in interesting results but fails to take into account correctly the diffusive nature of the particles. While the model requires a full advance $\Delta x = \pm D$ to produce a complete step, this assumption does not take into account that fluctuations of the piston around one of the ends

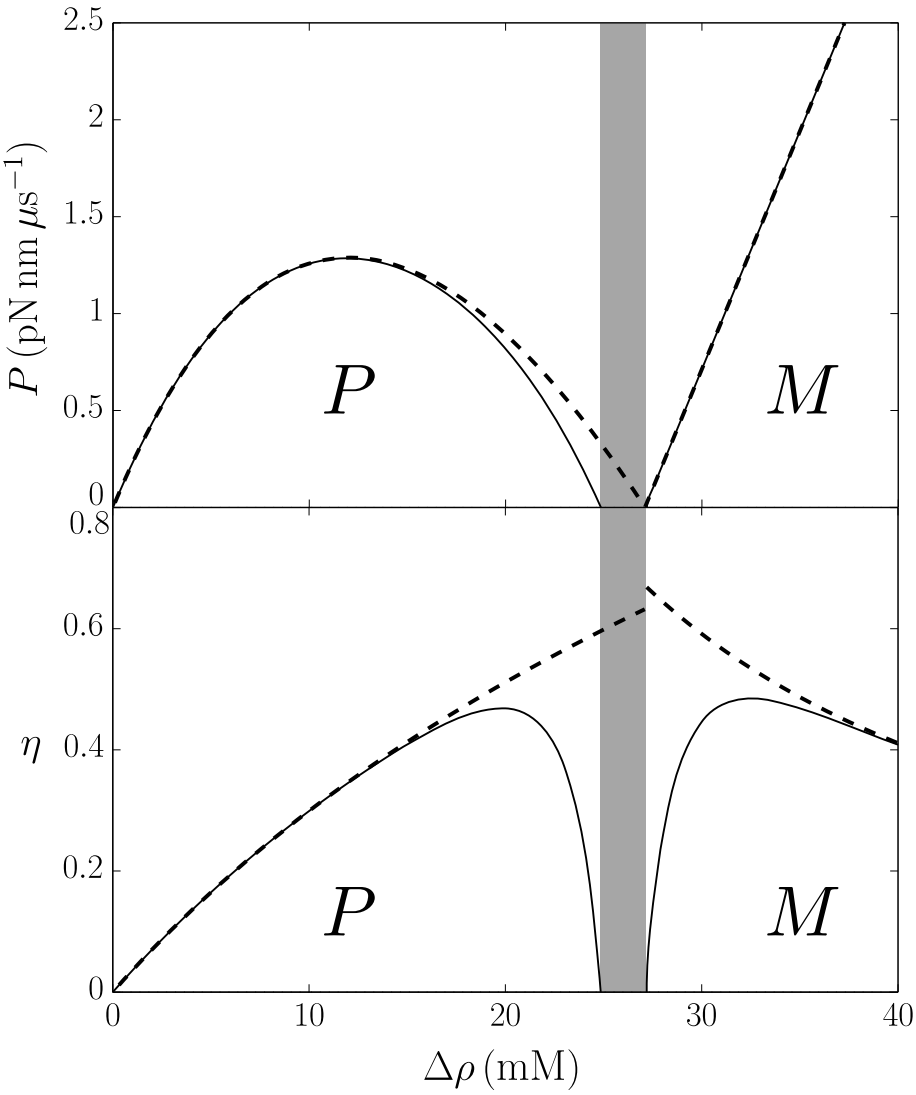

Figure 4.9: Turbine power (top) and efficiency (bottom) versus particle gradient. The behavior is equivalent to the energetic performance agains F_c but with the behavior of Motor and Pump exchanged. Concentration $\rho_1 = 40\,\mathrm{mM}$, other parameters used are those of Table 4.2.

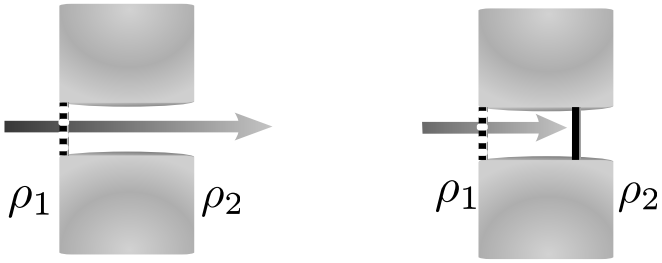

Figure 4.10: Comparison of the performance of the one–piston turbine (*left*) and the multiple-vane turbine (*right*) when a vane arrives at one end of the channel (*dashed vane*). In the one–piston turbine, fluctuations of the piston around one end can translocate particles. On the contrary, for the multiple-vane turbine there is always an active piston inside the turbine hindering the free flux of particles.

of the turbine would lead to a particle leakage *i.e.* the translocaction of particles does not require a full step of a determined length to translocate particles. This problem is easily avoidable by introducing more pistons in the turbine. With a set of equidistant pistons, the volume of particles requires to be enclosed by the pistons to be translocated (Fig. 4.11) and therefore a minimum finite advance of the turbine is necessary to produce a translocation (Fig. 4.10). Actually, this solution is not used only by microscopic motors but also by its macroscopic counterpart which translocate a certain fluid with several vanes. For this reason the pistons will be referred hereon as *vanes* to differentiate this turbine from the one–piston case.

The intervane distance $d < D$ determines the number of vanes inside the channel and interacting with the particles at the same time. In order to avoid the additional leakage aforementioned is enough to consider a minimum of two vanes acting at the same time $\frac{D}{2} < d < D$. In this case, the cycle is completed when the turbine covers a distance equal to the intervane distance $\Delta x = \pm d$ (Fig.

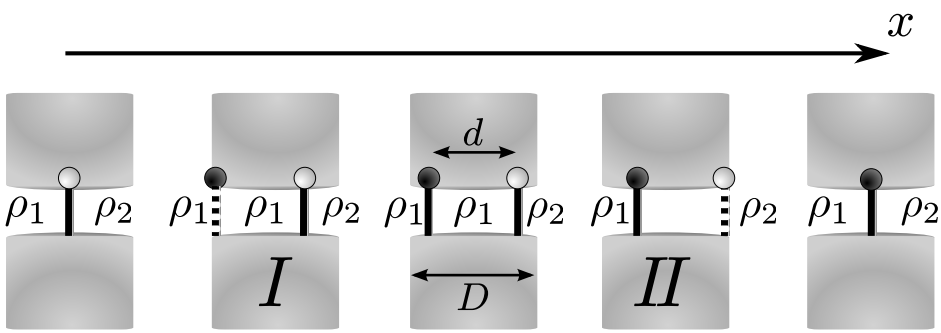

Figure 4.11: Turbine with two vanes along one full cycle advancing in the gradient direction ($\Delta x = d$). The particles are shut in the turbine when the second vane (*marked with a black ball*) enters the turbine (I) and are released to the other reservoir when the initial vane (*marked with a white ball*) leaves the turbine (II). Vanes entering and leaving the system are depicted as dashed vanes.

4.11). Thus, the turbine with multiple vanes translocates each step a volume of particles proportional to the inter–vane distance $V_0 = Ad$.

The net force $\overline{F}$ is not affected by the increase in the number of vanes and therefore the average velocity (4.5) is not affected by this change. Nonetheless, the translocation of particles does change with the number of vanes. Consequently, the particle flux must be reformulated. The multiple vane description introduces two relevant configurations of the turbine to describe the flux of particles. These are the configurations in which a vane is situated at either end of the turbine and will be labelled hereon as I and II (Fig. 4.11). At these configurations a vane can enter the turbine enclosing a certain volume of particles, or can disappear releasing a certain amount of particles. In configuration I, the turbine exchanges freely particles with the reservoir of concentration ρ_1, while configuration II exchanges particles with the reservoir of concentration ρ_2.

Taking I as the starting configuration, it can achieve configuration II by two different ways: forwards or backwards (Fig. 4.12). While in the forward direction

there is a net translocation of particles, in the backward direction no particle is translocated. These two transitions are labelled as $\overrightarrow{I\,II}$ and $\overleftarrow{II\,I}$. Taking II as the starting configuration, the behaviour is similar, having a net translocation of particles when the turbine goes to I backwards $\overleftarrow{I\,II}$ and no net flux of particles when advancing $\overrightarrow{II\,I}$. The four possible transitions are summarised in Figure 4.12 with the corresponding displacement of the turbine, and the corresponding particle exchange.

A cycle starting in position I will not translocate any particle until it arrives, at least, at a configuration II. Once in II, again no translocation will take place, at least, until it arrives again at I, closing the motor cycle. Thus a cycle is composed by the succession $I - II - I$. After the cycle is completed, the turbine may have advanced a distance d ($\overrightarrow{I\,II} + \overrightarrow{II\,I}$), a distance $-d$ ($\overleftarrow{II\,I} + \overleftarrow{I\,II}$) or no net advance ($\overrightarrow{I\,II} + \overleftarrow{I\,II}$ or $\overleftarrow{II\,I} + \overrightarrow{II\,I}$), entailing also different amounts of particles translocated ΔN. Once the cycle finishes in the I configuration, the system retains no information on the previous trajectory, *i.e.* the cycle is Markovian and therefore the average temporal evolution through a long trajectory can be studied through the average of the possible ways to perform a single cycle $I - II - I$.

The average number of particle translocated in the process $I - II$ will depend on the probability to produce the transition forwards or backwards,

$$\langle \Delta N_{I-II} \rangle = P_{\overrightarrow{I\,II}} \Delta N_{\overrightarrow{I\,II}} + P_{\overleftarrow{II\,I}} \Delta N_{\overleftarrow{II\,I}} = P_{\overrightarrow{I\,II}} \rho_1 V_0. \tag{4.22}$$

Where the relation $\Delta N_{\overleftarrow{II\,I}} = 0$ has been used leaving only one unknown quantity, the probability of starting at position I advance forward to position II ($P_{\overrightarrow{I\,II}}$) instead of going backwards. This problem is equivalent to the MFPT problem solved in the previous section but in an asymmetric fashion. In this case, the absorbing barriers are placed at a different distance from the starting position. For instance, the case of the first transition starting at a configuration I is equivalent to have a particle under a Brownian force $\overline{F} + \xi$ that ends its trajectory when it

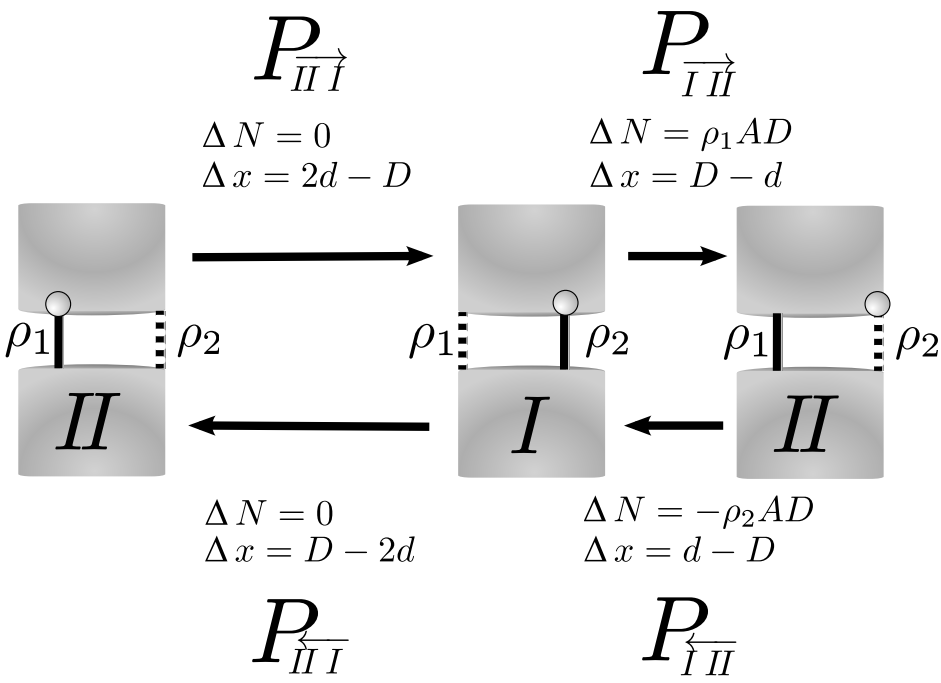

Figure 4.12: There are four possible transitions between states I and II. Each transition entails a different advance Δx and different average amounts of translocated particles ΔN. Starting at each state, there are two transitions possible with different probabilities for each direction $P_{\rightarrow}$ and $P_{\leftarrow}$. The active vane in state I is marked with a white ball for the sake of clarity along the different transitions. Vanes entering and leaving the channel are marked as a discontinuous vane.

reaches the boundaries set by state II, $\Delta x = -(2d - D)$ or $\Delta x = D - d$. Thus, the resulting MFPT and exit probability follow equations (4.10) and (4.13) with boundary conditions,

$$\mathcal{T}_{I-II}(D-d) = 0, \qquad \mathcal{T}_{I-II}(D-2d) = 0, \tag{4.23}$$

$$p_{\overrightarrow{I\,II}}(D-d) = 1, \qquad p_{\overrightarrow{I\,II}}(D-2d) = 0. \tag{4.24}$$

returning,

$$P_{\overrightarrow{I\,II}} \equiv \quad p_{\overrightarrow{I\,II}}(0) = \quad \frac{\mathrm{e}^{\nu_1} - \mathrm{e}^{-\nu_2}}{2\,\mathrm{sh}\,\nu_1}, \tag{4.25}$$

$$\mathcal{T}_{I-II} \equiv \quad \mathcal{T}_{I-II}(0) = \quad \frac{\gamma d}{2\bar{F}}\left(\frac{\mathrm{ch}\,\nu_1 - \mathrm{e}^{\nu_2}}{\mathrm{sh}\,\nu_1} - \frac{3}{2} - \frac{D}{d}\right), \tag{4.26}$$

with,

$$\nu_1 = \frac{\overline{F}d}{2kT} \quad , \qquad \nu_2 = \frac{\overline{F}}{kT}\left(\frac{3d}{2} - D\right). \tag{4.27}$$

Proceeding in the same way for the second transition (from II to I), the average number of particles, the direction probability and the time of the process follow the relations,

$$\langle \Delta N_{II-I} \rangle = P_{\overrightarrow{II\,I}} \Delta N_{\overrightarrow{II\,I}} + P_{\overleftarrow{I\,II}} \Delta N_{\overleftarrow{I\,II}} = -P_{\overleftarrow{I\,II}} \rho_2 V_0, \tag{4.28}$$

$$P_{\overleftarrow{I\,II}} = \frac{-\mathrm{e}^{-\nu_1} + \mathrm{e}^{\nu_2}}{2\,\mathrm{sh}\,\nu_1}, \tag{4.29}$$

$$\langle \mathcal{T}_{II-I} \rangle = \frac{\gamma d}{2\bar{F}}\left(\frac{\mathrm{ch}\,\nu_1 - \mathrm{e}^{-\nu_2}}{\mathrm{sh}\,\nu_1} + \frac{3}{2} + \frac{D}{d}\right). \tag{4.30}$$

Finally, the average flux can be computed using this information to evaluate the average flux of a cycle, this is, the average number of particles translocated in a cycle $\langle \Delta N \rangle_{\mathcal{T}}$ over the average time that takes a full cycle $\mathcal{T}$,

$$\begin{aligned} J &= \frac{\langle \Delta N \rangle_{\mathcal{T}}}{\mathcal{T}} = \frac{\langle \Delta N_{I-II} \rangle + \langle \Delta N_{II-I} \rangle}{\langle \mathcal{T}_{I-II} \rangle + \langle \mathcal{T}_{II-I} \rangle} = \\ &= \frac{\overline{F}A}{2\gamma} \frac{\rho_1\left(\mathrm{e}^{\nu_1} - \mathrm{e}^{-\nu_2}\right) + \rho_2\left(\mathrm{e}^{-\nu_1} - \mathrm{e}^{\nu_2}\right)}{\mathrm{ch}\,\nu_1 - \mathrm{ch}\,\nu_2}. \end{aligned} \tag{4.31}$$

Which returns a behaviour similar to the one–piston turbine. Again, the flux is inverted at a pump stall force value F^P_{stall} larger than F^M_{stall} (Fig. 4.13) giving place to the leakage zone,

$$F_{\text{c}}(J=0) \equiv F^P_{\text{stall}} = F^M_{\text{stall}} + \frac{k_B T}{D-d} \ln \frac{\rho_1}{\rho_2}. \tag{4.32}$$

In this case the difference between both stall forces is greater than the predicted for the one–piston case (4.17) (Fig. 4.13). Here, the size for he leakage zone coincides with the free energy of a particle crossing the membrane used along a distance $D - d$. Additionally, expressions (4.31) and (4.32) point out the failure of the one–piston turbine. Note that the one–piston scenario is not recovered in the limit $d = D$. The one–piston turbine analysis is an idealization in which always a full step of length D is required to obtain particle transduction. Instead, the flux diverges in this situation (Fig. 4.14).

Since the flux has the same characteristics as the one–piston case, the resulting profiles for the power and the efficiency show the same properties, namely, the decay to zero of the efficiency near the leakage zone and the appearance of new efficiency maxima (Fig. 4.13). The resulting efficiency is lower than the one predicted by the one–piston model. This does not imply that the multiple–vane model has a worse performance, but a more realistic one. In fact, when the limit $d = D$ is performed properly, it leads to an infinite flux of particles (Fig. 4.14) with a continuous loss of energy in the system *i.e.* null power and null efficiency.

4.2.3. Particle dynamics

So far, the particles have been considered as a continuous bulk with instantaneous diffusion. However, in real systems particles are discrete entities each one with its own dynamic. Therefore, it is essential to study the problem with a

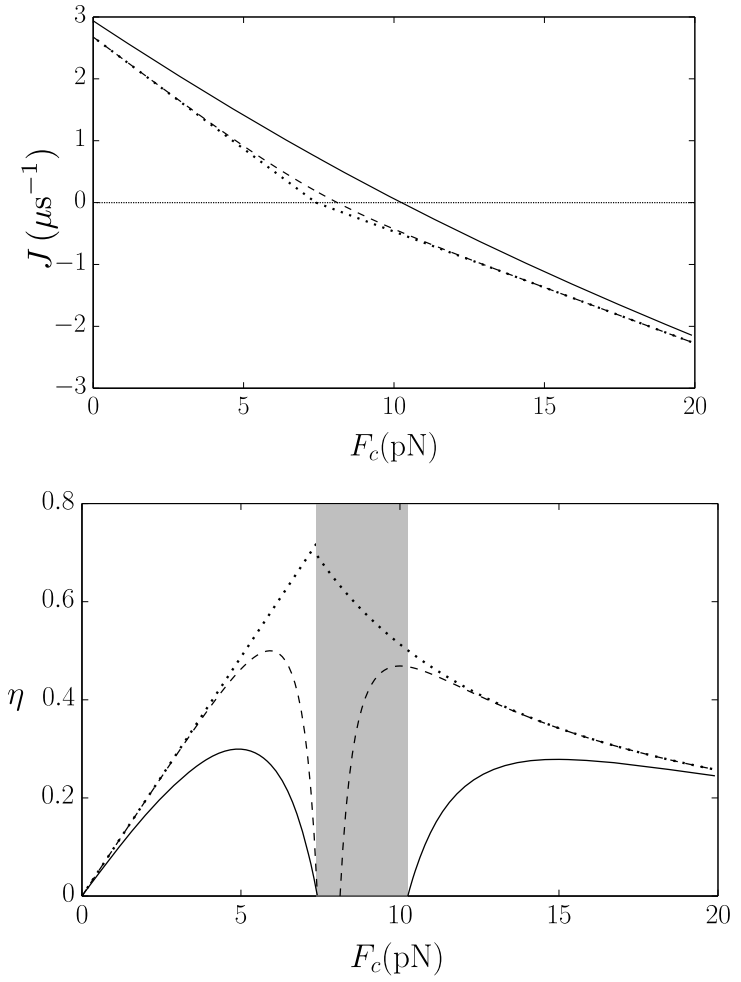

Figure 4.13: Comparison between the performance against an external force for the two–vane turbine (*solid line*) (4.31), the one–piston turbine (*dashed line*) (4.16) and the deterministic Stoke's analysis (*dotted line*) (4.8). Top: Particle flux of each model. Bottom: Efficiency of each model. The leakage zone of the two–vane turbine (*shaded zone*) is larger than the expected for the one–piston turbine. An intervane distance $d = 3$ nm is used, the rest of the parameters are those of Table 4.2.

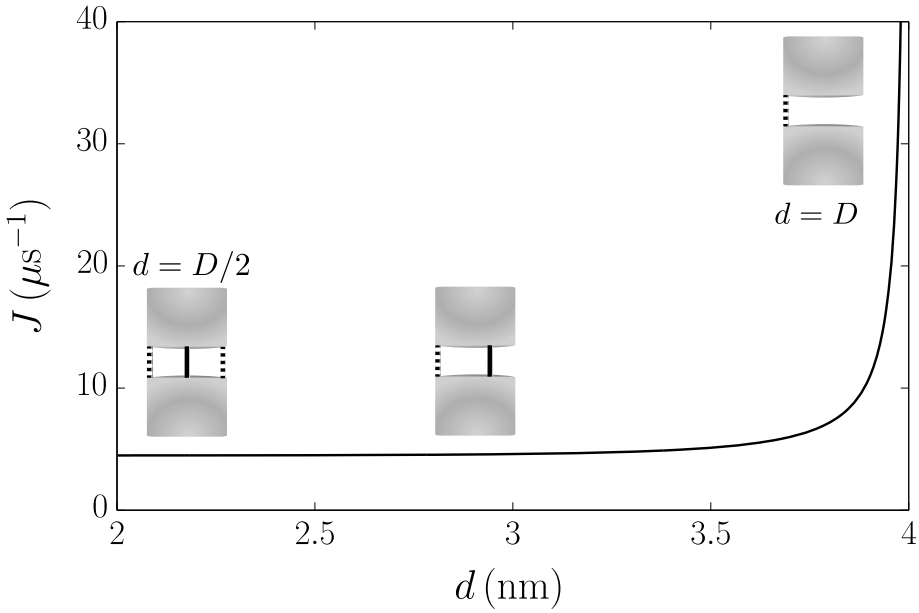

Figure 4.14: Dependence of the flux of two–vane turbine with the intervane distance d. The flux is constant for low values of d but diverges near the limit $d = D$. The three diagrams show the vane configuration when a vane is entering/leaving the channel for three different situations: The one–piston limit $d = D$, the shortest d compatible with the two–vane turbine $d = D/2$, and an intermediate d as the one used in Fig. 4.13. An external force $F_c = 5\,\mathrm{pN}$ is used, the rest of the parameters are those of Table 4.2.

finite number of particles to confirm the validity of the results obtained in previous sections. In addition, new phenomenology that was not taken into account previously will arise from this analysis. For instance, a large driving external force acting on the turbine, may achieve a great velocity but without producing any flux since the particles have no time to enter the turbine. This situation introduces a new limit, the volume of particles translocated per cycle is not anymore $V_0 = Ad$ but a lower value. For the sake of fluency, computational details are gathered in Appendix B leaving here the setting out of the problem and the main resulting observables.

In order to describe the dynamics of the ions, they must be considered separately from the thermalised cytosol and studied as thermalised particles by their own. Hence, the description of the dynamics of the turbine with N particles takes $N + 1$ coupled Langevin equations,

$$\left.\begin{array}{rcl} \gamma\dot{X} & = & -\sum_i V_p'(x_i - X) + V_T'(X) - F_{\rm c} + \xi \quad , \\ \gamma_p\dot{x}_i & = & \sum_i V_p'(x_i - X) + V_\phi'(x_i) + \xi_p \quad i = 1 \cdots N. \end{array}\right\} \tag{4.33}$$

Where X is the position of the piston and x_i is the position of each particle. The piston follows the same Brownian dynamics described in (4.3), whereas each particle follows also overdamped dynamics with friction coefficient γ_p and a white noise thermal force with correlation $\langle \xi_i(t)\xi_j(t')\rangle = 2\gamma_p kT\delta_{ij}\delta(t-t')$.
Additionally, a full mechano–chemical description requires to take into account all the rest of interactions present in a real molecular motor. Considering this, three potentials have been added in the system description (4.33). On one hand the interaction potential V_p that controls the collisions between the particles and the piston producing the particle force $F_p = \langle V_p'(x_i - X)\rangle$ already introduced in its average ideal form. This potential can be described through a hardcore poten-

Parameter	Value	Source
γ_p	$2{\cdot}10^{-3}$ pN nm μs	Stokes friction for a sphere of radius $\simeq$ 8 nm
d	3 nm	Chosen to have 1-2 active vanes
β	0.7	Intervane useful volume fraction

Table 4.3: Biophysical parameters used in the simulation with the corresponding source of the value. The rest of the parameters used in the simulations are gathered in Table 4.2 and Appendix B.

tial (Fig. 4.15). On the other hand, the potential $V_T(X)$ describes the internal interaction of the turbine. This potential may have many biological functions such as the control of the leakage by fixing the piston at the central part of the turbine not allowing the movement of the piston for low forces *i.e.* near the stall force. Finally, $V_\phi(x_i)$ is the membrane potential produced by an electrical potential difference at both sides of the membrane and generating a net force in the charged ions inside the turbine. If not stated otherwise, potentials V_T and V_ϕ will not be considered in the current work, having thus, the same mechanistic situation described in (4.3). Other terms can also be added to the equations such as particle–particle interaction. However, ionic density in biological systems is low enough to consider, in a first approximation, that there is no interaction between particles. Additionally, this is the case of the BFM where particles pushing the rotor can be found in different stators. The relevant biophysical parameters chosen for the current analysis are again based in biological information. Thus, for this analysis, the parameters of Table 4.2 are kept while the new parameters are gathered in Table 4.3. Additionally, the rest of parameters necessary for the computational analysis can be found in Table B.1.

Langevin equations describing the particle–turbine dynamics (4.33) can be

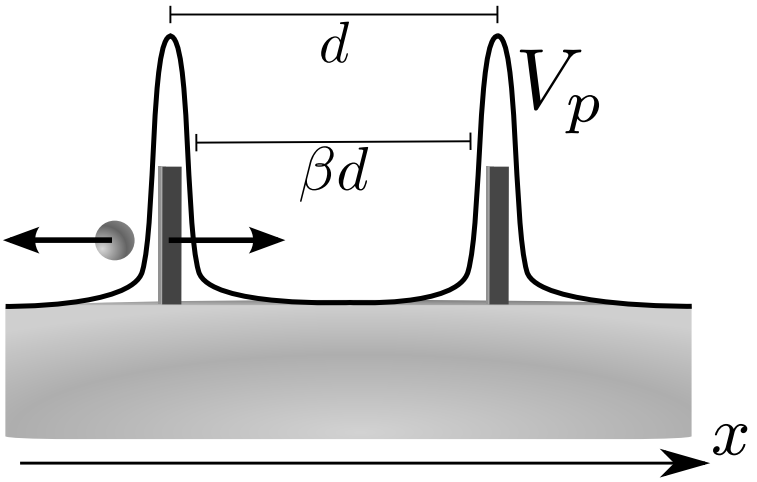

Figure 4.15: Example of interaction potential between the particles and the turbine V_p. The effective volume between vanes is reduced because of the potential width by a factor β.

integrated numerically obtaining trajectories for the turbine and the particles from which information about the velocity, flux and energetics of the motor is available (Appendix B). The average resulting velocity shows a behaviour comparable with the analytical results (Fig. 4.16). In fact, the dynamics equations (4.33) coincide with the simplified Langevin equation (4.3) when the particles diffuse faster than the advance of the turbine, which is a good approximation to the biological scenario. Actually, even for large values of the velocities, with an external assisting force ($F_c < 0$), the motor returns values only slightly slower than the prediction.

The resulting values of the flux also match the values predicted analytically in the muliple–vane scenario but contemplating that the volume of particles that fit inside the two vanes depends on the actual expression for V_p. The interaction potential for each vane has a certain width, as it happens in real turbines, that

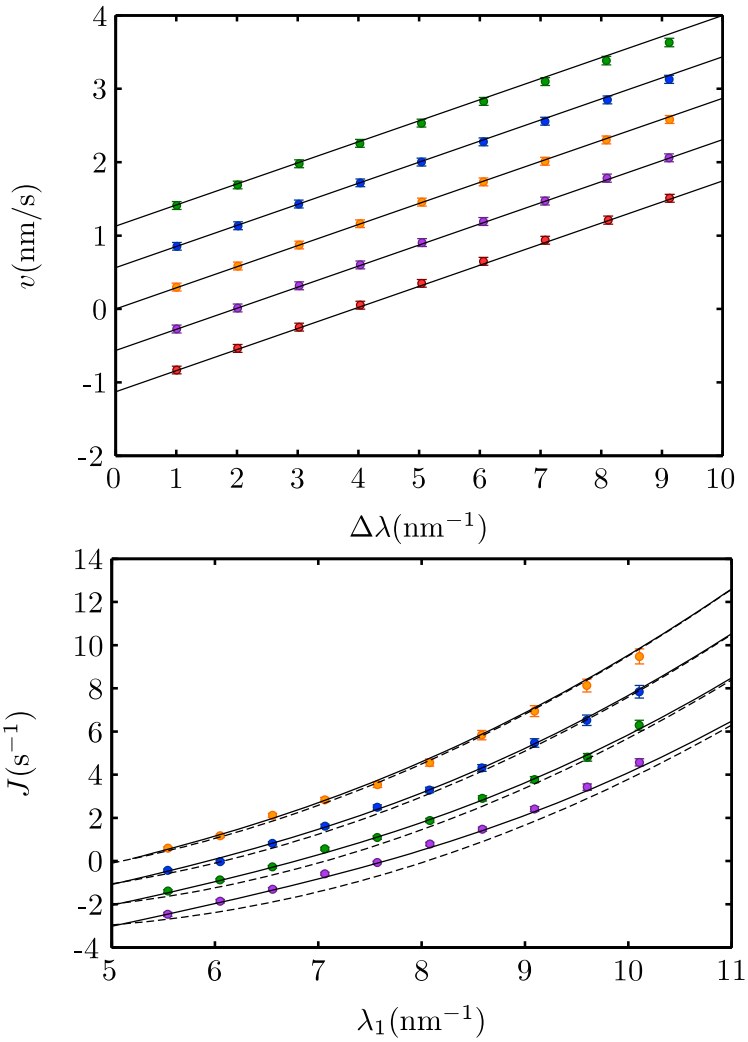

Figure 4.16: Results of the turbine simulations for different values of F_c (*symbols*) compared with analytical results (*solid line*) (eq. (4.31)) and Stoke's prediction (*dashed line*) (eqs. (4.5) and (4.8)). Top: Velocity of the turbine *vs.* lineal concentration of particles difference. Bottom: Flux of particles *vs.* lineal concentration of particles. The values used for F_c are -16 pN,-8 pN, 0 pN, 8 pN, 16 pN.

reduces the available volume translocated. The new volume will be $V_0 = \beta dA$ with $\beta < 1$ the available inter–vane volume fraction (Fig. 4.15). This fraction can be estimated for each potential and situation, which for the current case is $\beta = 0.7$ (Appendix B). The flux predicted this way fits very well with the stochastic simulations having some little discrepancies near the stall forces, where the diffusion velocity of the particles becomes more important (Fig. 4.16). This is so, since in the leakage zone, fluctuation of the turbine around state *I* and *II* is more frequent and the dynamics of charging and discharging of the turbine becomes more relevant.

The efficiency of the motor can also be computed showing a good match with the analytic model (Fig. 4.17). The computed efficiency recovers the decay of the efficiency near the stall forces of the device. This result entails that the analytic description is able to capture the energetic performance of the particle transduction device even near the leakage zone where discrepancies from the solution of the velocity and the flux can imply a large deviations.

To sum up, the computational results of the turbine not only allow to tackle the problems more realistically but do also confirm that the phenomenology described analytically from the initial one–piston turbine model is intrinsic to molecular turbines and can not be disregarded. The differences from the Stoke's analysis introducing thermal fluctuations is essential to study the energetic performance of the motor which is usually the experimental unavailable information of molecular machines.

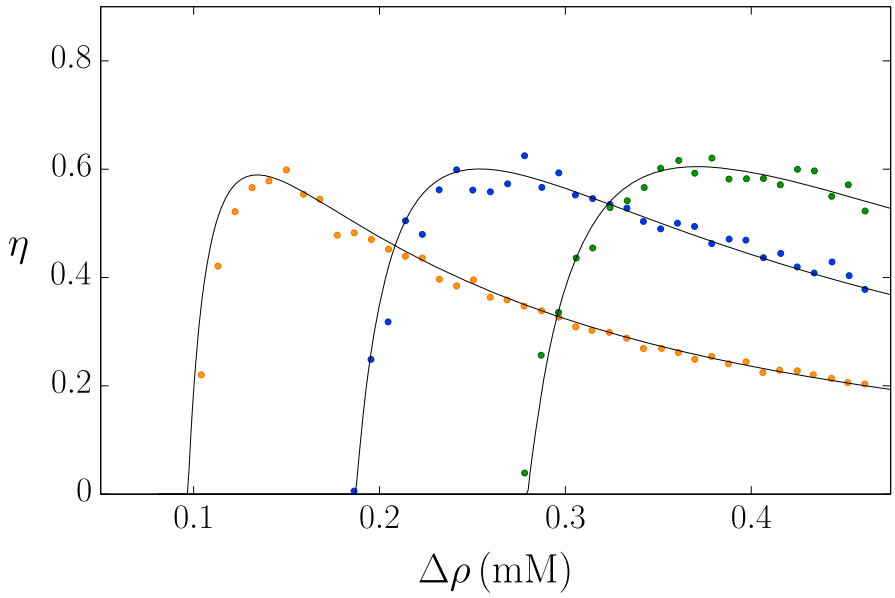

Figure 4.17: Efficiency of the turbine *vs.* de particle gradient for different values of F_c. The result from the simulations (*symbols*) match the efficiency resulting from the flux of the two–vane turbine (4.31). F_c = 4pN, 8 pN, 16 pN.

5 Conclusions

The current work has been devoted to the analysis of operation of rotatory molecular motors dealing with theoretical aspects of their energetic transduction. The analysis included both, more general approaches and more specific ones applied to particular motors. Here, a conclusion section is procured summarising the most relevant results and aspects of the work, with the corresponding publications.

Theoretical framework [57, 56, 70]

Molecular motors are macromolecules, which operate transforming between different kinds of energy. Such transduction results from the multiple complex interactions between the atoms composing each motor and its environment. The complexity of this picture is an obstacle in understanding the transduction process. Thus, in order to delve into the operation of molecular machines a more generic scenario is needed. However, possible theoretical descriptions of molecular motors are multiple. Each one corresponding with a different level of abstrac-

tion and contributing to the understanding of the machine operation. In the current work, the analysis developed takes as starting point the main observable of molecular machines, their trajectory under different experimental conditions. The analysis of the trajectory allows to identify the main processes composing each individual transduction cycle, characterising the length and duration of each process. This analysis separates, from the observed step-like trajectories, two well differentiated processes. On the one hand the mechanical times, during which the motor exerts a net force and produces a spatial advance; on the other hand, the dwell times, when the motor waits for different catalytic reactions and does not advance. In order to quantify these processes, the overdamped dynamics characteristic of the molecular working scale plus the kinetic of the reactions taking place are necessary. Thus, the analytic characterisation of the mechanical and chemical processes allowed to predict the dependence of the average velocity of the motor with the different experimental control parameters.

Additionally, a more detailed analysis of the motor was proposed through the explicit treatment of the dynamics of the machine. In this case an overdamped Langevin equation that takes into account the thermal stochastic forces acting continuously on the motor. The only ingredient missing in this analysis is the actual expression of the force that the motor is exerting, that can be written in the form of a motive potential. Thus, the problem is reduced to the search of this potential that contains all the mechano–chemistry of the motor.

F_1 motor under dissipative forces [56]

The theoretical framework proposed was applied for the F_1–ATPase motor. To start with, the analysis was based in a purely dissipative set up of the motor with two control parameters, the size of the dragging cargo and the ATP concentration. A deterministic analysis was carried out quantifying the mechano–

chemical processes relevant in the observed trajectory of the motor. This study gave place to a prediction of the velocity without any free parameter. The deterministic velocity profile calculated compared well with experimental observations of the rotation of the motor grasping the dependence of the velocity with the control parameters.

The appealing results suggested a detailed stochastic analysis of the motor. The motive potential derived from experimental observations consisted on a flashing mechanism between two sawtooth potentials. Each potential describing a chemical occupation state of the catalytic site of the motor, namely, occupied or free. Hence, the flashing between potentials corresponds with the caption of ATP and release of its hydrolysis products. Thus, the flashing times, that will be in general stochastic, will be driven by the chemical reactions and mechanical processes already described in the deterministic analysis. Hence, such a description, relates all the parameters of the flashing mechanism with real measurable quantities allowing to test the validity of the motive potential without any free parameter. In fact, the value of the substep angle α, which has been measured experimentally, can be extracted directly from the model from optimisation arguments of the motor operation. The resulting velocity profile from the corresponding Langevin equation returned a good match with the experimental data. In fact, it gave place to a better approximation than the one obtained from the deterministic analysis. Actually, the stochastic simulations predict a lower value than the deterministic results. An analysis revealed how the discrepancies are related with the stochasticity of the system *i.e.* flashing mechanism and thermal fluctuations. The differences come from the appearance of missing steps. Missing steps are ATP hydrolysis events that do not produce a successful step but waste the energy of the hydrolyzed ATP. The fraction of missing steps was also quantified analytically using the Fokker–Planck equation corresponding to the Langevin dynamics of the motor. The result is an explicit relation of the

fraction of missing events with the size of the load attached to the motor.

F_1 motor under conservative forces [57, 70]

The dependence of the F_1 motor with an external conservative torque was also studied. In this case, the analysis is more complex since a conservative torque affects the transduction cycle in both, chemical and mechanical processes. Specifically, the dependence of the duration of mechanical processes with the external force was found to have a contribution from thermal fluctuations. Again, this issue was tackled from the Fokker–Planck equation describing the spatial probability profile of the motor. Finally, with all the dependences with the external torque successfully quantified, the resulting velocity description was compared successfully with the velocity profile. As in previous analysis, the velocity prediction was performed without any free parameter giving soundness to the proposed potential.

Finding a potential compatible with available experimental information, not only gives an insight into the main mechanisms driving the operation of the motor but also allows to formulate predictions on the energetics of the motor, which can not be usually observed experimentally. This analysis was based in predictions of the power and the efficiency of the motor and compare them with the deterministic results. The study revealed dramatic differences between stochastic and deterministic results. While for the deterministic analysis, the maximum of efficiency is reached at the stall force of the motor, this is not longer true when thermal fluctuations are included. Thermal fluctuations lead the movement of the motor near the stall regime and the spatial advance, fixed by the motive potential, is erased. This way, the maximum of efficiency is obtained for intermediates

value of the external torque where the useful power of the motor is also large. This result is of special relevance for biological molecular motors, since they are expected to work in an optimum regime. In this case, this optimal behaviour can not be predicted by a pure deterministic analysis where thermal fluctuations are mandatory. Hence, this result does not only introduce a prediction for the efficiency but a proof that thermal fluctuations can not be neglected when dealing with the energetic transduction of molecular motors.

Fokker–Planck approximation to molecular motors [54, 55]

Due to the non–linearity of the flashing potential mechanism, the solution of the the Langevin equation is not analytically available. Therefore, the analysis of thermal fluctuations must be performed, in general, through computer simulations. This fact inspired an analytical procedure to analyse this kind of systems. The formulation consisted in an approximation of the Langevin equation through the Fokker–Planck description. This approximation takes into account the flashing mechanism as a dichotomous noise that can be approximated with a white noise. The resulting equation is a F–P equation with a diffusion coefficient dependent on the position. For sawtooth potentials, an exact solution of the resulting F–P equation is determined from which the velocity of the motor is available. This theoretical approximation was tested with experimental results of the F_1 motor. The match between theory and model was good for regimes of high ATP concentration and large loads. In order to evaluate the goodness of the approximation, a predictor was developed which is able to give the experimental conditions threshold beyond which the approximation holds. As a by

product, the analysis of this problem revealed that the traditional algorithms for the integration of Langevin equations in the Stratonovich interpretation failed to converge to the correct solution when the diffusion coefficient is not continuous in space. In order to solve this problem, a new algorithm based in the meaning of the Stratonovich interpretation was developed able to converge to the correct solution even in this case.

Molecular Machines driven by an ionic flux [58]

Finally, the developed theoretical framework was applied to molecular motors driven by a flux of ions. These motors presented new challenges originated in the change of the transduction mechanism. Now a flux of ions is coupled with the mechanical motion of an tansmembrane rotor. In order to understand the main features of such coupling, the most simple mechanistic device is proposed. An ionic turbine devised as a mobile piston inside a channel with periodic boundary conditions. The turbine is situated between two particle reservoirs of different concentration that interact with the piston generating the directional motion of the piston. The energy transduction of the motor is studied by applying a force against the natural motion of the motor. This force can hinder the spontaneous motion of the motor extracting mechanical work from it. Additionally, for a large enough external force, the ionic flux can be reverted. In this regime, the turbine acts as a pump in which the external force is used to increase the membrane energy by translocating particles against the Ionic Motive Force. An analysis of the motor including thermal fluctuation revealed that the flux of particles and the velocity of the motor are not proportional. In fact, the necessary force to inverse the velocity, the stall force of the motor; is smaller than the external force required to reverse the flux of the motor, the pump stall force. For intermediate

forces between both stall forces, a new regime appears in which the turbine does not extract useful energy. The external forces reverses the motor velocity and can not extract energy from it. In addition, the external force neither pumps particles that still are translocated in the gradient direction. In this new regime, named the leakage regime, the turbine is not only able to transduce energy but is continuously losing energy through the ion flux. For biological parameters, the width of the leakage zone is of the order of the pN, becoming of high significance in real biological turbines. Additionally, the energetic behaviour for this turbine is similar to the one observed in the F_1 motor in which the efficiency becomes null at the stall force of the motor. Again, this behaviour rises from thermal fluctuations that lead the dynamics of the machine near the machine stall. Hence, the efficiency obtained reaches new maxima for intermediate values of the external force. Actually, two new maxima appears, one for the pump regime and one for the motor regime. Following the same arguments as in the F_1 motor, the relevance of these energetic issues is high, since it implies that considering thermal fluctuations is essential in an optimisation process of the energy management of the motor.

The ideal model presented with the one–piston turbine lags a proper description of the diffusive nature of the particles. Therefore, a second model was proposed containing multiple vanes inside the channel. The velocity–flux relation was also analysed analytically for this model obtaining expressions for the velocity, the flux, the power and the efficiency in a more realistic scenario. This model presented the same features than the ones observed in the one–piston model. Actually, the flux of particles was larger resulting in a lower efficiency than the one predicted by the one–piston turbine. The changes in the flux also resulted in a larger leakage zone. Therefore, the introduction of more realistic elements in the turbine do not erase the effects of thermal fluctuations but enhance them.

This scenario was tested numerically to prove that the assumptions taken were valid at the biological scale. These simulations not only corroborates the analytical predictions but also sets a good tool to analyse a more realistic biological scenario in which other interactions, such as membrane voltage or particle–particle interaction, can be considered.

6

Future Perspectives

Even though different results have been attained in the current work, delving into these topics have raised more questions that failed to get a mention. For this reason, it is worth to account for some ideas inspired by this work that could be studied following the same methodology developed. Nevertheless, the topics collected here are only a taste of the possible applications. There are not only multiple directions of proceeding but also new problems will appear along with the new experimental observations that will take place in the following years.

Mechano–chemical analysis of φ29 packaging motor

The applied analysis to the mechano–chemical transduction to the F_1 motor can inspire the analysis of other ATP rotatory hydrolysis motors. Nonetheless, the current model can only serve as a guide and must be reformulated to accommodate the properties of these other motors. One possible application is the analysis of the operation of the ATPase homomeric ring that works as a double–stranded DNA packaging motor in the φ29 bacteriophage.

Again, the ATP hydrolysis cycle is tightly related with the trajectory of the

motor, in this case the DNA translocated distance in time. This motor also presents the step–like trajectories described in the current work (Fig. 6.1). However, this motor has the peculiarity that each transduction process does not need of one ATP molecule but four ATP molecules that attach to four of the homomeric ring binding sites. Once the four ATP molecules are attached, the motor hydrolyses the ATP molecules one at a time producing four mechanical substeps of 2.5 basepairs releasing a force able to overcome the high pressure to which this motor is exposed [41, 65]. As it happened with the F_1 motor, the dwell times between mechanical substeps depend with the applied external force. Interesting questions arise from these observations such as the performance advantages of this 4–ATP mechanism or how a fractional ADN base pair advance takes place. These questions can be understood in terms of the same energetic analysis developed in this work that must start with the finding of a suitable motive potential able to reproduce the substepping trajectories and its dependence with experimental control parameters. This work is currently in progress [53].

Non–equilibrium thermodynamics of transduction process

The mechano–chemical transduction through the flashing mechanism presented in Sec. 2.3 uses an out of equilibrium protocol where the potential flashings are triggered by the time duration of the different processes composing the cycle. However, alternative mechanisms can be proposed where the flashing mechanism is driven by the position of the motor along the motive potential. For instance, considering that mechanical steps end when the motor reaches the minimum of the driving potential. This possible mechanism corresponds to a protocol that requires information of the position of the motor in order to extract energy from

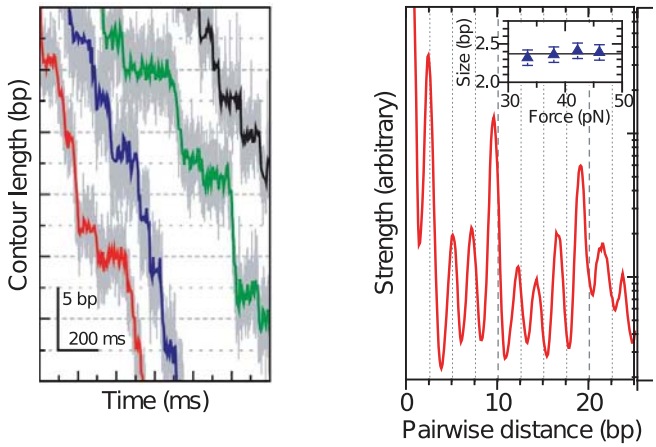

Figure 6.1: Experimental observations of the $\varphi 29$ operation. Left: Trajectory of the motor presenting steps. Right: Spatial autocorrelation function of the motor trajectory showing that the 10 basepair steps are composed by four 2.5 basepair substeps. Figure extracted from [39].

it. The energetic description of this protocol requires a correct analysis of the corresponding non–equilibrium thermodynamics that lead to relations between energy and information. Such relations have been already described theoretically and experimentally for similar systems to the ones proposed [68, 85]. In the framework developed in the current work, the information term could be computed from the known probability distributions of the motor along its trajectory. This extra energy would be an added term to the energy balance coming from the chemical reaction and subtracted to the actual chemical free energy ΔG. The study of these mechanisms could give a better insight into the mechano–chemical transduction processes in molecular motors and its optimisation.

Bacterial Flagellar Motor analytic models

The Stoke's minimal model proposed for the analysis of ionic rotatory motors in Section 4.1 does well in gathering the duration of the main processes composing the different transduction stages of each stator. However, it fails in reproducing the velocity–torque curves. One of the problems, already mentioned in Section 4.1, is the multiplicity of transduction processes when multiple stators act simultaneously on the rotor [7]. Thus, the tight coupling between the rotation coordinate and the actual state of one stator is lost. This problem was tackled introducing the ionic turbine. However, amends to the initial Stoke's equations (4.2) can be made to handle the torque–velocity profile. Actually, a set of studies using similar procedures exist producing successful appealing results [6, 42]. A possible alternative description should start with the Langevin equation for the motor relative to one stator,

$$\tau_{IMF} = \gamma_0 \omega_{\text{mech}} + \gamma_L \omega, \tag{6.1}$$

where τ_{IMF} is the internal torque supplied by the stator corresponding to the IMF, and ω and ω_{mech} are the average velocity of the motor and the average velocity during a mechanical process. This description splits the actual force balance in two components, the first term in the right hand side of (6.1) is the actual drag force of the stator applied during its mechanical time, while the second term of the right hand side of (6.1) is the global friction of the motor, which in this description is considered to be transmitted directly to the load drag which is the result of the average contribution of all the stators independent of their current state. Such description is equivalent to consider a soft link between the torque generating unit and the load that receives and average torque homogeneous in time. From expression (6.1) a new expression for the mechanical time is obtained,

$$t_{\text{mech}} = \frac{\gamma_0 \theta_0}{\tau_{\text{in}} - \tau} \tag{6.2}$$

Being τ the experimental reported torque of the motor computed as the drag friction force $\tau \equiv \gamma_L \omega$. This results in an explicit relation of the velocity with the experimental control parameters τ_{IMF} and ρ_1,

$$\tau = \tau_{\mathrm{IMF}} - \frac{\gamma_0}{\frac{1}{\omega} - \frac{t_0 + k_0 \rho_1^{-1}}{\theta_0}}. \tag{6.3}$$

This relation matches the dependence observed experimentally observed torque-velocity curves. For low values of the velocity saturates to the IMF $\tau(\omega \to 0) = \tau_{IMF}$ and decreases for larger velocities, whereas the maximum velocity corresponds to the case of zero measured torque, when no load is present in the system. Again, this model can be a good starting point to a motive potential analysis that leads to an energetic analysis of the Bacterial Flagellar Motor shedding light on its performance.

Complete Ionic Turbines

The current computational analysis of the Ionic Turbine presented in Section 4.2.3 was mainly applied to test the validity of the theory developed in Sections 4.2.1 and 4.2.2. Nevertheless, the study can be extended by including other features of real biological motors. Actually, expression (4.33), already contains possible interactions that must be included in a full description of an ionic turbine. One of these interactions include the electrostatic component of the IMF V_ϕ. This interaction will apply on any ion crossing the channel. Other possible interactions affecting the ion dynamics include ion–ion interactions and a position dependent diffusion coefficient of an ion inside a channel $\gamma_p(x)$ [59, 84].

Additionally, interaction terms affecting directly the interaction of the rotor with the stator can be introduced. This interaction can be expressed as a poten-

tial $V_T(X)$ of the turbine depending on the turbine position (4.33). The relevance of this potential lays in the possibility of altering the energy management of the turbine described in the current work. For instance, the introduction of a fixing potential that retains the turbine in a prefered position inside the channel. Such a potential can give place to a more stable turbine under low fluctuating forces dealing in a better way with the particle leakage. Thus, V_T presents a mechanism by which the operation of the motor can be optimized.

A

Algorithm for discontinuous multiplicative noise

Langevin equations (or their Fokker–Planck counterpart) turn to be a useful tool for describing biophysical systems. However, for the most interesting cases, these equations cannot be solved analytically, and explicit solutions must be obtained numerically through stochastic simulations [21, 22, 27, 32]. This appendix deals with general Langevin equations as the ones described along the text,

$$\dot{x} = f(x) + g(x)\xi(t), \tag{A.1}$$

where $\xi(t)$ is a Gaussian white noise with zero mean and covariation

$$\langle \xi(t)\, \xi(t') \rangle = 2\delta(t - t'). \tag{A.2}$$

In order to obtain numerically a trajectory from (A.1) a mathematical approximation for the increment $x(t + \Delta t) - x(t)$ is necessary. A formal integration of (A.1) is,

$$x(t + \Delta t) = x(t) + \int_t^{t+\Delta t} f(x(t'))\mathrm{d}t' + \int_t^{t+\Delta t} g(x(t'))\xi(t')\mathrm{d}t'. \tag{A.3}$$

Taylor expanding each one of the integrands $f(x(t'))$ and $g(x(t'))$ allows to solve numerically (A.3) with the desired accuracy. The first integral is determin-

istic and can be computed using the classical calculus rules,

$$\int_t^{t+\Delta t} f(x(t'))dt' = f(x(t))\Delta t + \mathcal{O}(\Delta t^2). \tag{A.4}$$

This integration corresponds to the first order expansion in $f(x(t))$ and can be used numerically by neglecting the terms of order $\mathcal{O}(\Delta t^2)$. This integration method is known as the Euler algorithm. More sophisticated algorithms exist that improve the numeric implementation of this integral.

On the other hand, due to its stochastic nature, the second integral in (A.3) cannot be univocally defined and additional assumptions are required. The problem lies in the evaluation of $g(x(t))$ along the integration interval. The evaluation point returns different solutions for the integral even in the limit $\Delta t \to 0$ resulting in different Fokker–Planck equations. Two interpretations are extensively studied: Itô and Stratonovich [22, 24, 82]. In the Itô interpretation, the stochastic integration is considered non–anticipating and therefore $g(x(t))$ is evaluated at the beginning of the integration interval,

$$\int_t^{t+\Delta t} g(x(t'))\,\xi(t')\mathrm{d}t' = g(x(t))\,W_{\Delta t}(t) + \mathcal{O}(\Delta t^{3/2}), \tag{A.5}$$

being $W_{\Delta t}(t)$ the Wiener increment,

$$W_{\Delta t}(t) = \int_t^{t+\Delta t} \xi(t')\mathrm{d}t', \tag{A.6}$$

which is a Gaussian process of zero mean and second moment

$$\langle \chi(t)^2 \rangle = 2\Delta t. \tag{A.7}$$

On the other hand, the Stratonovich interpretation evaluates the multiplicative term $g(x)$ in the intermediate position of the interval [22, 82]

$$\int_t^{t+\Delta t} g(x(t'))\,\xi(t')\mathrm{d}t' = g\left(\frac{x(t)+x(t+\Delta t)}{2}\right) W_{\Delta t}(t) + \mathcal{O}(\Delta t^{3/2}). \tag{A.8}$$

Here, a natural question arises: under which circumstances is correct either interpretation for a problem defined by (A.1)) and (A.2))? To answer this question is necessary to understand the nature of the process being described and, consequently, the specific derivation of the the Langevin equation. If they were obtained from a master equation a good choice is the Itô interpretation making it very popular among mathematicians. Nevertheless if the noise $\xi(t)$ represents an approximation of a realistic process (non–white or coloured), then Stratonovich is the answer. This is the case of the white noise approximation used to describe the dynamics of a particle under thermal fluctuations. More elaborated arguments can be found in Ref. [34].

The full expression for the integration of (A.3) up to first order for the Itô interpretation is obtained introducing (A.4) and (A.5) in (A.3),

$$x(t+\Delta t) = x(t) + f(x(t))\Delta t + g(x(t))\, W_{\Delta t}(t) + \mathcal{O}(\Delta t^{3/2}), \tag{A.9}$$

which is known as the Euler–Maruyama algorithm [32]. The stochastic generation of the increments of the Wiener process $W_{\Delta t}$ is easily implemented through the generation of Gaussian random numbers $N(0,1)$ [21],

$$W_{\Delta t} = \sqrt{2\Delta t}\; N(0,1). \tag{A.10}$$

On the other hand, the full first order algorithm for the integration of (A.3) for the Stratonovich interpretation, introducing (A.4) and (A.8) in (A.3) can not be obtained directly, since expression (A.8) introduces an implicit dependence with $x(t+\Delta t)$ that can not be isolated. An standard and simple procedure used to avoid the implicit term, is based in the assumption of continuity for the multiplicative function $g(x(t))$, and the use of Eq. (A.9),

$$g\left(\frac{x(t)+x(t+\Delta t)}{2}\right) \sim g(x(t)) + \frac{g'(x(t))g(x(t))}{2} W_{\Delta t}(t), \tag{A.11}$$

which returns the lowest order Stratonovich algorithm,

$$x(t+\Delta t) = x(t) + f(x(t))\Delta t + g(x(t))\, W_{\Delta t}(t) + \frac{g'(x(t))g(x(t))}{2} W_{\Delta t}^2 + \mathcal{O}(\Delta t^{3/2}), \tag{A.12}$$

known as the Milstein algorithm [38, 71]. Alternative algorithms to overcome the numerical integration in the Stratonovich interpretation use the analytical known relation between the Itô and the Stratonovich calculus. With these relations, the Stratonovich Langevin equation can be written as a new Itô Langevin equation that can be integrated using the Euler–Maruyama algorithm (A.9). Additionally, more algorithms can be derived by introducing different expansions and predictor–correctors [31, 37]. However, problems arise when the multiplicative function $g(x)$ is not continuous. In this situations none of the above mentioned solutions work, since all of them use the derivative of the multiplicative function $g'(x)$ to predict its spatial configuration. This discontinuity can be found in different ideal situations such as the Fokker–Planck white noise approximation (Sec. 2.4.2).

Different algorithms can be devised in order to avoid the spatial derivative based on the predictor–corrector scheme [69]. For instance, one possibility is to predict the forward position through an Itô step,

$$\begin{aligned} x_{\mathrm{I}}(t+\Delta t) &= x(t) + f(x(t))\Delta t + g(x(t))\, W_{\Delta t}(t), \\ x(t+\Delta t) &= x(t) + f(x(t))\Delta t + g\left(\frac{x(t) + x_{\mathrm{I}}(t+\Delta t)}{2}\right) W_{\Delta t}(t) + \mathcal{O}(\Delta t^{3/2}). \end{aligned} \tag{A.13}$$

This algorithm will be referred hereon as the predictor–corrector algorithm. The predictor–corrector algorithm is closely related with the Heun algorithm [21, 69] which is compatible with the Milstein algorithm (A.12) for a continuous $g(x)$ and also avoids the derivative problem,

$$x(t+\Delta t) = x(t)+f(x(t))\Delta t+\frac{g(x(t)) + g(x_{\mathrm{I}}(t+\Delta t))}{2}\, W_{\Delta t}(t)+\mathcal{O}(\Delta t^{3/2}). \quad \text{(A.14)}$$

The predictor–corrector algorithm and the Heun algorithms prove to be good algorithms when $g(x)$ is continuous. Nevertheless, as will be shown bellow, both algorithms do not converge to the correct solution for discontinuous multiplicative noise. Both algorithms fail to predict with enough accuracy the implicit term in the stochastic integral and an alternative solution for the stochastic integration is still required. Fortunately, this problem can be tackled by resorting to the nature of the stochastic integral. In the Stratonovich interpretation, the white noise is the resulting noise a non–white (coloured) noise in which its covariation time goes to zero [27, 93]. In order to implement this, the coloured noise have been chosen to be an Orstein–Ulenbeck process $\xi_{\mathrm{OU}}(t)$ which follows the Langevin equation

$$\tau\,\dot{\xi}_{\mathrm{OU}}(t) = -\xi_{\mathrm{OU}}(t) + \xi(t). \quad \text{(A.15)}$$

The white noise limit $\xi_{\mathrm{OU}}(t) \to \xi(t)$ is achieved for a correlation time $\tau \to 0$. The OU process can be simulated through standard integration [21],

$$\xi_{\mathrm{OU}}(t+\Delta t) = \xi_{\mathrm{OU}}(t)\left(1-\frac{\Delta t}{\tau}\right) + \frac{W_{\Delta t}(t)}{\tau} + \mathcal{O}(\Delta t^{3/2}). \quad \text{(A.16)}$$

Once the noise values are obtained, they can be introduced in the integration of the Langevin equation directly

$$x(t+\Delta t) = x(t) + f(x(t))\Delta t + g(x(t))\,\xi_{\mathrm{OU}}(t)\Delta t + \mathcal{O}(\Delta t^{3/2}). \quad \text{(A.17)}$$

The correlation time τ is a free parameter that must be chosen smaller than any characteristic time of the simulated system in order to avoid introducing any new phenomenology in the equations. On the other hand the correlation time τ must be larger than the integration step time Δt to observe its effect.

Additionally, other algorithms with a greater accuracy and efficiency [20, 37] for the OU process generation can be used. This algorithm will be referred heron as Orstein–Ulenbeck algorithm.

In order to test the different algorithms proposed for the discontinuous multiplicative noise, is necessary to work in a benchmark where the analytical solution is available. The easiest scenario is that of a Brownian particle located inside a one–dimensional box of length L without drift $f(x) = 0$ and a a discontinuous multiplicative function that follows a step distribution in space.

$$\dot{x} = g(x)\xi(t) \quad , \quad \left.\begin{array}{l} g(x < L/2) = \sqrt{T_a} \\ g(x > L/2) = \sqrt{T_b} \end{array}\right\}. \tag{A.18}$$

This scenario is equivalent to consider a different temperature at each half side of the box. The corresponding Fokker–Planck equations for each interpretation are,

$$\frac{\partial P(x,t)}{\partial t} = \frac{\partial^2}{\partial x^2} g^2(x) P(x,t), \qquad \text{(Itô)}, \tag{A.19}$$

$$\frac{\partial P(x,t)}{\partial t} = \frac{\partial}{\partial x} g(x) \frac{\partial}{\partial x} g(x) P(x,t), \qquad \text{(Stratonovich)} \tag{A.20}$$

which have the trivial steady state solution,

$$P_{\text{Itô}}(x) \sim \frac{1}{g^2(x)}, \qquad P_{\text{Strat.}}(x) \sim \frac{1}{g(x)}, \tag{A.21}$$

which for the current case is a step–like probability profile. The ratio between the probability at each side $R = P(x > L/2)/P(x < L/2)$ is a measure of the resulting distribution,

$$R_{\text{Itô}} = \frac{T_a}{T_b}, \qquad R_{\text{Strat.}} = \sqrt{\frac{T_a}{T_b}}. \tag{A.22}$$

For this elemental scenario, different algorithms have been tested generating large time and ensemble averages to reduce the statistical errors. The results show that Euler–Maruyama works perfectly to describe the Itô solution. On the

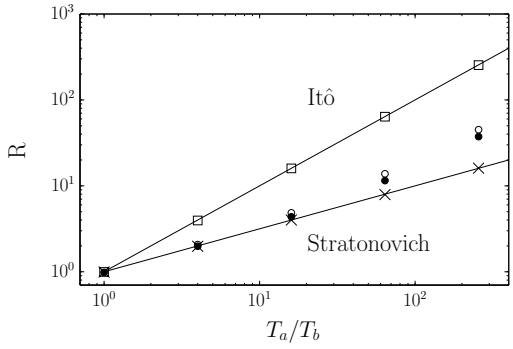

Figure A.1: Theoretical predictions (*lines*) and numerical simulation results (*symbols*) for different algorithms and stochastic interpretations of Langevin equation (A.21). Euler-Maruyama (A.9) (*squares*), predictor–corrector (A.14) (*full circles*), Heun (A.14) (*empty circles*) and Orstein–Ulenbeck algorithm (A.17) (*crosses*). Parameters used are $L = 1$, $\Delta t = 10^{-5}$, $n > 10^7$ time-steps and $N = 100$ trajectories. $\tau = 10^{-3}$ for the OU algorithm.

other hand, for the Stratonovich interpretation, neither the predictor–corrector algorithm nor the Heun algorithm work for the the discontinuous $g(x)$ converging to a wrong value independently of the time step chosen. However, the OU algorithm predicts perfectly the resulting probability profile (Figs. A.1 and A.2).

Moreover for OU algorithm, the use of a coloured noise whose time increments are correlated needs a careful attention if a reflecting boundary is present. When a particle is reflected at the boundary, the sign of the coloured noise (velocity) must be changed in the next integration step $\xi_{\mathrm{OU}}(t+\Delta t)$ (Fig. A.2), otherwise an anomalous density of particles is accumulated near the reflecting walls. Similar tests can be done with the OU algorithm for more complex Langevin equations as the ones used in the Fokker-Planck white noise approach (Sec. 2.4.2) leading always to correct predictions.

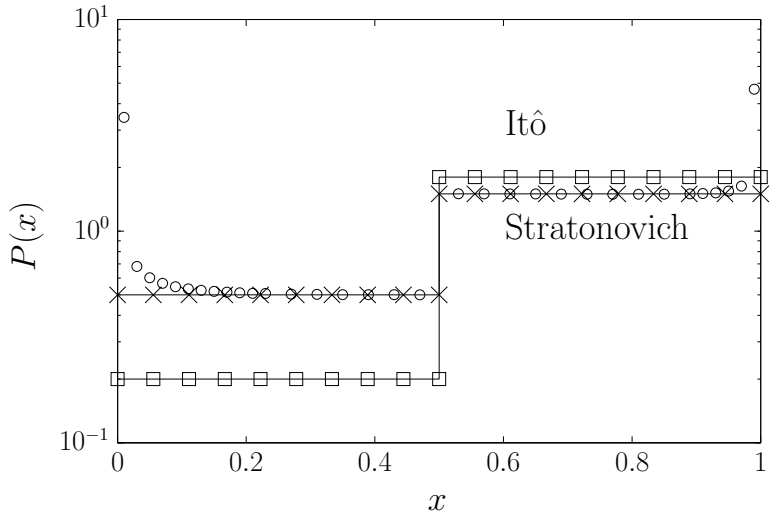

Figure A.2: Steady probability densities. Euler-Maruyama algorithm (*squares*), OU algorithm without noise inversion (*circles*) and OU algorithm with noise inversion at the walls (*crosses*). The probability is normalised to the centre of the box so the accumulation of density in the walls do not conceal the probability match near the centre of the box. Parameters used are the same as in Fig. (Fig. A.1) with $T_a/T_b = 9$.

B

Numerical analysis of the ionic turbine

Even though the aim of the analytic study of the turbine is to give a global framework to find essential mechanisms in the translocation of ions in molecular turbines, the contrast of the theory with simulations requires to chose a specific set of potentials and calculations for the simulations. This appendix summarises which parameters and algorithms have been used and the reasons for the choice. The different parameters described hereon are summarised in Table B.1

Numeric Integration

The numeric analysis has been developed using a Graphics Processing Unit (GPU) using Computing Unified Device Architecture (CUDA) which works using massive parallelisation allowing to compute several independent processes at the same time. This is of importance because, despite the native algorithms already optimised for GPU computing, the global structure of the program is chosen to take the most of the massive parallelisation. For instance, the rarified particle cytosol described, is most suitable to GPU computing since each particle can be assigned to an individual thread of the process, parallelising completely the

Parameter	Value	Description
H	10 k_BT	Height of the interaction potential
a	0.7	Width of the interaction potential
Δt	$10^{-5}\mu$ s	Time step for the particle integration
ΔT	$10^{-3}\mu$ s	Time step for the vanes integration
N	1024	Number of particles
L	48 nm	Length of the simulated box
L_E	20 nm	Length of each exchange zone

Table B.1: Parameters used along the turbine simulation

dynamics of the turbine–particle system. This can be done because the memory that particles need to share is minimal. On the other hand, since the friction coefficient of the particles is order of magnitudes smaller than the friction coefficient of the turbine the dynamics of both elements occur in different temporal scales. Hence, in order to reproduce the motion of the vanes is only necessary to update its position after several integrations of the particle dynamics. This also enhances the parallel computing allowing several integration steps per thread without modifying the shared memory.

Since the potentials that appear in the simulation are smooth and there is no memory in the equations, a simple Euler–Maruyama algorithm (A.9) is enough to reproduce the dynamics proposed in (4.33). For each particle it reads,

$$x_i\left((n+1)\Delta t\right) = x_i\left(n\Delta t\right) + \frac{F_i(n\Delta t)}{\gamma_p}\Delta t + \sqrt{\frac{2k_BT\Delta t}{\gamma_p}}\,N_i(0,1). \tag{B.1}$$

The index i covers all the particles in the system, F_i is the sum of all the forces acting on the particle, and $N(0,1)$ is a Gaussian random number of zero mean and unity variance. F_i contains all the forces acting on each particle, however for the case being only the vane–particle force is considered. On the other hand,

the dynamics of the vanes is evaluated after every lapse of time $\Delta T \gg \Delta t$. This include the evaluation of the average interaction force that the particles exert on the vanes along all the particle integration steps between vane position updates.

$$X\left((n+1)\Delta T\right) = -\frac{\langle \sum_i F_i \rangle_{\Delta T}}{\gamma}\Delta T + \sqrt{\frac{2k_B T \Delta T}{\gamma}}\, N(0,1). \tag{B.2}$$

The initial configuration of the particles $x_i(0)$ is taken to be random and out of the turbine having a starting transitory in the trajectory that is not taken into account in the trajectory analysis, the duration of this transitory is comparable with the characteristic time of the dynamics of the vanes.

Interaction Potential

The particles and the vanes interact through the short range repulsive potential $V_p(X - x_i)$. The requirements for such a potential are two: a hardcore part (or at least high enough) that retains the particles at the corresponding side of the vane, and a quick decaying to zero for longer distances (Fig. 4.15). Many potentials can be chosen with these characteristics, and the final behaviour should not strongly depend on the potential chosen. For the case being, a Gaussian profile is used,

$$V_p(x_i - X) = H\mathrm{e}^{((x_i - X)/a)^2}. \tag{B.3}$$

Parameters H and a describe the height and width of the potential which must be chosen carefully to avoid as much as possible particle overcoming the potential and also to keep a force profile that remains in the working scale. A Brownian particle has a typical displacement during an integration step $\Delta x = \sqrt{2k_B T \Delta t/\gamma_p}$. This displacement must be smaller than the width of the potential since an integration step must not introduce a particle very far inside the potential $p \equiv \frac{\Delta x}{a} < 1$. This returns a suitable integration time step for the particles,

$$\Delta t = \frac{p^2 a^2 \gamma_p}{2 k_B T}. \tag{B.4}$$

On the other hand, it is necessary that the largest force introduced by the potential expels de particle from the potential at a physical reasonable distance. The maximum reaction force of the potential is $V_p'(\mathrm{MAX}) = \frac{2H\mathrm{e}^{-1}}{a} \propto \frac{H}{a}$, which displaces a particle a distance $\delta = \frac{Hp^2 a}{2k_B T}$ in a lapse Δt. Making this distance comparable to the width of the vane $a = \delta$, results in a direct relation between the the height H and the fraction p,

$$H = \frac{2k_B T}{p^2}. \tag{B.5}$$

Thus a penetration $p = 0.3$ results in a height of $H \propto 10 k_B T$ and for a width of the vane of the order of the nanometer, an integration time step of $\Delta t \propto 10^{-5} \mu$s.

Available volume between vanes

Because of the width of the interaction potential, the volume of particles translocated is not the volume corresponding to the intervane distance, but is reduced by a fraction β, $V_0 = dA\beta$. Considering that a translocation carries a density ρ_0 of particles coming from the either side of the turbine, the number of particles translocated in each cycle is $\Delta N = V_0 \rho_0$ which can be written as a definition for β as,

$$\beta \equiv \frac{\Delta N}{\rho_0 dA}. \tag{B.6}$$

This equivalence can also be interpreted as well in terms of particles translocated. Hence, β is the fraction of the particles translocated over the ideal translocation of a volume of particles dA. Therefore, in order to compute β is necessary to

know which is the particle density profile near the vane. This spatial density (or probability) in equilibrium is proportional to the Boltzmann factor,

$$\rho(x) = \rho_0 \mathrm{e}^{-\tilde{V}_p(x)/k_B T}. \tag{B.7}$$

The tilde in $\tilde{V}_p(x)$ states for the contribution of the different vanes in the turbine,

$$\tilde{V}_p(x) = \sum_j V_p(x - X_j). \tag{B.8}$$

Actually, the value of β depends not only on the geometry of the interaction potential but also on the dynamics of the vane entering the turbine and trapping the particles. For instance, if the vane enters the turbine, in the best case scenario, it will be able to translocate every particle located between the edge of the turbine and the next vane (Fig. B.1) obtaining a translocated average amount of particles

$$\Delta N = \int_0^d A\rho(x)\mathrm{d}x = A\rho_0 \int_0^d \mathrm{e}^{-V_p(x-d)/k_B T}\mathrm{d}x, \tag{B.9}$$

which compared with the definition of β (B.6) results in the explicit relation,

$$\beta_1 = \frac{1}{d}\int_0^d \mathrm{e}^{-V_p(x-d)/k_B T}\mathrm{d}x. \tag{B.10}$$

This value will depend on the actual form of the interaction potential and for the Gaussian current case gives $\beta_1 \simeq 0.75$. On the other hand, if the potential is considered to enter slowly in the turbine through several fluctuations across the turbine edge, the enclosed volume of particles is expected to equilibrate with the donor reservoir (Fig. B.1) trapping a lower number of particles,

$$\Delta N = \int_0^d A\rho(x)\mathrm{d}x = A\rho_0 \int_0^d \mathrm{e}^{-(V_p(x)+V_p(x-d))/k_B T}\mathrm{d}x, \tag{B.11}$$

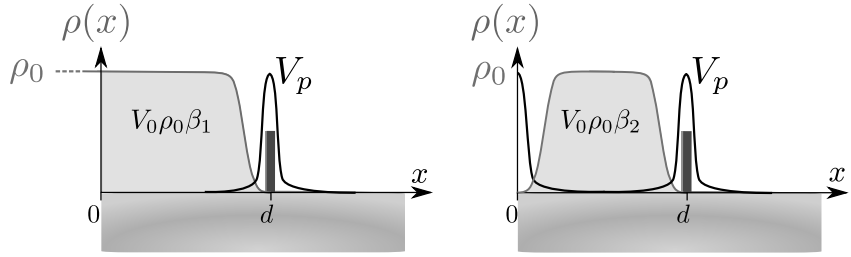

Figure B.1: Different configurations indicating the two boundaries for β. Left: Scheme showing the density of particles inside the turbine (*grey shade*) prior to the entering of a vane. Once the vane enters it is capable to enclose $\Delta N = V_0\rho_0\beta_1$ particles. Right: If the vane is not able to retain all the particles inside the space between vanes, the maximum density inside the turbine is equal to the density of the reservoir. In this limit, the amount of particles translocated is $\Delta N = V_0\rho_0\beta_2$.

Again, it can be compared with (B.6) obtaining the relation,

$$\begin{aligned}
\beta_2 &= \frac{1}{d}\int_0^d \mathrm{e}^{-(V_p(x)+V_p(x-d))/k_BT}\mathrm{d}x \qquad \text{(B.12)}\\
&= \frac{1}{d}\int_0^d /2\mathrm{e}^{-(V_p(x)/k_BT}\mathrm{d}x + \int_d /2^d\mathrm{e}^{-(V_p(x-d)/k_BT}\mathrm{d}x\\
&= \frac{2}{d}\int_d /2^d\mathrm{e}^{-(V_p(x-d)/k_BT}\mathrm{d}x = \frac{2}{d}\left(\int_0^d \mathrm{e}^{-(V_p(x-d)/k_BT}\mathrm{d}x - \frac{d}{2}\right)\\
&= 2\beta_1 - 1. \qquad \text{(B.13)}
\end{aligned}$$

Where the short–range property of the potential ($V(d) \simeq 0$) and its symmetry ($V(x) = V(-x)$) have been used. For the current case, relation (B.13) returns a value $\beta_2 \simeq 0.5$. Both values β_1 and β_2 give an upper and a lower boundary to the actual value of β. Numerically, for the Gaussian potential described under biological values of the parameters, it is obtained a value of $\beta \simeq 0.7$

Reservoirs

So far, only the interaction of the particles inside the turbine is considered. However, the dynamics of the particles outside the turbine is also necessary. For the sake of computing efficiency, the particles are confined in a one–dimensional box of length L. The turbine of length $D \ll L$ is located at the centre of the box, generating two particle reservoirs at each side of the turbine (Fig. B.2). All the particles are free to diffuse along each reservoir with reflective boundary conditions. The number of particles and the length L are chosen to fulfil the required particle densities in each reservoir with the desired precision being usually enough with 1024 particles and L=48 nm.

Since the biological conditions require a constant concentration of particles at each side of the turbine without the depletion of a reservoir, a mechanism to maintain the concentrations is needed. In addition, optimisation of parallel computation requires that all the particles are treated equally without a minimum information exchange between them. This can be achieved introducing a balance mechanism in which each particle has a probability per unit of time (rate) of changing from one reservoir to the other. Choosing this rate to be inversely proportional to the desired concentration of its actual reservoir $k_{12} = \frac{C}{\overline{\rho}_1}$ and $k_{21} = \frac{C}{\overline{\rho}_2}$, the density evolution of reservoir 1 will be,

$$\dot{\rho}_1 = -k_{12}\rho_1 + k_{21}\rho_2 = C\left(\frac{\rho_2}{\overline{\rho}_2} - \frac{\rho_1}{\overline{\rho}_1}\right), \tag{B.14}$$

which evolves to the situation in which $\rho_1 = \overline{\rho}_1$. This condition, however, cannot be applied along all the reservoir since it can destroy any spatial density profile near the turbine. For this reason, the exchange is only applied in a zone far enough of the turbine (Fig. B.2) occupying a distance L_E of each reservoir. Once a particle is selected for reallocation it is dropped randomly inside the

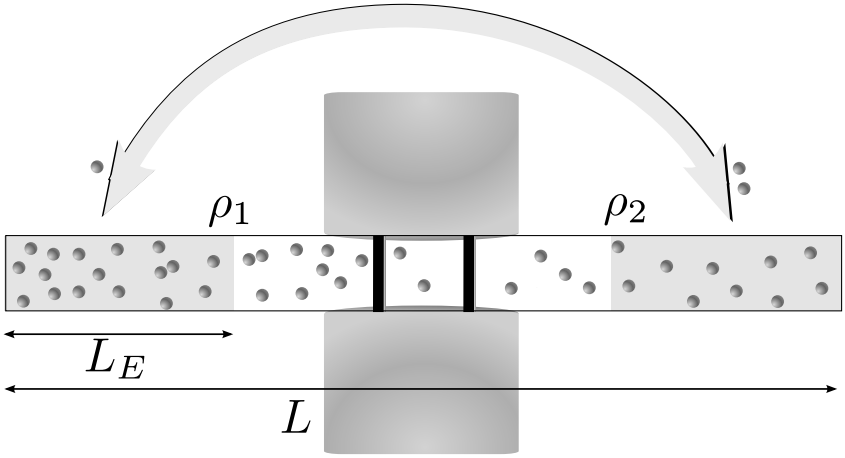

Figure B.2: Computational box used during the simulations. The exchange zones of the reservoir (*dashed gray zones*) of length L_E are used for density conservation in each reservoir.

exchange zone of the other reservoir. The value of C is chosen to balance the concentrations of each exchange zone faster than the turbine translocation.

Resumen (Spanish Summary)

Introducción

Las célula es la mínima unidad de vida. Tanto en el sentido de que constituye la unidad funcional de cualquier ser vivo como que es la mínima entidad a la que se puede considerar viva. Asimismo, comparten propiedades comunes entre ellas. Las células nacen, se alimentan, se pueden reproducir, pueden tener la capacidad de moverse y finalmente mueren. Todos estos procesos se pueden observar bajo la lupa de la Física obteniendo una descripción equivalente pero con una terminología completamente distinta. Una célula, bajo esta visión, es un sistema complejo, fuera del equilibrio, que está constantemente intercambiando materia, energía e información. De esta forma, una célula alimentándose es un sistema obteniendo materia del exterior para extraer energía, y una célula moviéndose está transformando la energía química interna del sistema en trabajo.

A summary in Spanish is included following the current legislation of the University of Barcelona

Para realizar esta manipulación de energía y materia, las células tienen una maquinaria interna, un conjunto de macromoléculas conocida como *máquinas moleculares*. Las funciones que tienen estas máquinas en una célula son numerosas: transportar macromoléculas, transcribir el ADN, contraer músculos... Concretamente, cuando el objetivo de la máquina es realizar un trabajo mecánico, se puede denominar también *motor molecular*. No obstante, ambos nombres, máquina molecular o motor molecular, así como máquina proteica, son usados indistintamente en la literatura.

Un ejemplo de motor molecular que realiza un trabajo mecánico es la kinesina. Las kinesinas son motores moleculares que trabajan junto a los microtúbulos, uno de los tipos filamentos que conforman el citoesqueleto celular. Los microtúbulos funcionan como vías para el desplazamiento de la kinesina. Así, ésta es capaz de interactuar con los microtúbulos generando una fuerza tangencial a éste que aprovecha para diversas funciones, como por ejemplo el transporte direccional de macromoléculas o vesículas a lo largo de la célula (Fig. R.1). La energía necesaria para realizar este trabajo se extrae de la hidrólisis de moléculas de adenosín trifosfato (ATP). No sólo la kinesina funciona con ATP, siendo éste una de las fuentes más importantes de energía a nivel subcelular. El ATP se encuentra difundiendo de forma natural en la célula. Así, cuando una molécula de ATP llega al bolsillo catalítico de la kinesina, ésta es capaz de catalizar su hidrólisis aprovechando la energía liberada en la reacción.

El reciclaje de los productos de la hidrólisis del ATP, a saber, adenosín difosfato (ADP) y fosfato, tiene lugar dentro de la célula. De nuevo, una máquina molecular se encarga de este proceso, la F_0F_1–ATP sintasa (Fig. R.1). Este motor, ubicuo en todos los sistemas vivos, sintetiza ATP a partir de ADP y fosfato. La energía necesaria para realizar esta síntesis la extrae de la energía electroquímica

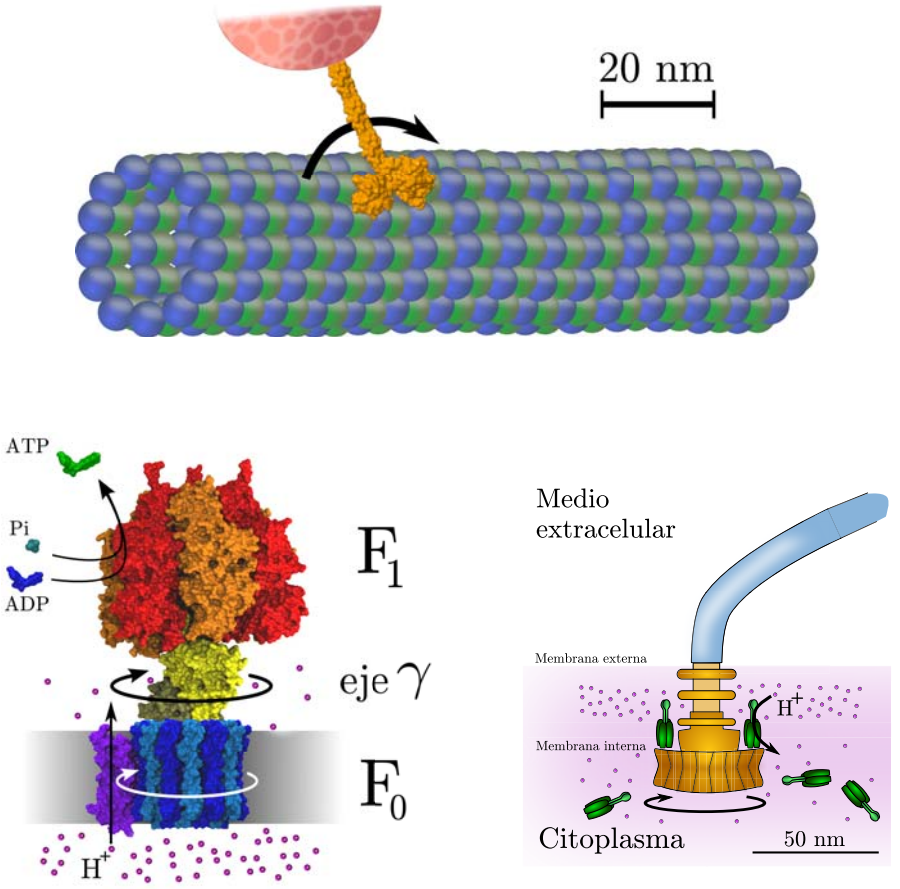

Figura R.1: Ejemplos de máquinas moleculares. Arriba: Kinesina transportando una carga a lo largo de un microtúbulo. Representación superficial de la proteína basada en la estructura 1N6M del PDB. Abajo: Ejemplos de motores moleculares rotatorios. La F_0F_1–ATP sintasa (izquierda) y el Motor Flagelar de las Bacterias (MFB) (derecha). Representación superficial de la ATP–sintasa extraida de las estructuras 1Q01 y 1C17 del PDB. Dibujo del MFB basado en [7].

resultante de una diferencia de concentración iónica a través de una membrana. Para ello, la F_0F_1-ATP sintasa se encuentra en la membrana interna de las mitocondrias en células eucariotas. En células vegetales también se puede encontrar en los cloroplastos, mientras que en procariotas se encuentra en la membrana plasmática de la célula. Esta energía electroquímica es el resultado del procesamiento del alimento de la célula. Así la F_0F_1–ATP sintasa es una máquina fijada a una membrana que se encarga de transformar una energía local en forma de un gradiente iónico en una energía que puede difundir a lo largo de la célula, el ATP.

La F_0F_1–ATP sintasa tiene tres partes bien diferenciadas: La subunidad transmembranal F_0, la parte globular F_1 y el eje γ (Fig. R.1). La transducción energética comienza en la subunidad F_0. Esta subunidad funciona como una turbina molecular permitiendo un flujo de iones a través de ella y acoplándolo al giro de su rotor. Este giro es transmitido a lo largo del motor a través del eje asimétrico γ. El eje γ, que se prolonga dentro de la subunidad F_1, gira dentro de F_1 generando una deformación estructural en ésta. Esta deformación es utilizada por la subunidad F_1 para unir el ADP y el fosfato, localizados en el centro activo de F_1, formando así una nueva molécula de ATP.

Las dos subunidades F_0 y F_1 se pueden aislar experimentalmente dando lugar a dos máquinas moleculares independientes. Por un lado el motor F_0 que funciona como una turbina iónica generando un movimiento rotatorio. Por otro lado el motor F_1 se puede utilizar para sintetizar ATP en el laboratorio, mediante la rotación artificial del eje γ. Aún más interesante resulta la posibilidad que presentan ambas máquinas de revertir su régimen de trabajo. De esta forma el motor F_1 en presencia de un exceso de ATP puede hidrolizar moléculas de ATP generando una rotación activa del eje γ. El motor F_1 en este régimen recibe el

nombre, F_1–ATPasa. La F_1–ATPasa es uno de los motores moleculares rotatorios más estudiados a nivel experimental, y es uno de los principales objetivos de estudio de este trabajo.

Los gradientes iónicos no sólo son usados por la F_0F_1–ATP sintasa, sino por muchas otras máquinas transmembranales como las usadas por las bacterias para hacer girar sus flagelos. El Motor Flagelar de las Bacterias (MFB) es uno de los motores moleculares biológicos más grandes y consiste en un turbina molecular semejante al F_0 (Fig. R.1). Este motor junto al F_1 serán los dos motores rotatorios en que se basa el actual trabajo.

Metodología para el estudio de máquinas moleculares

La transformación energética que llevan a cabo los motores moleculares es el resultado del conjunto de interacciones que tiene lugar entre los átomos que componen el motor y su entorno. Este escenario presenta una alta complejidad. Es por eso que un enfoque más general es necesario para entender los mecanismos básicos que utilizan los motores moleculares. Diferentes enfoques y modelos teóricos son posibles correspondiendo a diferentes niveles de abstracción. Cada perspectiva contribuyendo de forma diferente a la comprensión de los motores. De esta forma, un estudio detallado atomista puede permitir entender que papel juega cada aminoácido en en el ciclo energético del motor. Sin embargo, la capacidad computacional actual no permitirá reproducir más de un ciclo del motor. Por otro lado, un acercamiento cineticoquímico más general consistiría en reducir toda la dinámica del motor a un número discreto reducido de conformaciones

del motor con una dinámica de evolución entre ellas. Este acercamiento puede dar una idea de cuales son las configuraciones básicas que describen el funcionamiento del motor pero no permitiría recoger detalles de la dinámica del motor como fuerzas o energías. El trabajo actual sigue un acercamiento intermedio que utiliza como punto de partida el principal observable de la dinámica del motor, su trayectoria. La mayoría de experimentos con motores moleculares consisten en observar su movimiento anexando una carga visible bajo el microscopio para poder recoger la trayectoria del motor. Este montaje experimental permite modificar las condiciones experimentales para observar como varían las propiedades de la trayectoria del motor. Así, este enfoque intenta relacionar la coordenada espacial observable del motor con su configuración química interna a la vez que permite estudiar la dinámica asociada.

A pesar de las similitudes que hay entre los motores macroscópicos y los motores nanoscópicos, ambos trabajan bajo condiciones físicas y químicas muy diferentes que hay que tener en cuenta a la hora de plantear la dinámica de estos motores. Una de las diferencias más importantes es la relevancia de las fuerzas viscosas frente a las fuerzas inerciales. Los motores moleculares trabajan a números de Reynolds muy bajos en que la velocidad del motor es proporcional a la fuerza neta que actúa sobre el motor. Por otro lado, en la escala biológica celular, el efecto de las fluctuaciones térmicas sobre el motor es importante. Estas fluctuaciones vienen dadas por las colisiones aleatorias de las moléculas que lo envuelven por el hecho de estar termalizadas. La energía asociada a estas colisiones es comparable al resto de energías que rigen los procesos subcelulares. Teniendo en cuenta estos dos efectos: fricción y fluctuaciones, la dinámica del motor puede describirse mediante una ecuación de Langevin sobreamortiguada para la coordenada de avance θ del motor. Para un motor rotatorio, la ecuación de Langevin asociada es,

$$\gamma\dot{\theta} = -V'(\theta, t) + \tau_{\mathrm{c}} + \xi(t). \tag{R.1}$$

Donde γ es la fricción del sistema motor–carga, τ_{c} es el torque ejercido por efectos externos al motor, $\xi(t)$ es el ruido térmico descrito por una función aleatoria y $V(\theta, t)$ es el potencial interno del motor del cual resulta la fuerza ejercida por el motor para realizar su función. Así, $V(\theta, t)$ contiene la información sobre el funcionamiento del motor. Por eso, el objetivo de estudiar la máquina mediante (R.1) es obtener una expresión para el potencial motor que en general dependerá de forma no lineal con la posición y el tiempo con los diferentes procesos físico–químicos que tienen lugar en la transducción.

F_1 bajo fuerzas disipativas

La observación de las trayectorias de los motores moleculares revela que el avance del motor no es continuo en el tiempo sino que muestra pasos discretos. Esto permite distinguir dos tipos de procesos. Por un lado, los procesos durante los cuales el motor ejerce una fuerza neta, desplazándose. Estos procesos reciben el nombre de procesos mecánicos. Por otra parte, los procesos químicos durante los cuales el motor no realiza ningún desplazamiento activo. Los procesos químicos coinciden con los procesos catalíticos del motor. Para motores que trabajan con hidrólisis de ATP, en general la trayectoria presenta un proceso químico por ciclo que resulta de la espera de ATP y la expulsión de los productos de la hidrólisis y, por otro lado, un proceso mecánico resultante de la transformación energética de la hidrólisis de ATP. Así, de forma genérica, se obtiene una fórmula para el valor medio de la velocidad, describiendo los tiempos químicos mediante la cinética de Michaelis–Menten típica de procesos catalíticos y por otro lado describiendo los tiempos mecánicos a través de la dinámica sobreamortiguada del motor [56].

$$\omega = \frac{\theta_0}{\sum t_i} = \frac{\theta_0}{t_0 \left(\frac{k_0}{[\mathrm{ATP}]} + 1 \right) + \theta_0^2 \frac{\gamma}{\Delta G_{\mathrm{ATP}}}}, \tag{R.2}$$

Donde θ_0 es la distancia angular de un ciclo del motor que viene fijada por la estructura bioquímica del motor y t_i la duración de cada uno de los procesos, tanto químicos como mecánicos, que conforman un ciclo del motor. k_0 y t_0 son parámetros cinéticos que describen los tiempos químicos del motor y ΔG_{ATP} la energía útil de la hidrólisis de ATP. Aplicando la expresión (R.2) a la F_1–ATPasa se puede obtener una relación para la velocidad angular del motor con la fricción de la carga y la concentración de ATP donde todos los parámetros se pueden extraer de medidas experimentales [56]. El resultado se puede comparar con observaciones experimentales de la velocidad media del motor obteniendo un buen resultado (Fig. R.2).

La validez de este resultado sugiere la propuesta de un potencial motor $V(\theta, t)$ que describa la dinámica del motor con más detalle como los subpasos del motor observados experimentalmente. Esto se puede conseguir mediante dos potenciales de dientes de sierra con la periodicidad biomolecular del motor que se alternan de forma intermitente, cada potencial describiendo un estado del centro activo del motor: vacío u ocupado. De nuevo, la información experimental disponible permite describir este tipo de potencial sin ningún parámetro ajustable. De hecho, el modelo es capaz de predecir la longitud del subpaso directamente mediante argumentos de optimización de la transducción del motor [56]. Debido a la no linearidad de las ecuaciones, la trayectoria del motor tiene que obtenerse computacionalmente, integrando la ecuación estocástica (R.1) numéricamente para el potencial propuesto. El valor medio de la velocidad resultante es más pequeño que el de la predicción teórica (R.2) que se corresponde a un mejor ajuste los datos experimentales (Fig. R.2). Analizando las diferencias entre el resultado

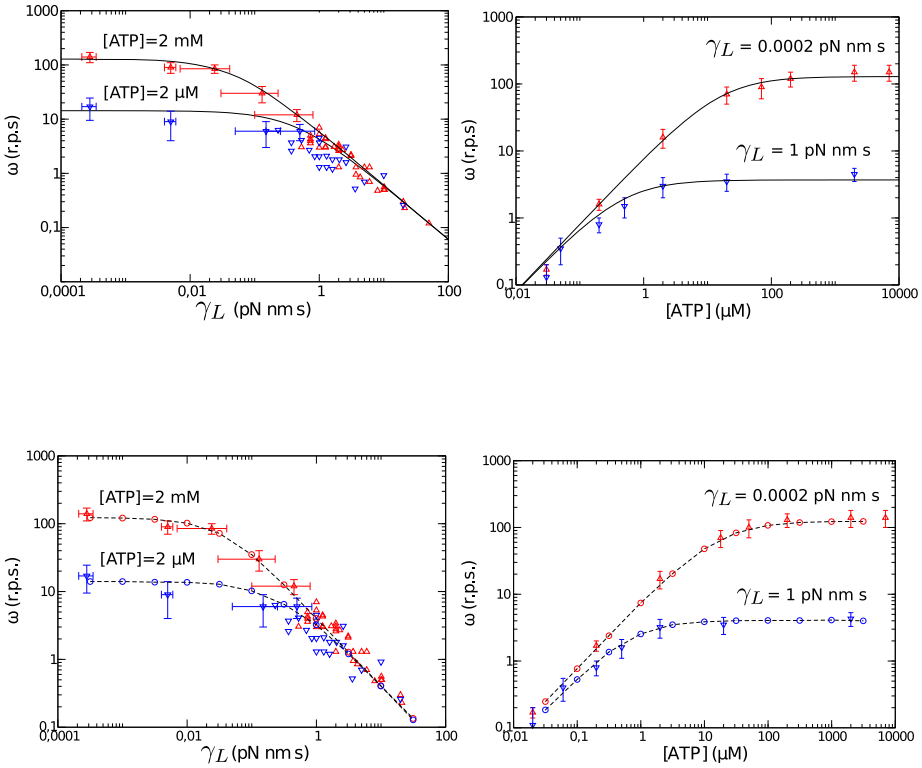

Figura R.2: Comparativa de los resultados experimentales de la velocidad (*triángulos*) con las predicciones (*líneas*). Arriba: Comparación con el resultado teórico determinista (R.2). Abajo: Comparación con el resultado de las simulaciones estocásticas de la ecuación de Langevin (R.1).

determinista y el resultado aleatorio se observa que las discrepancias se deben principalmente a las fluctuaciones térmicas que producen eventos fallidos. Estos eventos corresponden a hidrólisis de ATP que no producen un avance exitoso del motor a pesar de consumir la energía de hidrólisis. Este fenómeno se puede aproximar analíticamente mediante la ecuación de Fokker–Planck asociada a (R.1) estudiando la evolución de las colas de la distribución de probabilidad de la carga en el espacio [56]. De esta forma se muestra que los eventos fallidos tienen una dependencia importante con la fricción de la carga fallando más eventos de hidrólisis mientras más grande es la carga.

F_1 bajo fuerzas conservativas

El análisis desarrollado en la sección anterior no tiene en cuenta la presencia de torques conservativos sobre el motor F_1 ya que se basa en experimentos puramente disipativos ($\tau_c = 0$). No obstante, experimentalmente también se puede inducir un torque externo sobre la carga mediante diferentes técnicas como pinzas ópticas, pinzas magnéticas o electrorotación. En este caso, el análisis es más complejo ya que un torque conservativo afecta al ciclo de transducción tanto en los procesos químicos como en los procesos mecánicos. Esto se puede cuantificar teniendo en cuenta los efectos que tiene el torque conservativo sobre los diferentes procesos mecánicos y químicos [57],

$$\langle \omega \rangle = \frac{\theta_0}{[\theta_1 - \delta\theta(\tau_c)]\frac{\gamma}{\tau_c+\tau_1} + \theta_2\frac{\gamma}{\tau_c+\tau_2} + t_0\left(1 + \frac{k_M(\tau_c)}{[ATP]}\right)}. \tag{R.3}$$

Esta expresión contiene cuatro nuevos elementos con respecto a (R.2). Por un lado tiene en cuenta los subpasos de la trayectoria θ_1 y θ_2 y sus respectivos torques asociados τ_1 y τ_2. Por otro lado, el torque efectivo en el proceso mecánico de

casas subpaso se ve incrementado por el torque conservativo τ_c. En tercer lugar la distancia a recorrer por el motor durante el tiempo mecánico se ve reducida una cantidad $\delta\theta$. Este efecto es puramente térmico. Debido a la asimetría del potencial inducida por el torque conservativo, la posición media de equilibrio dentro del potencial varía. Este fenómeno se puede cuantificar analíticamente resolviendo la distribución de probabilidad de equilibrio de la carga en el pozo de potencial mediante la ecuación de Fokker–Planck obteniendo una relación de $\delta\theta$ con τ_c y con la temperatura. Finalmente hay una cuarta dependencia del potencial con el torque externo en los tiempos catalíticos del motor. Este fenómeno esta relacionado con el hecho de que un torque externo deforma el motor modificando su estructura bioquímica y con ello su cinética de reacción. Este fenómeno se puede describir mediante una relación lineal $k_M(\tau_c)$.
No sólo la dependencia de la duración de los diferentes procesos se puede cuantificar analíticamente sino que de nuevo todos los parámetros se pueden extraer directamente de información experimental. De esta forma la velocidad resultante de (R.3) se puede comparar con resultados experimentales de la velocidad sin la necesidad de ningún tipo de ajuste. El resultado, como en el caso disipativo, es un buen ajuste del modelo a los experimentos (Fig. R.3) [57]. También para este caso se puede estudiar el papel de los efectos estocásticos mediante la simulación de la ecuación de Langevin obteniendo de nuevo una buen acuerdo con los resultados experimentales.

Encontrar un potencial compatible con la información experimental disponible, no solo permite una comprensión de los mecanismos básicos del funcionamiento del motor sino que también permite formular predicciones de la gestión energética del motor. Esta información, normalmente no es accesible experimentalmente. No obstante, el marco teórico desarrollado permite calcular todas las energía de entrada y salida del motor y por lo tanto calcular potencias y eficiencias. El resultado más relevante de este análisis es la diferencia entre el modelo

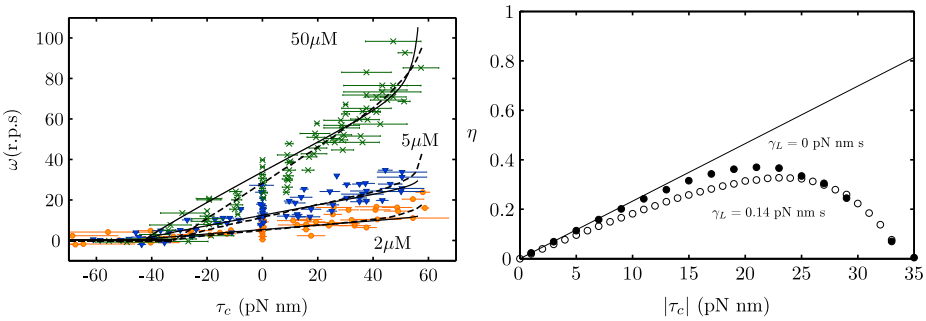

Figura R.3: Funcionamiento del F_1 bajo una torque conservativo. Izquierda: velocidad angular media del motor. Los resultados experimentales (*símbolos*) conmparan bien con los resultados analíticos deterministas (R.3) (*linea continua*) y con las simulaciones estocástica (*línea discontinua*). Derecha: Eficiencia del motor determinista (*linea*) comparada con los resultados estocásticos (*símbolos*) para dos casos diferentes de la fricción de la carga.

determinista y las simulaciones estocásticas. En el análisis determinista de un motor, el máximo de eficiencia se encuentra cerca de la fuerza de calado del motor para la cual el motor se para. Esto deja de ser cierto cuando las fluctuaciones se tienen en cuenta. Cerca de la fuerza de calado, la dinámica del motor viene regida por las fluctuaciones térmicas que borran el avance del motor y por lo tanto el trabajo que realiza éste [70]. De esta forma, la fluctuaciones térmicas reducen a cero la eficiencia cerca de la fuerza de calado y un nuevo valor óptimo de la eficiencia aparece para valores intermedios del torque externo (Fig. R.3). Este resultado es de especial relevancia para motores moleculares biológicos ya que se espera que hayan evolucionado para funcionar en un régimen de trabajo óptimo. En este caso, el régimen óptimo no se puede predecir por un análisis puramente determinista siendo necesario el análisis estocástico del sistema. Por lo tanto, este resultado no sólo introduce un predicción para la eficiencia sino que pone en evidencia que las fluctuaciones térmicas no pueden ser despreciadas

cuando se quiere estudiar las transformación energética en motores moleculares.

Aproximación de Fokker–Planck para el estudio de motores moleculares

Debido a la no linearidad del mecanismo de potenciales intermitentes, la solución de la ecuación de Langevin no se puede resolver analíticamente. Por lo tanto, el análisis de las fluctuaciones térmicas se tiene que hacer mediante simulaciones o resolviendo la ecuación de Fokker–Planck para el potencial estático en uno de sus múltiples estados. Esto inspiró el desarrollo de un procedimiento analítico para analizar este tipo de sistemas aproximando la ecuación de Langevin por una ecuación de Fokker–Planck que contenga la dinámica del potencial [54]. Esta aproximación considera la intermitencia del potencial con un ruido dicotómico que se puede aproximar a su vez como un ruido blanco. La ecuación resultante es una ecuación de F–P con un coeficiente de difusión dependiente de la posición. Esta ecuación se puede resolver analíticamente obteniendo predicciones para la velocidad del motor.

Los resultados del esta aproximación se han comparado exitosamente con los resultado experimentales del motor F_1 [54]. El acuerdo entre la teoría y el modelo es bueno para regímenes de alta concentración de ATP o cargas grandes. Para evaluar la validez de la aproximación, se puede obtener una expresión analítica de un predictor. Este predictor ofrece un valor umbral a partir del cual la aproximación funciona.

El estudio de este problema también reveló que los algoritmos tradicionales

de integración de ecuaciones de Langevin en la interpretación de Stratonovich fallaban en converger a la solución correcta cuando el coeficiente de difusión no es continuo en el espacio. Este problema se puede resolver mediante el uso de un nuevo algoritmo basado en el significado de la interpretación de Stratonovich [55].

Motores que trabajan con un flujo de iones

Finalmente, el marco teórico desarrollado se puede aplicar al estudio de motores moleculares que trabajan con un flujo de iones. Estos motores presentan nuevas cuestiones que se originan en el cambio de mecanismo de transducción. Ahora un flujo de iones se acopla con el movimiento de un rotor transmembranal. Con el objetivo de entender los características básicas de este acoplamiento, se ha estudiado un modelo sencillo. Este modelo consiste en un pistón móvil que separa dos gases de partículas que interaccionan con el pistón. El pistón tiene condiciones de contorno periódicas en sus fronteras simulando el comportamiento de una turbina. Así la diferencia de presiones a ambos lados del pistón se traduce en un movimiento direccional del pistón (Fig. R.4) [58]. Para estudiar la transducción energética de esta turbina molecular se aplica una fuerza externa en el pistón. Esta fuerza puede tener sentido contrario al movimiento espontáneo de la turbina extrayendo trabajo mecánico de ella. Adicionalmente, para una fuerza externa suficientemente grande, la velocidad de la turbina y el flujo de iones se puede revertir. En este régimen la turbina funciona como una bomba en la que la fuerza externa se usa para incrementar la energía de membrana. El análisis del funcionamiento de la turbina, incluyendo las fluctuaciones térmicas correspondientes, revela que el flujo de partículas a través del motor y la velocidad de éste no son proporcionales (Fig. R.4). De hecho, la fuerza necesaria para invertir la velocidad del motor es diferente a la fuerza necesaria para invertir el flujo del mo-

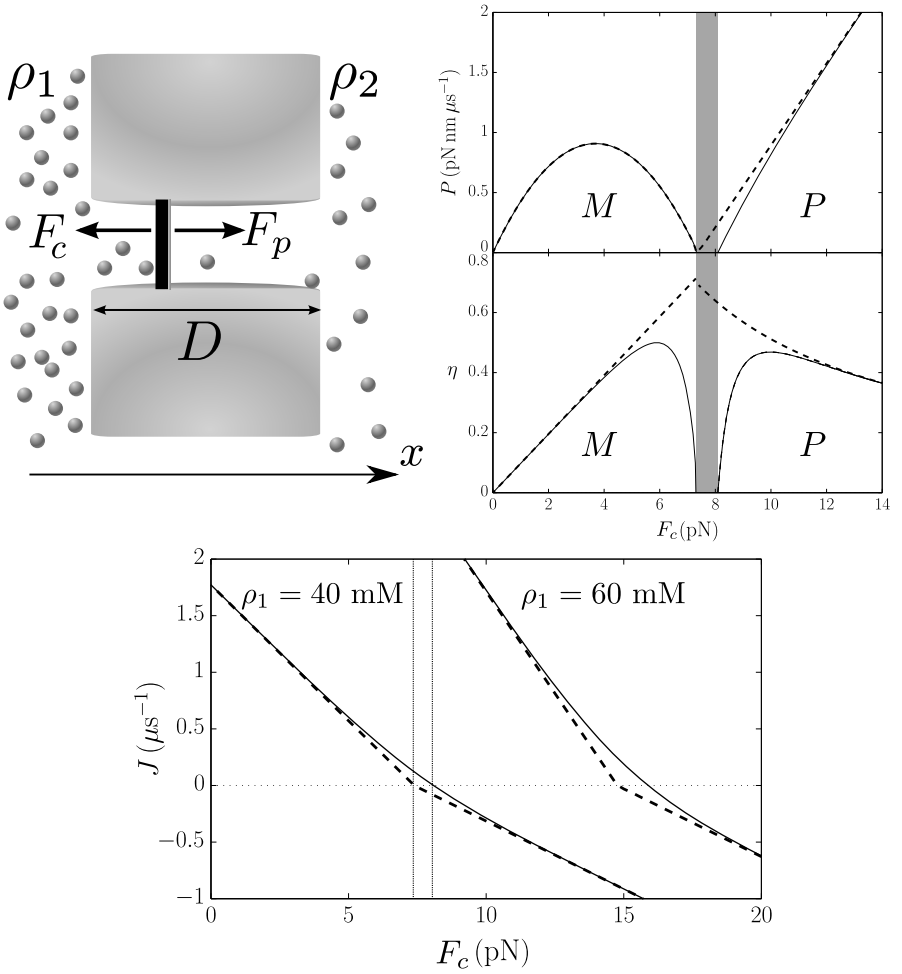

Figura R.4: Arriba izquierda: Esquema de la turbina de un pistón. Arriba derecha: Potencia y eficiencia de la turbina con respecto a la fuerza externa, comparando los resultados deterministas sin ruido térmico (*línea discontinua*) con los estocásticos (*línea continua*). Se muestran los tres regímenes: motor (M), bomba (P) y zona de pérdidas (*sombreado gris*). Abajo: Dependencia del flujo de partículas de la turbina con la fuerza externa para el caso determinista (*línea discontinua*) y para el caso estocástico (*linea continua*) para diferentes valores de la densidad de partículas ρ_1.

tor. Esto crea un régimen de pérdidas para valores intermedios de la fuerza para el cual el motor retrocede en el mismo sentido que la fuerza externa, impidiendo la extracción de trabajo mecánico, sin llegar a invertir el flujo de partículas, perdiendo energía de membrana continuamente. La zona de pérdidas se debe a efectos térmicos, debido a que fluctuaciones simétricas en el pistón dan lugar a un traspaso de iones asimétrico a través de la turbina. Para este modelo se puede también estudiar su gestión energética obteniendo un desacuerdo completo entre el caso determinista (sin ruido térmico) y el estocástico (con ruido térmico) cerca de la zona de pérdidas (Fig. R.4). El modelo determinista no es capaz de predecir la zona de pérdidas del modelo estocástico para el cual la eficiencia cae a cero cerca de la fuerza de calado del motor. La situación es similar a la obtenida para la eficiencia del motor F_1. Cerca de la fuerza de calado las fluctuaciones lideran la dinámica del motor impidiendo la transducción energética. En el caso de la turbina, este fenómeno da lugar a dos nuevos máximos de eficiencia para valores intermedios de la fuerza tanto en el régimen de bomba como en el régimen de turbina (Fig. R.4) [58]. Siguiendo los mismos argumentos que en el caso del motor F_1, la relevancia de este decaimiento debido a fluctuaciones térmicas es alta ya que implica que no se pueden obviar las fluctuaciones térmicas en el estudio de las máquinas moleculares.

El modelo ideal presentado con la turbina de un pistón carece de una descripción rigurosa de la difusión de las partículas. Por lo tanto, un segundo modelo ha sido propuesto conteniendo múltiples álabes equidistantes dentro de la turbina. Este segundo modelo presenta relaciones similares a las de la turbina formada por un solo pistón. La velocidad y el flujo siguen teniendo valores diferentes de inversión dando lugar a la zona de pérdidas. En este caso más realista la zona de pérdidas es incluso más grande que la descrita en el caso anterior y resulta también en un valor más pequeño de la eficiencia. Por lo tanto la introducción de

elementos más realistas en la turbina no elimina los efectos de las fluctuaciones térmicas sino que los incrementan.

Para acabar, este escenario fue analizado numéricamente para comprobar que las suposiciones tomadas en el diseño del modelo eran válidas en la escala biológica. Estas simulaciones no sólo corroboran las predicciones analíticas sino que también se convierten en una buena herramienta para analizar un escenario biológico más realista en el cual otras interacciones, como pueden ser el voltaje de la membrana o la interacción entre partículas se pueden considerar.

Todos los resultados que se exponen en este resumen están explícitamente documentados a lo largo de la tesis y en las publicaciones que se citan en el resumen. Asimismo, las referencias de estas publicaciones, que han dado lugar a esta tesis, están también recogidas de forma separada en la sección "Publications of this thesis".

Bibliography

[1] Abrahams J.P., Leslie A.G., Lutter R., & Walker J.E. Structure at 2.8 Å resolution of F1-ATPase from bovine heart mitochondria. *Nature*, **370**(6491):621 (1994).

[2] Akola J. & Jones R.O. ATP Hydrolysis in Water - A Density Functional Study. *The Journal of Physical Chemistry B*, **107**(42):11774 (2003).

[3] Alberts B. The cell as a collection overview of protein machines: Preparing the next generation of molecular biologists. *Cell*, **92**:291 (1998).

[4] Alberts B. *Molecular Biology of the Cell*. Molecular Biology of the Cell. Taylor & Francis Group (2008). ISBN 9780815341055.

[5] Antes I., Chandler D., Wang H., & Oster G. The unbinding of ATP from F1-ATPase. *Biophysical Journal*, **85**(2):695 (2003).

[6] Bai F., Lo C.J., Berry R.M., & Xing J. Model Studies of the Dynamics of Bacterial Flagellar Motors. *Biophysical Journal*, **96**(8):3154 (2009).

[7] Baker M.A.B. & Berry R.M. An introduction to the physics of the bacterial flagellar motor: a nanoscale rotary electric motor. *Contemporary Physics*, **50**(6):617 (2009).

[8] Buono M. & Kolkhorst F. Estimating ATP resynthesis during a marathon run: a method to introduce metabolism. *Advances in Physiology Education*, **25**:142 (2001).

[9] Campàs O., Leduc C., Bassereau P., Casademunt J., Joanny J.F., & Prost J. Coordination of Kinesin Motors Pulling on Fluid Membranes. *Biophysical Journal*, **94**(12):5009 (2008).

[10] Chen L., Nakamura M., Schindler T.D., Parker D., & Bryant Z. Engineering controllable bidirectional molecular motors based on myosin. *Nature nanotechnology*, **7**(4):252 (2012).

[11] Chowdhury D. Machines of life: catalogue, stochastic process modeling, probabilistic reverse engineering and the PIs- from Aristotle to Alberts. *arXiv.org*, **physics.bio-ph** (2012).

[12] Chowdhury D. Stochastic mechano-chemical kinetics of molecular motors: a multidisciplinary enterprise from a physicist's perspective. *arXiv.org*, **physics.bio-ph** (2012).

[13] Ciudad A. & Sancho J.M. External mechanical force as an inhibition process in kinesin's motion. *The Biochemical journal*, **390**(1):345 (2005).

[14] Ciudad A. & Sancho J.M. A unified phenomenological analysis of the experimental velocity curves in molecular motors. *Journal of Chemical Physics*, **128**(2):5107 (2008).

[15] Ciudad A. & Sancho J.M. Analysis of the nucleotide-dependent conformations of kinesin-1 in the hydrolysis cycle. *The Journal of Chemical Physics*, **131**(1):015104 (2009).

[16] Ciudad A., Sancho J.M., & Lacasta A.M. Dynamics of an inchworm nano-walker. *Physica A: Statistical Mechanics and its Applications*, **371**(1):25 (2006).

[17] Conn H. *The story of life's mechanism: a review of the conclusions of modern biology in regard to the mechanism which controls the phenomena of living activity.* Library of useful stories. G. Newnes (1899).

[18] Csete M. & Doyle J. Reverse engineering of biological complexity. *Science Signalling*, **295**(5560):1664 (2002).

[19] Czub J. & Grubmüller H. Torsional elasticity and energetics of F1-ATPase. *Proceedings of the National Academy of Sciences of the United States of America*, **108**(18):7408 (2011).

[20] Fox R., Gatland I., Roy R., & Vemuri G. Fast, accurate algorithm for numerical simulation of exponentially correlated colored noise. *Physical Review A*, **38**(11):5938 (1988).

[21] García-Ojalvo J. & Sancho J. *Noise in Spatially Extended Systems.* Institute for Nonlinear Science. Springer (1999). ISBN 9780387988559.

[22] Gardiner C. *Handbook of stochastic methods for physics, chemistry, and the natural sciences.* Springer series in synergetics. Springer (1985). ISBN 9783540156079.

[23] Geeves M. & Holmes K. Structural mechanism of muscle contraction. *Annual review of biochemistry*, **68**(1):687 (1999).

[24] Germano G., Politi M., Scalas E., & Schilling R. Stochastic calculus for uncoupled continuous-time random walks. *Physical Review E*, **79**(6) (2009).

[25] Gibbons C., Montgomery M.G., Leslie A.G., & Walker J.E. The structure of the central stalk in bovine F1-ATPase at 2.4 Å resolution. *Nature structural biology*, **7**(11):1055 (2000).

[26] Hirono-Hara Y., Ishizuka K., Kinosita K.J., Yoshida M., & Noji H. Activation of pausing F1 motor by external force. In *Proceedings of the National Academy of Science*, pages 4288–4293 (2005).

[27] Horsthemke W. & Lefever R. *Noise-Induced Transitions: Theory and Applications in Physics, Chemistry, and Biology.* Springer Series in Synergetics. Springer (2007). ISBN 9783540113591.

[28] Inoue Y., Lo C.J., Fukuoka H., Takahashi H., Sowa Y., Pilizota T., Wadhams G.H., Homma M., Berry R.M., & Ishijima A. Torque–Speed Relationships of Na+-driven Chimeric Flagellar Motors in Escherichia coli. *Journal of Molecular Biology*, **376**(5):1251 (2008).

[29] Itoh H., Takahashi A., Adachi K., Noji H., Yasuda R., Yoshida M., & Kinosita K. Mechanically driven ATP synthesis by F1-ATPase. *Nature*, **427**(6973):465 (2004).

[30] Kay E.R., Leigh D.A., & Zerbetto F. Synthetic Molecular Motors and Mechanical Machines. *Angewandte Chemie International Edition*, **46**(1-2):72 (2007).

[31] Kim C., Lee E., & Talkner P. Numerical method for solving stochastic differential equations with dichotomous noise. *Physical Review E*, **73**(2) (2006).

[32] Kloeden P. & Platen E. *Numerical Solution of Stochastic Differential Equations*. Applications of Mathematics Series. Springer (2011). ISBN 9783540540625.

[33] Kudernac T., Ruangsupapichat N., Parschau M., Maciá B., Katsonis N., Harutyunyan S.R., Ernst K.H., & Feringa B.L. Electrically driven directional motion of a four-wheeled molecule on a metal surface. *Nature*, **479**(7372):208 (2011).

[34] Kupferman R., Pavliotis G., & Stuart A. Itô versus Stratonovich white-noise limits for systems with inertia and colored multiplicative noise. *Physical Review E*, **70**(3) (2004).

[35] Leduc C., Campàs O., Zeldovich K., Roux A., Jolimaitre P., Bourel-Bonnet L., Goud B., Joanny J., Bassereau P., & Prost J. Cooperative extraction of membrane nanotubes by molecular motors. *Proceedings of the National Academy of Sciences*, **101**(49):17096 (2004).

[36] Lo C.J., Leake M.C., Pilizota T., & Berry R.M. Nonequivalence of Membrane Voltage and Ion-Gradient as Driving Forces for the Bacterial Flagellar Motor at Low Load. *Biophysical Journal*, **93**(1):294 (2007).

[37] Mannella R. & Palleschi V. Fast and precise algorithm for computer simulation of stochastic differential equations. *Physical Review A*, **40**(6):3381 (1989).

[38] Milstein G. *Numerical Integration of Stochastic Differential Equations*. Mathematics and Its Applications. Springer (1994). ISBN 9780792332138.

[39] Moffitt J.R., Chemla Y.R., Aathavan K., Grimes S., Jardine P.J., Anderson D.L., & Bustamante C. Intersubunit coordination in a homomeric ring ATPase. *Nature*, **457**(7228):446 (2009).

[40] Moffitt J.R., Chemla Y.R., & Bustamante C. Mechanistic constraints from the substrate concentration dependence of enzymatic fluctuations. *Proceedings of the National Academy of Sciences of the United States of America*, **107**(36):15739 (2010).

[41] Moffitt J.R., Chemla Y.R., & Bustamante C. Methods in statistical kinetics. *Methods in enzymology*, **475**:221 (2010).

[42] Mora T., Yu H., Sowa Y., & Wingreen N.S. Steps in the Bacterial Flagellar Motor. *PLoS Computational Biology*, **5**(10):e1000540 (2009).

[43] Morin J.F., Shirai Y., & Tour J.M. En Route to a Motorized Nanocar. *Organic Letters*, **8**(8):1713 (2006).

[44] Muneyuki E., Watanabe-Nakayama T., Suzuki T., Yoshida M., Nishizaka T., & Noji H. Single Molecule Energetics of F1-ATPase Motor. *Biophysical Journal*, **92**(5):1806 (2007).

[45] Murphy G.E., Leadbetter J.R., & Jensen G.J. In situ structure of the complete Treponema primitia flagellar motor. *Nature*, **442**(7106):1062 (2006).

[46] Naber N., Minehardt T.J., Rice S., Chen X., Grammer J., Matuska M., Vale R.D., Kollman P.A., Car R., Yount R.G., Cooke R., & Pate E. Closing of the nucleotide pocket of kinesin-family motors upon binding to microtubules. *Science*, **300**(5620):798 (2003).

[47] Noji H., Yasuda R., Yoshida M., & Kinosita K. Direct observation of the rotation of F1-ATPase. *Nature*, **386**(6):299 (1997).

[48] O'Kelly C., Farmer M., & Nerad T. Ultrastructure of Trimastix pyriformis (Klebs) Bernard et al.: Similarities of Trimastix Species with Retortamonad and Jakobid Flagellates. *Protist*, **150**(2):149 (1999).

[49] Oster G. & Wang H. Why is the mechanical efficiency of F(1)-ATPase so high? *Journal of bioenergetics and biomembranes*, **32**(5):459 (2000).

[50] Palanisami A. & Okamoto T. Torque-Induced Slip of the Rotary Motor F1-ATPase. *Nano Letters*, **10**(10):4146 (2010).

[51] Pänke O., Cherepanov D., Gumbiowski K., Engelbrecht S., & Junge W. Viscoelastic dynamics of actin filaments coupled to rotary F-ATPase: angular torque profile of the enzyme. *Biophysical Journal*, **81**(3):1220 (2001).

[52] Parrondo J.M.R. & de Cisneros B.J. Energetics of Brownian motors: a review. *Applied Physics A: Materials Science & Processing*, **75**(2):179 (2002).

[53] Perez-Carrasco R., Fiasconaro A., Falo F., & Sancho J.M. Modelling the mechano,Äìchemistry of the DNA translocation motor (Preprint).

[54] Perez-Carrasco R. & Sancho J.M. Fokker-Planck approach to molecular motors. *Europhysics Letters*, **91**(6):60001 (2010).

[55] Perez-Carrasco R. & Sancho J.M. Stochastic algorithms for discontinuous multiplicative white noise. *Physical Review E*, **81**(3):32104 (2010).

[56] Perez-Carrasco R. & Sancho J.M. Theoretical analysis of the F(1)-ATPase experimental data. *Biophysical Journal*, **98**(11):2591 (2010).

[57] Perez-Carrasco R. & Sancho J.M. Molecular motors in conservative and dissipative regimes. *Physical Review E*, **84**(4):041915 (2011).

[58] Perez-Carrasco R. & Sancho J.M. Physics of molecular machines operated by a particle flux. *Europhysics Letters*, **100**:40001 (2012).

[59] Peter C. & Hummer G. Ion Transport through Membrane-Spanning Nanopores Studied by Molecular Dynamics Simulations and Continuum Electrostatics Calculations. *Biophysical Journal*, **89**(4):2222 (2005).

[60] Pogoryelov D., Klyszejko A.L., Krasnoselska G.O., Heller E.M., Leone V., Langer J.D., Vonck J., Muller D.J., Faraldo-Gómez J.D., & Meier T. Engineering rotor ring stoichiometries in the ATP synthase. *Proceedings of the National Academy of Sciences of the United States of America*, **109**(25):E1599 (2012).

[61] Purcell E. Life at low Reynolds number. *Am. J. Phys*, **45**(1):3 (1977).

[62] Rao F. & Spichty M. Thermodynamics and kinetics of large-time-step molecular dynamics. *Journal of Computational Chemistry*, **33**(5):475 (2011).

[63] Reid S., Leake M., Chandler J., Lo C., Armitage J., & Berry R. The maximum number of torque-generating units in the flagellar motor of Escherichia coli is at least 11. *Proceedings of the National Academy of Sciences*, **103**(21):8066 (2006).

[64] Reimann P. Brownian motors: noisy transport far from equilibrium. *Physics Reports*, **361**(2):57 (2002).

[65] Rickgauer J.P., Fuller D.N., Grimes S., Jardine P.J., Anderson D.L., & Smith D.E. Portal Motor Velocity and Internal Force Resisting Viral DNA Packaging in Bacteriophage 29. *Biophysical Journal*, **94**(1):159 (2008).

[66] Riedel Kruse I.H., Hilfinger A., Howard J., & Jülicher F. How molecular motors shape the flagellar beat. *HFSP Journal*, **1**(3):192 (2007).

[67] Risken H. *The Fokker-Planck Equation: Methods of Solution and Applications*. Springer Series in Synergetics. Springer (1996). ISBN 9783540615309.

[68] Sagawa T. & Ueda M. Generalized Jarzynski Equality under Nonequilibrium Feedback Control. *Physical Review Letters*, **104**(9) (2010).

[69] Sagués F., Sancho J., & Garcia-Ojalvo J. Spatiotemporal order out of noise. *Reviews of Modern Physics*, **79**(3):829 (2007).

[70] Sancho J.M. & Perez-Carrasco R. Power and Efficiency of F1-ATPase Molecular Motor. *Fluctuation and Noise Letters*, **11**(01):1240003 (2012).

[71] Sancho J.M., San Miguel M., Katz S., & Gunton J. Analytical and numerical studies of multiplicative noise. *Physical Review A*, **26**(3):1589 (1982).

[72] Schliwa M. *Molecular Motors*. Wiley (2006). ISBN 9783527605651.

[73] Schüler D. & Frankel R. Bacterial magnetosomes: microbiology, biomineralization and biotechnological applications. *Applied microbiology and biotechnology*, **52**(4):464 (1999).

[74] Sekimoto K. Kinetic Characterization of Heat Bath and the Energetics of Thermal Ratchet Models. *Journal of the Physical Society of Japan*, **66**(5):1234 (1997).

[75] Shimabukuro K., Yasuda R., Muneyuki E., Hara K.Y., Kinosita K., & Yoshida M. Catalysis and rotation of F1 motor: cleavage of ATP at the catalytic site occurs in 1 ms before 40 degree substep rotation. *Proceedings of the National Academy of Sciences of the United States of America*, **100**(25):14731 (2003).

[76] Sielaff H., Rennekamp H., Wächter A., Xie H., Hilbers F., Feldbauer K., Dunn S.D., Engelbrecht S., & Junge W. Domain compliance and elastic power transmission in rotary F(O)F(1)-ATPase. *Proceed-*

ings of the National Academy of Sciences of the United States of America, **105**(46):17760 (2008).

[77] Silflow C.D. & Lefebvre P.A. Assembly and Motility of Eukaryotic Cilia and Flagella. Lessons from Chlamydomonas reinhardtii. *PLANT PHYSIOLOGY*, **127**(4):1500 (2001).

[78] Small J., Stradal T., Vignal E., & Rottner K. The lamellipodium: where motility begins. *Trends in Cell Biology*, **12**(3):112 (2002).

[79] Sowa Y. & Berry R.M. Bacterial flagellar motor. *Quarterly reviews of biophysics*, **41**(2):103 (2008).

[80] Sowa Y., Hotta H., Homma M., & Ishijima A. Torque–speed Relationship of the Na+-driven Flagellar Motor of Vibrio alginolyticus. *Journal of Molecular Biology*, **327**(5):1043 (2003).

[81] Spetzler D., York J., Daniel D., Fromme R., Lowry D., & Frasch W. Microsecond time scale rotation measurements of single F1-ATPase molecules. *Biochemistry*, **45**(10):3117 (2006).

[82] Stratonovich R. *Topics in the Theory of Random Noise: Peaks of random functions and the effect of noise on relays, nonlinear self-excited oscillations in the presence of noise*. Mathematics and Its Applications Series. CRC PressINC (1967). ISBN 9780677007908.

[83] Stryer L. *Biochemistry 4 Ed.* Freeman (1995). ISBN 9780716720096.

[84] Tieleman D. & Berendsen H. A molecular dynamics study of the pores formed by Escherichia coli OmpF porin in a fully hydrated palmitoyloleoylphosphatidylcholine bilayer. *Biophysical Journal*, **74**(6):2786 (1998).

[85] Toyabe S., Sagawa T., Ueda M., Muneyuki E., & Sano M. Experimental demonstration of information-to-energy conversion and validation of the generalized Jarzynski equality. *Nature Physics*, **6**(12):988 (2010).

[86] Vale R. The molecular motor toolbox for intracellular transport. *Cell*, **112**(4):467 (2003).

[87] Visscher K., Schnitzer M.J., & Block S.M. Single kinesin molecules studied with a molecular force clamp. *Nature*, **400**(6740):184 (1999).

[88] Wang H. Several Issues in Modeling Molecular Motors. *Journal of Computational and Theoretical Nanoscience*, **5**(12):2311 (2008).

[89] Wang H. & Oster G. The Stokes efficiency for molecular motors and its applications. *EPL (Europhysics Letters)*, **57**(1):134 (2002).

[90] Watanabe-Nakayama T., Toyabe S., Kudo S., Sugiyama S., Yoshida M., & Muneyuki E. Effect of external torque on the ATP-driven rotation of F1-ATPase. *Biochemical and Biophysical Research Communications*, **366**(4):951 (2008).

[91] Wiedenmann A., Dimroth P., & von Ballmoos C. Deltapsi and DeltapH are equivalent driving forces for proton transport through isolated F0 complexes of ATP synthases. *Biochimica et biophysica acta*, **1777**(10):1301 (2008).

[92] Wiedenmann A., Dimroth P., & von Ballmoos C. Functional asymmetry of the F(0) motor in bacterial ATP synthases. *Molecular microbiology*, **72**(2):479 (2009).

[93] Wong E. & Zakai M. On the convergence of ordinary integrals to stochastic integrals. *The Annals of Mathematical Statistics*, pages 1560–1564 (1965).

[94] Yasuda R., Noji H., Kinosita K., & Yoshida M. F1-ATPase is a highly efficient molecular motor that rotates with discrete 120 degree steps. *Cell*, **93**(7):1117 (1998).

[95] Yasuda R., Noji H., Yoshida M., Kinosita K., & Itoh H. Resolution of distinct rotational substeps by submillisecond kinetic analysis of F1-ATPase. *Nature*, **410**(6831):898 (2001).

[96] Yoshida M., Muneyuki E., & Hisabori T. ATP synthase–a marvellous rotary engine of the cell. *Nature reviews. Molecular cell biology*, **2**(9):669 (2001).

Symbol Glossary

A	Piston Area
cr, cr^0, cr^*	Coupling ratio
d	Intervane distance
D	Membrane/Turbine width
F	Force
$\overline{F}$	Net average force
$F^M_{\text{stall}}, F^P_{\text{stall}}$	Stall forces for motor and pump regimes
E_i, E_1, E_2	Energy supplied in different substeps
g	Noise intensity component
k	Reaction rate
k_{ATP}	ATP caption rate
k_0	ATP dwell time rate component dependent of [ATP]
k_0^0, k_0^1	Components of the linear relation $k_0(\tau_c)$
$k_B T$	Thermal energy
J	Probability flux. Particle flux
N	Number of particles
P	Probability distribution

P_i, P_E, P_R	Probability distribution corresponding to a certain potential
$P_{\rightarrow}, P_{\leftarrow}$	Probablity of finishing a cycle in a particular direction
$P_{\text{in}}, P_{\text{out}}$	Input power, output power
P_M, P_P	Power of motor, Power of pump
Q	Heat
t	Time variable
t_i	Duration of a subprocess
$t_{\text{chem}}, t_{\text{mech}}$	Duration of chemical and mechanical processes
t_s	Catalytic dwell duration
t_0	Catalytic time
t_E, t_R	Duration of a certain potential state
t_γ	Inertial time
(t_i, t_f)	Initial and final times of a process
$\mathcal{T}$	Average duration of a motor cycle
$\mathcal{T}_v$	Stoke's average duration of a motor cycle
v	Linear velocity
V	Motor Potential. Electrostatic component of the membrane potential
V_i, V_E, V_R	Static potentials components of the potential V
V_0, V_1	Motor potential heights
V_0	Volume of particles translocated per step
W	Mechanical work
$W_{\Delta t}$	Wiener increment
x, X	Spatial linear coordinate
z	Motor potential state function
α	Substep fraction
α_M	Optimum value for the substep fraction
β	Intervane fraction of available volume

γ	Friction coefficient
γ_0	Internal friction coefficient of a motor
γ_L	Friction coefficient of the cargo
γ_{eff}	Effective friction of the motor including external drag
$\delta\theta$	Thermal variaton of the substep length
ΔG	Useful chemical free energy related to an external entity
ΔG_{ATP}	Useful hydrolysis energy of ATP
Δg	Single particle free energy
ε	Dimensionless parameter controlling motor potential height
ϵ	Predictor parameter for the goodness of the White Noise Limit
η	Motor potential state function. Efficiency
$\bar{\eta}$	Average value of the dichotomous noise
η_L	Stoke's efficiency
θ	Angular/Spatial coordinate
θ_0	Step length of a motor cycle
$\theta_i, \theta_1, \theta_2$	Substep length
κ	Load-Shaft Stiffness
λ	Linear density of particles
ξ	Thermal force
ξ_{OU}	Ornstein–Uhlenbeck process
ρ, ρ_1, ρ_2	Particle density
σ_W	Noise intensity
τ	Torque
$\tau_{\text{in}}, \tau_i, \tau_1\tau_2$	Motive torque
τ_{c}	Conservative torque
τ_{ex}	External torque
φ	Angular coordinate of the load

ϕ	Membrane potential
χ	White noise
ω	Average angular velocity
ω_E, ω_R	Jump rates of a dichotomous noise

Publications of this thesis

- Perez–Carrasco R., & Sancho J.M. Fokker-Planck approach to molecular motors. *Europhysics Letters*, **91**(6):60001 (2010).
- Perez–Carrasco R., & Sancho J.M. Theoretical analysis of the F1–ATPase experimental data. *Biophysical Journal*, **98**(11):2591 (2010).
- Perez–Carrasco R., & Sancho J.M. Stochastic algorithms for discontinuous multiplicative white noise. *Physical Review E*, **81**(3):32104 (2010).
- Perez–Carrasco R., & Sancho J.M. Molecular motors in conservative and dissipative regimes. *Physical Review E*, **84**(4):041915 (2011).
- Sancho J.M., & Perez-Carrasco R. Power and Efficiency of F1-ATPase Molecular Motor. *Fluctuation and Noise Letters*, **11**(01):1240003 (2012).
- Perez–Carrasco R., & Sancho J.M. Physics of molecular machines operated by a particle flux. *Europhysics Letters*, **100**:40001 (2012).
- Perez–Carrasco R., Fiasconaro A, Falo F., & Sancho J.M. Modelling the mechano–chemistry of the ϕ29 DNA translocation motor (Preprint).